

**THE DESIGN, SYNTHESIS, AND OPTIMIZATION OF  
NANOMATERIALS FABRICATED IN SUPERCRITICAL  
CARBON DIOXIDE**

A Thesis  
Presented to  
The Academic Faculty

by

Michael John Casciato

In Partial Fulfillment  
of the Requirements for the Degree  
Doctor of Philosophy in the  
School of Chemical & Biomolecular Engineering

Georgia Institute of Technology  
August 2013

Copyright © 2013 by Michael John Casciato

# THE DESIGN, SYNTHESIS, AND OPTIMIZATION OF NANOMATERIALS FABRICATED IN SUPERCRITICAL CARBON DIOXIDE

Approved by:

Professor Martha A. Grover, Advisor  
School of Chemical & Biomolecular  
Engineering  
*Georgia Institute of Technology*

Professor Dennis W. Hess, co-Advisor  
School of Chemical & Biomolecular  
Engineering  
*Georgia Institute of Technology*

Professor Charles A. Eckert  
School of Chemical & Biomolecular  
Engineering  
*Georgia Institute of Technology*

Professor Michael A. Filler  
School of Chemical & Biomolecular  
Engineering  
*Georgia Institute of Technology*

Professor J.C. Lu  
H. Milton Stewart School of Industrial  
& Systems Engineering  
*Georgia Institute of Technology*

Date Approved: 4 June 2013

*Never give in. Never give in. Never, never, never, never — in  
nothing, great or small, large or petty — never give in, except to  
convictions of honor and good sense. Never yield to force; never yield  
to the apparently overwhelming might of the enemy.*

Sir Winston Churchill

Speech to the Harrow School

October 29, 1941

*The dedication of this thesis is split seven ways:*

*...to mom, for her love...*

*...to John & Dominick, for their brotherhood...*

*...to Gram & Pop, for their support...*

*...to Dr. Grover & Dr. Hess, for their mentorship...*

*...to the Crew, for their friendship...*

*...to Jose, Loice, and Lina, for their camaraderie...*

*...and to everyone who has stuck with me while working on this thesis*

*until the*

*very*

*end.*

## ACKNOWLEDGEMENTS

I would like to acknowledge my mom, Bonnie, and my brothers, Dominick and John, for their love and support not only during graduate school but throughout my whole life.

I give my sincerest thanks to my excellent advisors, Professor Martha A. Grover and Professor Dennis W. Hess. Their mentorship, guidance, and kindness were invaluable in succeeding in this chapter of my life.

I also thank the members of my dissertation committee, Professor Charles A. Eckert, Professor Michael A. Filler, and Professor J.C. Lu, for their advice and suggestions as I worked to develop and complete my thesis studies.

I am grateful to my funding sources: the National Science Foundation Graduate Research Fellowship Program; the National Science Foundation Division of Chemical, Bioengineering, Environmental, and Transport (CBET) Grant # 0933430; the Georgia Institute of Technology President's Fellowship; and the Goizueta Foundation Fellowship.

I am thoroughly grateful to Galit Levitin, whose friendship and mentorship were incredibly helpful to me throughout my studies at Georgia Tech.

I thank Professor Christopher W. Jones for his mentorship during my teaching practicum, which I thoroughly enjoyed.

I also thank Professor Damon Williams, who has been an exceptional role model and friend at Georgia Tech, in CETL, and beyond.

I thank the many group members I have enjoyed becoming friends with over the years in both the Grover and Hess groups (in no particular order): Lester Li, Sonam

Sherpa, Tae-Seop Choi, Andres Hernandez-Moreno, Dan Griffin, Christine He, Ming-Chien Hsieh, Zhenguan Tang, Xun Tang, Huayu Li, Sheng-Sheng Yu, Michelle Kuykendal, Jonathan Rawlston, Justin Vastola, Aparna Boddapati, Sungil Kim, Ashish Pande, Fangyu Wu, and Balamurali Balu. I thank my many friends at Georgia Tech, but in particular I thank Jose, Loice, and Lina for their kindness and support.

I thank and acknowledge the help and assistance of the wonderful staff at the Institute for Electronics and Nanotechnology (IEN), in particular Gary Spinner, Michael Ross, Charlie Suh, Eric Woods, and Todd Walters. I also acknowledge the assistance of my undergraduate mentees: Fuad Gaya, Jen Kim, and Andrew Wong.

I thank Shannon Capps and Krystle Chavez, who were incredibly kind in helping me transition into the ChBE program and Atlanta.

Last, I thank the following teachers and mentors from elementary, middle, high school, and college who nurtured my passion for learning and scholarship: Mrs. Gretchen Fletcher, Mrs. Gretchen Steinberg, Dr. Silvia Lanza, Dr. Jeremy Rowan, Mr. Scott Orcutt, Fr. Charles Newburn, and Dr. Angel Kaifer.

# TABLE OF CONTENTS

<b>ACKNOWLEDGEMENTS</b> . . . . .	<b>v</b>
<b>LIST OF TABLES</b> . . . . .	<b>xii</b>
<b>LIST OF FIGURES</b> . . . . .	<b>xiv</b>
<b>SUMMARY</b> . . . . .	<b>xix</b>
<b>I INTRODUCTION</b> . . . . .	<b>1</b>
1.1 Nanotechnology Background . . . . .	1
1.1.1 Brief history of nanotechnology and its applications . . . . .	1
1.1.2 Techniques for fabricating nanostructures . . . . .	3
1.1.3 Supercritical carbon dioxide for nanostructure synthesis . . . . .	5
1.2 Background on experimental design . . . . .	8
1.2.1 Brief history of experimental design . . . . .	8
1.2.2 Applications of experimental design in nanotechnology research . . . . .	11
1.3 Challenges in the synthesis and optimization of nanomaterials in sc-CO <sub>2</sub> . . . . .	13
1.4 Summary of thesis objectives and contributions . . . . .	14
<b>II SYNTHESIS OF Cu<sub>2</sub>ZnSnS<sub>4</sub> PARTICLES IN SUPERCRITICAL CARBON DIOXIDE</b> . . . . .	<b>19</b>
2.1 Introduction . . . . .	19
2.2 Experimental Methods . . . . .	20
2.2.1 Materials . . . . .	20
2.2.2 Reactor Design . . . . .	21
2.2.3 Deposition Process . . . . .	23
2.2.4 Characterization . . . . .	23
2.3 Results and Discussion . . . . .	24
2.4 Conclusion . . . . .	29
<b>III EFFECT OF SUBSTRATE ON Cu<sub>2</sub>ZnSnS<sub>4</sub> MORPHOLOGY IN SUPERCRITICAL CARBON DIOXIDE</b> . . . . .	<b>30</b>

3.1	Introduction . . . . .	30
3.2	Experimental Methods . . . . .	31
3.2.1	Substrate choice and preparation . . . . .	31
3.2.2	CZTS deposition in sc-CO <sub>2</sub> and characterization . . . . .	31
3.3	Results and Discussion . . . . .	32
3.4	Conclusion . . . . .	41
<b>IV</b>	<b>DEPOSITION OF ZnS NANOPARTICLES ON CARBON NANOTUBES . . . . .</b>	<b>43</b>
4.1	Introduction . . . . .	43
4.2	Experimental Methods . . . . .	46
4.2.1	Materials . . . . .	46
4.2.2	ZnS nanoparticle deposition and doping in sc-CO <sub>2</sub> . . . . .	46
4.2.3	Characterization . . . . .	47
4.3	Results and Discussion . . . . .	47
4.3.1	Nanoparticle size and morphology . . . . .	52
4.3.2	Optical properties . . . . .	55
4.4	Conclusion . . . . .	59
<b>V</b>	<b>CONTROLLING DEPOSITION OF SILVER NANOPARTICLES IN SUPERCRITICAL CARBON DIOXIDE . . . . .</b>	<b>61</b>
5.1	Introduction . . . . .	61
5.2	Experimental Methods . . . . .	64
5.2.1	Materials . . . . .	64
5.2.2	Surface pretreatment . . . . .	64
5.2.3	Nanoparticle deposition . . . . .	64
5.2.4	Characterization . . . . .	65
5.3	Results and Discussion . . . . .	66
5.3.1	Scanning electron microscopy . . . . .	66
5.3.2	Analysis of kinetics . . . . .	70
5.3.3	X-ray photoelectron spectroscopy . . . . .	73

5.3.4	Transmission electron microscopy and selected area electron diffraction . . . . .	74
5.3.5	X-ray diffraction . . . . .	74
5.3.6	Surface enhanced Raman spectroscopy . . . . .	75
5.3.7	Heterogeneous AgNP deposition on substrates in sc-CO <sub>2</sub> . . . . .	78
5.3.8	SERS application of AgNP coated substrates fabricated in sc-CO <sub>2</sub> . . . . .	82
5.4	Conclusion . . . . .	84
<b>VI LAYERS OF EXPERIMENT WITH ADAPTIVE COMBINED DESIGN . . . . .</b>		<b>86</b>
6.1	Introduction . . . . .	86
6.2	Methodology . . . . .	90
6.2.1	Model Selection . . . . .	91
6.2.2	Assessment of Model Accuracy . . . . .	92
6.2.3	Selection of Next Layer . . . . .	93
6.2.4	Adaptive Combined Design . . . . .	95
6.3	Experimental Methods . . . . .	96
6.4	Results and Discussion . . . . .	97
6.5	Conclusion . . . . .	105
<b>VII A SECOND CASE STUDY FOR LAYERS OF EXPERIMENT WITH ADAPTIVE COMBINED DESIGN . . . . .</b>		<b>106</b>
7.1	Introduction . . . . .	106
7.2	Experimental Methods . . . . .	106
7.2.1	Layers of Experiments with Adaptive Combined Design . . . . .	106
7.2.2	Experimental procedure . . . . .	108
7.3	Results and Discussion . . . . .	109
7.3.1	First layer . . . . .	109
7.3.2	Second layer . . . . .	109
7.4	Conclusion . . . . .	113

<b>VIII</b>	<b>INITIAL EXPERIMENTAL DESIGN INCORPORATING PRIOR DATA, ENGINEERING MODELS, AND EXPERT OPINION . . . . .</b>	<b>115</b>
8.1	Introduction . . . . .	115
8.2	Methodology . . . . .	119
8.2.1	Summary of the IED methodology . . . . .	119
8.2.2	Survey for expert conjecture . . . . .	119
8.2.3	Choosing the experimental design window . . . . .	121
8.2.4	Building individual models based on expert opinion and prior data . . . . .	122
8.2.5	Building a unified model . . . . .	123
8.2.6	Choosing the experimental design points . . . . .	124
8.3	Experimental Methods . . . . .	125
8.3.1	Materials . . . . .	125
8.3.2	Nanoparticle deposition . . . . .	125
8.3.3	Characterization . . . . .	126
8.4	Results and Discussion . . . . .	126
8.4.1	Plan for potential follow-up experiments . . . . .	130
8.5	Conclusion . . . . .	137
<b>IX</b>	<b>CONCLUSIONS AND FUTURE WORK . . . . .</b>	<b>139</b>
9.1	Process-structure-property investigations . . . . .	140
9.2	Novel experimental design approaches . . . . .	143
<b>APPENDIX A</b>	<b>— XRD AND RAMAN DATA FOR CZTS DEPOSITED ON VARIOUS SUBSTRATES . . . . .</b>	<b>146</b>
<b>APPENDIX B</b>	<b>— SURVEY FOR INITIAL DESIGN OF EXPERIMENTS . . . . .</b>	<b>151</b>
<b>APPENDIX C</b>	<b>— EDX SPECTRUM FOR IRIDIUM NANOPARTICLES ON SILICON . . . . .</b>	<b>155</b>
<b>APPENDIX D</b>	<b>— EXPERTS' COMMENTS FOR SURVEY . . . . .</b>	<b>156</b>
<b>REFERENCES</b>	<b>. . . . .</b>	<b>159</b>

VITA . . . . . 202

## LIST OF TABLES

1	Comparison of properties of liquid phase, supercritical phase, and gas phase fluid. From <i>Science</i> , Vol. 294, Blackburn et al., Deposition of conformal copper and nickel films from supercritical carbon dioxide, 141-145. Reprinted with permission from AAAS . . . . .	7
2	Atomic ratios of $\text{Cu}_2\text{ZnSnS}_4$ particles as measured by energy dispersive X-ray spectroscopy . . . . .	26
3	Atomic composition of ZnS nanocomposites synthesized in $\text{sc-CO}_2$ as measured by EDX . . . . .	49
4	Band gap and peak maxima data from Tauc plot and PL spectroscopy	51
5	Descriptive statistics for AgNPs deposited on plasma treated silicon and glass in the temperature range $60\text{ }^\circ\text{C}$ – $180\text{ }^\circ\text{C}$ . Replicates are separated by commas; standard deviations are included for mean nanoparticle size . . . . .	67
6	Descriptive statistics for AgNPs deposited on HCl treated silicon and glass at different reaction temperatures. Replicates are separated by commas; standard deviations are included for mean nanoparticle size	68
7	$R^2$ values and activation energy values for (a) plasma-treated silicon, (b) plasma-treated glass, (c) HCl-treated silicon, and (d) HCl-treated glass; 95% confidence intervals are included for activation energy values on the model prediction of the mean . . . . .	71
8	Surface atomic percent composition of plasma and HCl treated silicon and glass substrates as measured by XPS before AgNP deposition . .	73
9	SERS enhancement factors for AgNPs coated surfaces synthesized at $60\text{ }^\circ\text{C}$ , $120\text{ }^\circ\text{C}$ , and $180\text{ }^\circ\text{C}$ . Replicates are separated by commas in the table . . . . .	77
10	Results of first layer of experiments . . . . .	97
11	Model selection criteria for first layer . . . . .	98
12	Results of second layer of experiments . . . . .	99
13	Model selection criteria for second layer . . . . .	100
14	Results of experiments and model selection criteria in first layer . . .	109
15	Results of experiments and model selection criteria in second layer . .	110

16	Expert survey responses for conjectures of the design window and confidence in conjecture for IrNP deposition in sc-CO <sub>2</sub> . Intervals denote 95% confidence interval . . . . .	127
17	Expert conjectures for activation energy and nanoparticle size at the midpoint of the conjectured design window. Intervals denote 95% confidence interval . . . . .	127
18	Confidence in Arrhenius model structure . . . . .	127
19	Conjectured parameters and final parameters after Gibbs sampling of Bayesian hierarchical model . . . . .	128
20	Confidence in Arrhenius model structure . . . . .	128
21	Experimental data for IrNP deposited on Si wafer surface in sc-CO <sub>2</sub> .	131
22	Table of experimental results . . . . .	152

## LIST OF FIGURES

1	TEM image of gold nanocages used in cancer therapy research. Reprinted from <i>Nanomedicine: Nanotechnology, Biology, and Medicine</i> , Vol. 8, Chen et al., Gold nanocages as contrast agents for two-photon luminescence endomicroscopy imaging, 1267-1270, Copyright 2012, with permission from Elsevier . . . . .	3
2	Phase diagram of carbon dioxide . . . . .	6
3	Overall organization of this thesis . . . . .	18
4	NMR spectrum for Sn(dedc) <sub>4</sub> . . . . .	21
5	TGA analysis for Sn(dedc) <sub>4</sub> . . . . .	22
6	Schematic of supercritical carbon dioxide continuous flow reactor system	22
7	EDX spectrum of CZTS particles on silicon wafer substrate . . . . .	24
8	Scanning electron microscope images of CZTS particles formed on a silicon wafer via the sc-CO <sub>2</sub> CFR process. Magnification increases from (a) 2,000×, (b) 5,000×, and (c) 50,000×. White boxes indicate regions viewed at higher magnification in (b) and (c). (d) Cross section image of CZTS on silicon . . . . .	25
9	Chemical mapping of CZTS particles on a silicon substrate by energy dispersive X-ray spectroscopy. Scale bar: 15 μm . . . . .	25
10	X-ray diffraction pattern for CZTS particles fabricated on silicon via the sc-CO <sub>2</sub> CFR process . . . . .	27
11	Raman spectrum for CZTS particles deposited on silicon by the sc-CO <sub>2</sub> CFR process. The peak at 337 cm <sup>-1</sup> corresponds to CZTS . . . . .	28
12	UV/Vis spectrum of CZTS particles. The inset shows the corresponding Tauc plot, and the band gap is estimated where the dashed line intersects the abscissa . . . . .	28
13	(a) Top-down and (b) cross section view of CZTS particles deposited on oxygen plasma-cleaned Si surface . . . . .	33
14	Top-down view of CZTS samples fabricated on Au, Ge, Mo, and SiO <sub>2</sub> substrates . . . . .	33
15	Cross section view of CZTS samples fabricated on Au, Ge, Mo, and SiO <sub>2</sub> substrates . . . . .	34
16	Top-down view of CZTS samples fabricated on Au, Ge, Mo, and SiO <sub>2</sub> substrates at 1 minute reaction time . . . . .	34

17	Cross section view of CZTS samples fabricated on Au, Ge, Mo, and SiO <sub>2</sub> substrates at 1 minute reaction time . . . . .	35
18	Top-down view of CZTS samples fabricated on Au, Ge, Mo, and SiO <sub>2</sub> substrates at low concentration . . . . .	35
19	Cross section view of CZTS samples fabricated on Au, Ge, Mo, and SiO <sub>2</sub> substrates at low concentration . . . . .	36
20	Top-down view of CZTS samples fabricated on Au, Ge, Mo, and SiO <sub>2</sub> substrates at 400 °C . . . . .	36
21	Cross section view of CZTS samples fabricated on Au, Ge, Mo, and SiO <sub>2</sub> substrates at 400 °C . . . . .	37
22	Proposed mechanism for CZTS thin film and particle formation in sc-CO <sub>2</sub> . . . . .	38
23	XPS spectra for oxidized and non-oxidized Mo substrate . . . . .	39
24	Cross section image of molybdenum oxide layer on Mo substrate . . . . .	40
25	Cross section image of CZTS deposited on MoO <sub>x</sub> . . . . .	41
26	ATR-FTIR spectra of Mo and MoO <sub>x</sub> substrates used for CZTS deposition in sc-CO <sub>2</sub> . . . . .	41
27	(a)-(b) SEM images of ZnS nanoparticles deposited on carbon nanotubes (c)-(d) SEM image of f-ZnS nanoparticles synthesized in the absence of any substrate . . . . .	48
28	TEM image of ZnS NPs immobilized on CNTs . . . . .	48
29	Histograms of (a) 16.9 ± 1.9 nm mean size and (b) 209 ± 24 nm mean size ZnS nanoparticles on CNTs and (c) histogram of 178 ± 15 nm mean size f-ZnS NPs synthesized in the absence of any substrate . . . . .	49
30	XRD spectrum of ZnS-CNT nanocomposite, illustrating the characteristic peaks for the wurtzite structure of ZnS . . . . .	50
31	UV-vis absorption spectra of ZnS-CNT and Mn:ZnS-CNT nanocomposites . . . . .	52
32	Tauc plots corresponding to UV-vis spectra of (a) ZnS, (b) Mn:ZnS-CNT, and (c) f-ZnS in Figure 31 . . . . .	53
33	Photoluminescence spectra of ZnS-CNT and Mn:ZnS-CNT nanocomposites . . . . .	53

34	Energy level diagrams for the ZnS-CNT and Mn:ZnS-CNT nanocomposites synthesized in sc-CO <sub>2</sub> (1) Photon absorption and exciton generation (2) Hole promotion to a hole trap state (3) Nonradiative decay into electron trap state (4) Blue light emission as an electron recombines with a hole (5) Nonradiative decay to a Mn <i>d</i> -state (6) Nonradiative decay to a Mn <i>d</i> -state (7) Hole promotion into a Mn <i>d</i> -state (8) Orange light emission as an electron recombines with a hole . . .	56
35	SEM images of AgNPs deposited on plasma treated silicon at (a) 60 °C, (b) 120 °C, and (c) 180 °C and plasma treated glass at (d) 60 °C, (e) 120 °C, and (f) 180 °C . . . . .	66
36	Histograms for AgNPs deposited on plasma treated (a) silicon and (b) glass surfaces in the temperature range 60 °C–180 °C . . . . .	67
37	SEM images of AgNPs deposited on HCl treated silicon at (a) 60 °C, (b) 120 °C, and (c) 180 °C and HCl treated glass at (d) 60 °C, (e) 120 °C, and (f) 180 °C . . . . .	68
38	Histograms for AgNPs deposited on HCl treated (a) silicon and (b) glass surfaces in the temperature range 60 °C–180 °C . . . . .	69
39	EDX spectra of AgNPs deposited on silicon and glass substrates . .	70
40	Arrhenius plots for AgNPs deposited on (a) plasma treated silicon, (b) plasma treated glass, (c) HCl treated silicon, and (d) HCl treated glass. Dotted lines indicate the 95% confidence interval on the model prediction of the mean . . . . .	72
41	Combinations of AgNP mean diameters and densities that can be achieved in the sc-CO <sub>2</sub> system. R <sup>2</sup> values for the fitted lines are included in the legend . . . . .	72
42	TEM image of AgNPs deposited on HCl treated silicon 60 °C, removed and placed on lacy carbon TEM grid. Inset shows the SAED pattern indicating fcc crystal structure . . . . .	74
43	XRD diffractogram of AgNPs deposited on (a) plasma treated and (b) HCl treated glass. Spectra were offset slightly to ease interpretation	75
44	SERS spectra of 1×10 <sup>-6</sup> R6G on AgNPs deposited at 120 °C on plasma treated silicon as well as controls lacking either R6G or AgNPs. R6G peaks are assigned . . . . .	76
45	SERS spectra of 1×10 <sup>-6</sup> R6G on AgNPs deposited on (a) plasma treated silicon, (b) plasma treated glass, (c) HCl treated silicon, and (d) HCl treated glass . . . . .	76

46	Layers of Experiments with Adaptive Combined Design Algorithm. The uncertainty metric $L^*$ is used to assess model accuracy in each layer of experiments . . . . .	90
47	Typical SEM image used for data collection of AgNP size on silicon wafer . . . . .	97
48	Linear model fit of data collected in the first layer of experiments with 95% confidence interval and the associated $L$ metric . . . . .	98
49	Histogram of center points calculated from bootstrapping and using Eq. 14 . . . . .	99
50	Plot of $\psi(r)$ versus $r$ using Eq.15 on the data shown in Figure 49; the horizontal dashed line indicates the $\alpha = 0.98$ confidence level and the vertical line corresponds to the window size of the next layer for this confidence level . . . . .	100
51	Plot of linear and quadratic models fit in second layer of experiments	101
52	Linear model fit of data collected in first LoE with 95% confidence intervals and $L$ metric . . . . .	110
53	(a) Histogram of potential center points (b) $\psi(r)$ vs. $r$ ; dashed lines indicate 99% confidence level and window size . . . . .	111
54	Linear model fit of data collected in second LoE with 95% confidence interval and $L$ metric . . . . .	111
55	Typical SEM image of silver nanoparticles on silicon wafer surface . .	112
56	Arrhenius plot of prior data from AgNP deposition experiments in sc-CO <sub>2</sub> [43, 44] . . . . .	120
57	Individual expert models and unified model for IrNP deposition . . .	129
58	Potential experimental designs as a function of tuning parameter $\gamma$ .	130
59	Typical SEM image of IrNP deposited on Si wafer surface at $T = 149$ °C . . . . .	131
60	Arrhenius plots for global model and local model (incorporating points from 131 °C to 184 °C) shown in Table 21 . . . . .	131
61	Plot of $L$ metric with local Arrhenius model, confidence interval, and target IrNP size . . . . .	133
62	XRD spectra for samples fabricated in the base case conditions . . .	146
63	Raman spectra for samples fabricated in the base case conditions . .	146
64	XRD spectra for samples fabricated at 1 minute reaction time . . . .	147

65	Raman spectra for samples fabricated at 1 minute reaction time . . .	147
66	XRD spectra for samples fabricated at low concentration . . . . .	148
67	Raman spectra for samples fabricated at low concentration . . . . .	148
68	XRD spectra for samples fabricated at 400 °C . . . . .	149
69	Raman spectra for samples fabricated at 400 °C . . . . .	149
70	XRD spectrum for CZTS deposited on MoO <sub>x</sub> surface . . . . .	150
71	Raman spectrum for CZTS deposited on MoO <sub>x</sub> surface . . . . .	150
72	Plot of experimental data for mean nanoparticle size vs. temperature	152
73	Arrhenius plot of experimental data . . . . .	153
74	EDX spectra of Ir nanoparticles deposited on Si surface . . . . .	155

# SUMMARY

This thesis presents investigations into the design and synthesis of nanomaterials in supercritical carbon dioxide (sc-CO<sub>2</sub>) as well as novel experimental design methodologies. First, the process-structure-property relationships are studied for the deposition of materials from organometallic precursors in sc-CO<sub>2</sub>. The materials that were investigated in these studies were: (1) the semiconductor material copper zinc tin sulfide (Cu<sub>2</sub>ZnSnS<sub>4</sub>, or CZTS), which has application in solar energy capture; (2) zinc sulfide nanoparticles deposited onto carbon nanotubes, which have application in optoelectronics; and (3) silver nanoparticles deposited on silicon and glass wafer surfaces, which find application as biosensors via surface enhanced Raman spectroscopy. Next, two novel experimental design methodologies were implemented. The first is termed layers of experiment with adaptive combined design (LoE/ACD), which efficiently optimizes a process that is expensive and time consuming to study by zooming in on the process optimum through successive layers. The mean silver nanoparticle size was optimized as a function of temperature in the sc-CO<sub>2</sub> system using the LoE/ACD approach. The second experimental design methodology is called initial experimental design (IED). The IED methodology was developed to choose the first round of experiments for a system that is expensive to study (in terms of time and money), poorly understood, and possesses a related, non-identical system that is well-studied. The IED approach was used to optimize the mean iridium nanoparticle size as a function of temperature given expert opinion, prior data, and an engineering model for silver nanoparticles synthesized in sc-CO<sub>2</sub>.

# CHAPTER I

## INTRODUCTION

### *1.1 Nanotechnology Background*

#### **1.1.1 Brief history of nanotechnology and its applications**

Nanoscience is the study of structures that have one physical dimension at the nanoscale (i.e., between 1–100 nm), while nanotechnology is the application of nanoscience to solve challenges in the real world [20, 36, 247, 307]. The first known application of nanotechnology was in stained glass windows used in churches in medieval Europe [81, 84]. Glass artisans mixed gold chloride into molten glass, unknowingly reducing the gold complexes to form small gold nanoparticles [74, 309]. By virtue of their small size, the gold nanoparticles exhibited a surface plasmon resonance effect to imbue the glass with a ruby red color [83, 151, 209]. In 1857, Michael Faraday first reported that colloidal gold exhibited significantly different properties compared to bulk gold [88, 213]. He attributed this observation to differences in the physical size of the particles, although he did not elucidate the mechanism; nonetheless, his observation was the first step toward understanding the differences in behavior of matter at the nanoscale. The prescient physicist Richard P. Feynman is credited with advancing the cause of nanotechnology in a 1959 lecture entitled, “There’s Plenty of Room at the Bottom,” by asking the question: “What would happen if we could arrange the atoms one by one the way we want them?” [93, 141]. Nonetheless, not until 1974 was the term “nanotechnology” coined, and this field has developed rapidly with the invention of various instruments such as the scanning tunneling microscope, transmission electron microscope, and atomic force microscope, which are able to investigate and manipulate atoms to control nanoscale phenomena [24, 34, 80, 185, 280, 284, 285].

As of 2012, the United States has invested 3.7 billion dollars in nanotechnology research through the National Nanotechnology Initiative, highlighting the potential impact of this field in several areas of science and engineering [240]. For instance, in medicine, nanoparticles of gold, silver, and other metals have been leveraged for use in photodynamic therapy [19, 202]. Figure 1 shows a TEM image of gold nanocages used for cancer therapy [50]. This application of nanotechnology may allow physicians to selectively target tumors and avoid the pitfalls of traditional chemotherapy and radiotherapy [37, 300]. In energy-related research, nanotechnology has found multiple applications [154, 162, 203]. Nanowires of silicon and germanium have been grown on semiconductor surfaces to develop high efficiency next generation solar cell devices [117, 126]. Nanowires are nanostructures that have an aspect ratio (nanowire length to diameter) of 100 or more [196]. These nanowires take advantage of quantum confinement effects in order to manipulate the optical properties of the nanostructures while also increasing the absorption of light through multiple reflections and scattering/confinement within the nanowire array [218, 222]. Similarly, quantum dots have been studied because of quantum confinement effects that can be used to manipulate the band gap energies of light absorbing nanoparticles such as CdS or CdSe [160, 184]. Chemical and environmental sensors have also benefited from nanotechnology [143]. Nanoparticles have been leveraged to develop highly sensitive detection techniques such as surface enhanced Raman spectroscopy [188, 327]. It is clear that there are many possible types of nanostructures that have applications in science, engineering, medicine, and other fields. Consequently, it is critical that an understanding of the relationship between various methods used to fabricate these nanostructures and their resulting properties be established in order to effectively design nanomaterials to allow nanotechnology to realize its full potential.

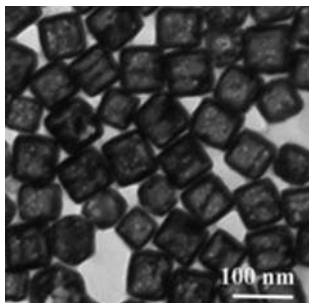


Figure 1: TEM image of gold nanocages used in cancer therapy research. Reprinted from *Nanomedicine: Nanotechnology, Biology, and Medicine*, Vol. 8, Chen et al., Gold nanocages as contrast agents for two-photon luminescence endomicroscopy imaging, 1267-1270, Copyright 2012, with permission from Elsevier

### 1.1.2 Techniques for fabricating nanostructures

A myriad of methods exist for fabricating nanostructures, and these generally fall into two categories: top-down approaches and bottom-up approaches [174, 189, 212]. In the top-down approach, a bulk sample is manipulated to remove material, leaving behind the nanoscale structure [217, 258, 299]. For example, ion beam sputtering is used in the field of microelectronics to generate micro- and nanoscale patterns that are vital for high performance electronic devices [100, 163]. The highly energetic ion beam transfers energy to a material, physically ejecting atoms to yield nanosized features in the surface [97, 101, 157]. Similar to ion beam sputtering, laser ablation with visible or ultraviolet light can be used to selectively etch organic polymers as well as microelectronic materials [85, 271]. In this method, light impinges upon the material and transfers energy to atoms on the surface, which are then ejected [140, 263]. Finally, plasmas can be used to etch away unwanted material from materials such as copper or silicon to create nanochannels for use in electronic devices [71, 166]. For example, plasmas can be used to selectively etch copper by forming volatile copper compounds, which are removed from the surface to leave behind the desired nanoscale structures [55, 155, 314].

On the other hand, bottom-up approaches focus on fabricating nanostructures

from atomic or molecular precursors and thereby “build up” the nanostructure [40, 47]. For instance, in chemical vapor deposition (CVD), precursors are transported onto a surface and react in a nucleation and growth process [123, 288]. A thin film is then gradually fabricated by this bottom up approach, with atoms being successively added to the growing thin film surface [200, 224]. Atomic layer deposition (ALD) is similar to CVD in that both approaches use chemical precursors [159, 237]. However, in ALD, a film or nanostructure is fabricated with atomic layer precision by cycling the precursor deposition, reaction, and purge steps [54, 237]. ALD approaches yield much greater control over the film deposition process, but it is also very slow, depositing one layer of atoms per cycle. In CVD methods, the thin film fabrication process proceeds more rapidly than ALD but affords less control over the film formation process.

In colloidal synthesis, precursors react in solution to form nanoparticles such as gold, silver, or copper [110, 112, 158]. The precursors react to form critically-sized nuclei of the metal nanoparticles, and continue to grow until the reaction is terminated by quenching [176, 246, 312]. The reaction mechanism usually proceeds by reducing the cationic metal species in the precursor to the zero-valent metal state; reducing agents such as sodium borohydride or hydrazine are commonly used for this purpose [176, 246, 312]. The resulting colloidal nanoparticles are then collected and separated to recover the metallic nanoparticles [14, 107]. In vapor-liquid-solid (VLS) growth techniques, another example of a bottom-up approach, it is possible to fabricate anisotropic structures such as nanowires [223, 230]. Nanowire crystal growth from a vapor precursor on a solid is usually very slow; however, in VLS synthesis methods, a catalyst nanoparticle (e.g., gold) is used to accelerate the rate of reaction [116, 301]. A classical example of this process is silicon nanowire growth [103]. In this technique, a vapor precursor is brought into contact with a gold nanosized droplet above the eutectic point; a reaction occurs, depositing silicon from the precursor beneath the gold nanoparticle, and the nanowire increases in length axially [113, 287].

Within the many synthesis techniques that have been developed for nanotechnology, a subset of these methods attempts to apply the techniques of green chemistry [130]. Green chemistry is the practice of chemistry and chemical engineering in such a way as to minimize the effects of a chemical process on the environment and society [8]. For instance, if a product were synthesized using an environmentally unfriendly or hazardous chemical, such as an organic solvent, the principles of green chemistry suggest replacing this chemical with an alternative that is more environmentally friendly [256]. One such example of a green application of nanotechnology is the synthesis of Au, Ag, and Au-Ag alloy nanoparticles of size  $< 10$  nm. Traditional syntheses of these metallic nanoparticles rely on harsh reducing agents (sodium borohydride or lithium borohydride) and non-sustainable stabilizing agents (polyvinyl pyrrolidone) [49, 59, 132, 158, 241]. In contrast, a green approach to fabricating these nanomaterials implemented glucose as a reducing agent and starch as the stabilizing agent [195, 233].

Another method that has been explored as a green alternative to current methods for nanomaterials synthesis is supercritical carbon dioxide (sc-CO<sub>2</sub>) processing [303]. In this technique, the sc-CO<sub>2</sub> is used as the reaction medium and replaces the organic solvent [208]. Supercritical CO<sub>2</sub> synthesis is a greener choice compared to organic solvents because it provides a use for captured and recycled carbon dioxide, is nontoxic, nonflammable, and is readily available for use.

### **1.1.3 Supercritical carbon dioxide for nanostructure synthesis**

Supercritical CO<sub>2</sub> is a medium which has attracted significant attention for the synthesis of nanostructures. Supercritical CO<sub>2</sub> is carbon dioxide that has been elevated above its critical pressure (72.9 atm) and critical temperature (31.1 °C); the phase diagram for carbon dioxide is shown in Figure 2 [261]. Before finding use in nanoparticle synthesis at the laboratory scale, sc-CO<sub>2</sub> was used frequently for extraction. For

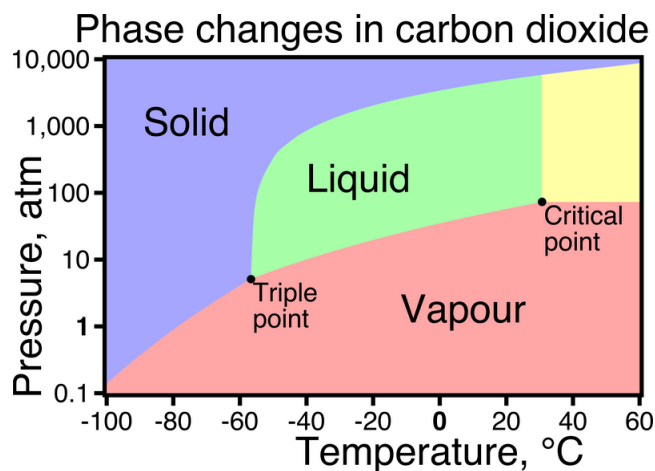


Figure 2: Phase diagram of carbon dioxide

example, caffeine is removed from coffee beans using sc-CO<sub>2</sub> [181, 221]. Similarly, sc-CO<sub>2</sub> has been applied in the extraction of chemicals used in the pharmaceutical industry [183, 269]. Supercritical-CO<sub>2</sub> can also be used for the extraction of heavy metals from liquids using chelating agents that can be dissolved in sc-CO<sub>2</sub> [260, 296].

Carbon dioxide in the supercritical state has several attributes that make it ideal for use as a solvent to solubilize precursors and synthesize nanoparticles. First, it has the characteristics of both a liquid and a gas [261]. Like a liquid, sc-CO<sub>2</sub> can dissolve precursor compounds and thus be used as a solvent from which nanoparticles can be formulated [261]. Like a gas, sc-CO<sub>2</sub> has high diffusivity and low viscosity, allowing the sc-CO<sub>2</sub> to penetrate into high aspect ratio structures and therefore transport precursor molecules into these constrained spaces where they can form nanoparticles or nanostructures [261]. These properties are summarized in Table 1 [25]. Furthermore, the characteristics of sc-CO<sub>2</sub> can be tuned by modulating fluid temperature and pressure, yielding a more liquid-like or gas-like medium depending upon the specific conditions [303].

Supercritical CO<sub>2</sub> has been implemented in many ways for the synthesis of nanoparticles and other nanostructures. In the reverse microemulsion method, water soluble precursors (such as chlorides or nitrates) are dissolved in water droplets which are

Table 1: Comparison of properties of liquid phase, supercritical phase, and gas phase fluid. From *Science*, Vol. 294, Blackburn et al., Deposition of conformal copper and nickel films from supercritical carbon dioxide, 141-145. Reprinted with permission from AAAS

Property	Liquid phase	Supercritical phase	Gas phase
Density (g/cm <sup>3</sup> )	1	0.1	10 <sup>-3</sup>
Viscosity (Pa·s)	10 <sup>-3</sup>	10 <sup>-4</sup> – 10 <sup>-5</sup>	10 <sup>-5</sup>
Diffusivity (cm <sup>2</sup> /s)	10 <sup>-5</sup>	10 <sup>-3</sup>	10 <sup>-1</sup>
Surface tension (dynes/cm)	20 – 0	0	0
Precursor conc. (M)	10 <sup>-3</sup>	10 <sup>-5</sup>	10 <sup>-8</sup>

suspended throughout the sc-CO<sub>2</sub> phase, forming the microemulsion [206, 207]. This method has been used to synthesize nanoparticles of copper, silver, and zinc sulfide which are not supported on any substrate [206, 207]. This methodology has the advantage of control over nanoparticle size; however, environmentally unfriendly surfactants must be used to establish the reverse microemulsion [206, 207].

Nanoparticles of platinum have been directly deposited onto carbon nanotubes (CNTs) from organometallic platinum precursors for use in fuel cell applications [10]. The advantageous transport properties of sc-CO<sub>2</sub> facilitate the decoration of the CNT surfaces with Pt nanoparticles, since the CNT network possesses high aspect ratio and high tortuosity in the structure. The precursor was reduced via hydrogen to facilitate nanoparticle deposition; nanoparticles were decorated on the surface of the CNTs with sizes in the range of 5 – 10 nm. The hypothesized mechanism for this reaction is one where carboxyl functional groups on the functionalized CNTs act as reactive nucleation sites for deposition of Pt from the organometallic precursor [10, 167, 171].

Thin films have also been synthesized using sc-CO<sub>2</sub>. For example, copper and nickel thin films have been deposited onto silicon substrates for applications in microelectronics [39, 208]. These efforts have also leveraged the advantageous transport properties of sc-CO<sub>2</sub> to deposit the thin films into nanosized trenches where

liquid solvents would not be as successful due to limited diffusivity and surface tension [25]. The mechanism of Cu film deposition in sc-CO<sub>2</sub> has been explored by Zong and Watkins [335]. A hypothesized Langmuir-Hinshelwood heterogeneous reaction mechanism was proposed and fit for the deposition of the Cu thin film from a bis(2,2,7-trimethyloctane-3,5-dionato)copper(II) precursor. The effective activation energy was estimated to be 51.9 kJ/mol, and the thin film deposition proceeded at a rate of 5 nm/min.

Nanowires have also been synthesized using sc-CO<sub>2</sub>. In one method, anodic aluminum oxide (AAO) membranes were used as templates for nanowire fabrication [41, 58, 298]. These templates possess a high aspect ratio: they are generally 50–200 microns thick (corresponding to the resulting nanowire length), and have pore diameters of 5–100 nm (corresponding to the resulting nanowire diameter). Upon reaction, the pores in the AAO templates are filled with deposited metal. The AAO is then carefully etched away using NaOH to reveal the nanowires inside the AAO pores. In a similar methodology, carbon nanotubes were used instead of AAO as the template for nanowire growth [324]. Again, the advantageous transport properties of sc-CO<sub>2</sub> allow it to efficiently move precursor compounds into the high aspect ratio pores of the carbon nanotubes.

## ***1.2 Background on experimental design***

### **1.2.1 Brief history of experimental design**

Process systems engineering is an approach that combines experimental data with models or simulations to efficiently design, optimize, and/or control a system of interest [109]. The field of process systems engineering has been developed to address challenges in many areas of chemical engineering such as separations and process optimization [108, 178, 194]. Some areas within process systems engineering overlap

significantly with approaches used in statistics and industrial engineering. For example, the approach known as design of experiments (DoE, or experimental design) is a powerful tool for studying chemical systems in engineering that is also used in process systems engineering, statistics, and industrial engineering [9, 226]. Experimental design was first formalized by the work of Ronald A. Fisher; this work applied statistical methods to the different methods of growing and rotating crops in agricultural application [95]. Dr. Fisher’s seminal work, *The Design of Experiments*, laid the foundation for DoE approaches and was a major contribution to statistics in that it outlined the major ingredients of experimental design: replication, randomization, blocking, factorial experiments, and the analysis of variance (ANOVA) [95].

Replication is a vital part of experimental research. Experimental results and measurements can be influenced significantly by uncertainty and variation in the system of interest [295]. Replication of experimental results is necessary to ensure that an experimental result is due to a significant effect of the independent variable on the system and not due to uncontrollable variation [295]. Randomization is a term applied to assigning the treatments of an experiment randomly across groups to be studied [79]. The classical example of randomization relates to drug trials in the clinical setting: treatments (either the experimental drug or a placebo) are randomly assigned to patients [7]. The practice of randomization is used to reduce the influence of unknown, uncontrollable variables that cannot or were not controlled in the initial experimental design [30, 295]. Similar to randomization, the technique of blocking is used to reduce variation in an experimental design [30]. However, blocking achieves this goal by identifying sources of variation that occur systematically in similar groups in a trial and reduces this source of variation [30].

Factorial experiments can take advantage of each of these three techniques for reducing variability. However, factorial experiments possess an additional advantage: a factorial design is able to study the effect of more than one independent variable at

a time [29]. Factorial experimental designs were developed to increase the efficiency of a study, decrease the number of experiments necessary when studying the effects of multiple independent variables, and test for interaction effects among variables. However, such studies do not provide insight into any fundamental phenomena occurring in the system. For example, it would be possible to study the effect of both temperature and reaction time on yield in a chemical process at the same time, instead of simply studying the effect of each effect in a one-factor-at-a-time design [57]. Through an ANOVA analysis, the effects due to each individual variable (main effects) and those due to interplay between variables (interaction effects) are simultaneously tested to determine which have statistically significant influence on the system and which are due to random chance [190, 295].

Moreover, experimental design studies can be performed with alternative objectives. For example, if a model is postulated for a system, experiments must be conducted to fit the model and estimate the model's parameters. Optimal designs have been developed to specifically address this issue [52]. Alphabet optimal designs (e.g., A-optimal or D-optimal) are optimal with respect to some type of statistical criterion related to the model structure [32, 215]. For example, a D-optimal design seeks to minimize the variance on the parameter estimates [191]. A non-optimal design would result in an experimental design that requires additional experiments compared to the optimal design, leading to inefficiency in data collection. Additionally, the non-optimal design may not minimize the variance on the parameter estimates compared to the D-optimal design.

If the goal is to optimize the response of a system (instead of optimizing a statistical criterion), an alternative strategy must be used. A technique termed response surface methodology (RSM) was developed by Box and Wilson in 1951 to optimize system response [33]. The RSM methodology uses a steepest ascent/descent method to find the process optimum, and the response function is usually modeled as a

quadratic polynomial [33, 193, 313]. This approach is useful if the objective function is convex; however, if the objective function is non-convex, it is possible that local optima may be mistakenly identified that are not global optima [125, 197]. Moreover, an infeasible number of experiments may be necessary if the initial design region is selected poorly (i.e., far away from the process optimum), and the size of the ascent/descent step must be selected using the best judgment of the investigator [68, 86, 199].

Traditional statistical designs usually attempt to measure the effect of independent variables on the *mean* response of a system. However, for many applications, the mean response is not the only important response; indeed, variation from the mean can also be an important issue to address in experimental design [273]. This is often termed robustness. Genichi Taguchi developed statistical methods, collectively known as “Taguchi methods”, that address this issue [275, 276]. His most important contribution to experimental design and statistics was the introduction of a “loss function” that can quantify the loss of a product’s value as increased variation from the mean occurs during a production process [272, 277]. This variation is considered from many sources, such as the environment, the loss in function and failure of manufacturing components, and uncontrollable variation during a manufacturing process; these are considered noise factors [274]. The Taguchi methods increase the robustness of a manufacturing process, ultimately improving its profit-making ability.

### **1.2.2 Applications of experimental design in nanotechnology research**

The tools developed for experimental design have garnered limited attention and use in nanotechnology research. Factorial designs have been of significant interest. For example, an orthogonal experimental design was implemented to study the effect of different process conditions on electrospinning of polymer nanofibers [61]. Electrospinning is a technique where an electric charge or field is used to controllably

fabricate nanoscale fibers from a polymer solution [73]. Materials manufactured by the electrospinning technique find use in many fields, such as medicine, catalysis, and textiles [67, 69, 251]. There are many process conditions that can affect the characteristics of the nanofibers, and many characteristics of the nanofibers that are important for their use [61]. In this particular factorial design study, the authors used an orthogonal experimental design and regression analysis to determine the effect of solution concentration and polymer molecular weight on nanofiber diameter and percent yield [61]. A significant interaction effect was also observed between these independent variables [61]. This factorial design was successful in quantifying the effect of each process condition on the nanofiber characteristics in a more efficient manner than a one-factor-at-a-time design [61].

A design of experiments approach has also been implemented in the VLS growth of ZnO nanowires [253]. Zinc oxide nanowires have application in solar cells as anti-reflective coatings to decrease light losses due to reflection. In this study, an experimental design was conducted for six factors: time, temperature, thickness of gold layer, mass of ZnO, argon flow rate, and thickness of the gold layer on the substrate [253]. Since there were so many variables to be tested, a fractional factorial design was implemented [253]. Fractional factorial designs have the advantage of decreasing the number of experiments necessary to conduct at the potential cost of missing interaction effects between variables [30]. This fractional factorial design was conducted on these six independent variables to determine which had a significant effect on the diameter of the ZnO nanowires [253]. It was determined that there were main effects from the gold layer thickness, the temperature, and the reaction time, by conducting a total of only 25 experiments [253].

### ***1.3 Challenges in the synthesis and optimization of nanomaterials in sc-CO<sub>2</sub>***

While sc-CO<sub>2</sub> processing has been explored as a method for nanostructure synthesis, there are significant challenges that hinder the implementation of sc-CO<sub>2</sub> in a commercial or industrial setting.

First, the costs associated with such systems are appreciable: there are significant capital costs (high pressure pumps, stainless steel reactors and tubing), energy costs (due to pressurization and heating), and material costs (precursor synthesis and separation) associated with this system. Moreover, characterization of nanomaterial samples from this system can be costly and time-consuming.

Second, the relationship of the process variables available for manipulation during sc-CO<sub>2</sub> synthesis to the resulting nanostructure is not well understood. In addition, the influence of nanostructure on performance of a material is also not well characterized for this system, and *in situ* observation of the system is difficult due to the high pressures and temperatures involved. These relationships are collectively known as process-structure-property (PSP) relationships, and they have not been extensively investigated for this system.

As a result of these two challenges, it is difficult to rigorously study and optimize the sc-CO<sub>2</sub> system using traditional experimental design approaches. Such DoE approaches usually implement a model with many experiments over the entirety of a design region, which is not feasible given the difficulties described above. Moreover, building a mechanistic or empirical model for the sc-CO<sub>2</sub> system is difficult since fundamental understanding of the PSP relationships is lacking.

These challenges and issues are addressed in this thesis by (1) implementing fundamental studies of the PSP relationships for several sc-CO<sub>2</sub> nanomaterial synthesis systems in order to increase understanding of the underlying chemical and physical processes and (2) developing and implementing novel DoE approaches on the sc-CO<sub>2</sub>

system to more efficiently plan experiments for and optimize this system.

#### ***1.4 Summary of thesis objectives and contributions***

This thesis addresses the challenges of sc-CO<sub>2</sub> nanomaterial synthesis in two ways. First, the process-structure-property relationships of nanomaterials synthesized in sc-CO<sub>2</sub> were quantified for several nanomaterials: silver nanoparticles, Cu<sub>2</sub>ZnSnS<sub>4</sub> (CZTS) particles and thin films, and zinc sulfide nanoparticles. The surface chemistry and temperature of the various systems were evaluated for their effects on particle size, density, and morphology. The effects of these observed nanostructures established nanomaterial properties such as band gap energy and spectroscopic response.

Second, two novel experimental design methodologies were developed and implemented to study the sc-CO<sub>2</sub> system. The first experimental design methodology implements a novel Layers of Experiment (LoE) with Adaptive Combined Design (ACD) method to rapidly optimize the deposition of silver nanoparticles in sc-CO<sub>2</sub>. The second experimental design methodology leverages expert knowledge and experimental data to efficiently design a first layer of experiments for a new, unstudied system, which is a common circumstance in nanotechnology research.

In Chapter 2 of this thesis, copper zinc tin sulfide (Cu<sub>2</sub>ZnSnS<sub>4</sub>, or CZTS) particles were synthesized in a continuous flow sc-CO<sub>2</sub> process [45]. CZTS particles are used as a *p*-type semiconductor in solar cell devices. The sc-CO<sub>2</sub> processing method employed represents a significantly greener method for CZTS synthesis compared to the state of the art. The CZTS particles synthesized in the sc-CO<sub>2</sub> method possessed the requisite chemical composition, crystal structure, and optical properties that are deemed important in previous studies of this compound.

In Chapter 3 of this thesis, the influence of the substrate surface chemistry on CZTS nucleation and growth is investigated. The presence of an oxide layer on the substrate promoted the formation of a CZTS thin film, and the influences of

temperature, time, and precursor concentration were studied to investigate how to best control the growth of CZTS thin films and micro/nanoparticles in sc-CO<sub>2</sub>.

In Chapter 4 of this thesis, zinc sulfide nanoparticles were deposited on carbon nanotubes in a one-step batch sc-CO<sub>2</sub> process [46]. Zinc sulfide nanoparticles deposited on carbon nanotubes possess photoluminescent properties. The sc-CO<sub>2</sub> process employed is a potentially greener method for zinc sulfide nanoparticle synthesis compared to the state of the art. Zinc sulfide particles synthesized by this method possessed the requisite chemical composition, crystal structure, and optical properties reported in other studies of zinc sulfide nanoparticles deposited on carbon nanotubes.

In Chapter 5 of this thesis, a study of the PSP relationships during the deposition of silver nanoparticles onto silicon wafer surfaces is described [44]. Silver nanoparticles were deposited from an organometallic precursor onto four types of surfaces: oxygen-plasma treated silicon, oxygen-plasma treated glass, HCl-treated silicon, and HCl-treated glass. A significant effect of surface pretreatment on silver nanoparticle size, density, and morphology was observed, and an Arrhenius model was used to describe the growth of silver nanoparticles as a function of temperature. The varying sizes, densities, and structures of the silver nanoparticle films had a significant effect on the surface enhanced Raman spectroscopy (SERS) of the samples.

In Chapter 6 of this thesis, a Layers of Experiment (LoE) with Adaptive Combined Design (ACD) methodology was implemented to efficiently optimize the deposition of silver nanoparticles on a plasma-cleaned silicon wafer substrate [43]. Rapidly optimizing the sc-CO<sub>2</sub> process is difficult because it is time-consuming to run experiments and characterize films and nanoparticles, expensive in terms of chemicals and energy costs, and has not been extensively explored through mechanistic or empirical modeling studies. The LoE/ACD approach overcomes these challenges to rapidly optimize the sc-CO<sub>2</sub> process by “zooming in” on the process optimum via the LoE approach while using the ACD approach to select the experimental design in each layer. Data

and insight gained from the study in Chapter 5 of this thesis was used to inform the potential design region of this study, and the process optimum was determined by conducting only twelve experiments using the LoE/ACD approach.

In Chapter 7 of this thesis, an additional case study for the synthesis of silver nanoparticles in sc-CO<sub>2</sub> is presented [42]. In this case, the optimum for the synthesis of silver nanoparticles is completely outside the initially selected design region. This case study demonstrates how the LoE/ACD methodology can redirect to find the process optimum. The process optimum was found by conducting only eight experiments.

In Chapter 8 of this thesis, a novel design of experiments methodology is implemented to choose the design points in the initial experimental design. For a new system to be studied in nanotechnology research, it is often unclear how to design the first set of experiments because the system is costly to study in terms of time and money and there is no data previously gathered for the new system. However, there is often a similar system, an “older” process that can be used to help design a first layer of experiments; moreover, opinions of experts in a field can be used as well to help with the initial experimental design. We implement an initial experimental design (IED) methodology to choose design points for the deposition of iridium nanoparticles in sc-CO<sub>2</sub> based on data from and the Arrhenius model developed in Chapter 5 of this thesis; expert opinions gathered via survey were also used in an attempt to facilitate efficient and effective design of this unknown system.

In Chapter 9, the main contributions of this thesis are summarized and future directions for research in these areas are discussed.

Overall, this thesis addresses the PSP relationships for synthesizing nanomaterials in sc-CO<sub>2</sub> while also developing new experimental design methods to apply to nanomaterials synthesis methods that are time-consuming, expensive, and not well studied. These contributions will increase the potential for the sc-CO<sub>2</sub> synthesis of nanomaterials as well as make it more cost-effective for optimization in future studies.

The Venn diagram in Figure 3 illustrates how each chapter falls into either or both of these areas of investigation.

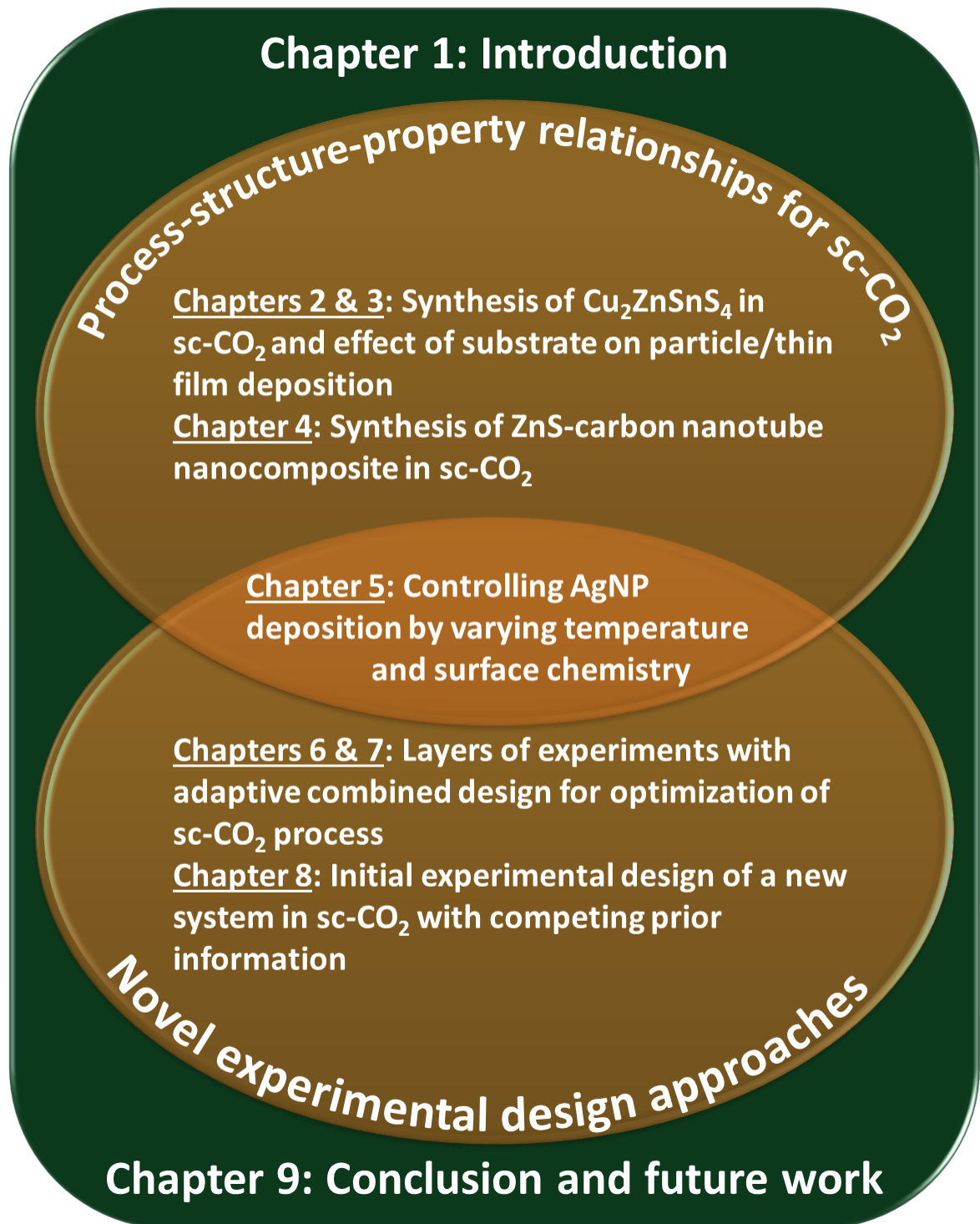


Figure 3: Overall organization of this thesis

## CHAPTER II

### SYNTHESIS OF $\text{Cu}_2\text{ZnSnS}_4$ PARTICLES IN SUPERCRITICAL CARBON DIOXIDE

#### *2.1 Introduction*

Direct band gap thin-film solar cells have attracted attention over the last twenty years as a potential alternative to indirect band gap silicon-based solar cells [254]. In particular, copper indium gallium selenide ( $\text{CuIn}_x\text{Ga}_{1-x}\text{Se}_2$ ; CIGS) thin-film solar cells have achieved solar conversion efficiencies nearing 20% [228]. However, these thin films require the use of expensive, scarce, and toxic compounds, which may inhibit the wide-scale implementation of CIGS devices [145]. A related chalcogenide material, copper zinc tin sulfide ( $\text{Cu}_2\text{ZnSnS}_4$ ; CZTS), has been explored recently because it is composed of relatively less expensive, more abundant, and less toxic materials compared to CIGS.

The highest photoconversion efficiency reported using the CZTS material is 10.1%, although this device was based on CZT(S,Se), which possesses selenium in addition to CZTS and therefore is less “green” than CZTS alone [17]. Sputtering, electrodeposition, and coevaporation of metals followed by sulfurization and annealing are three widely used techniques to fabricate CZTS [250, 252, 279]. Metal dithiocarbamate precursors have been used in liquid and chemical vapor deposition (CVD) processes to form CZTS nanocrystals and thin films directly, without sulfurization [146, 229]. However, none of these techniques are well-suited for depositing CZTS particles or thin films onto structures that possess high aspect ratios or high tortuosity due to solubility and/or transport limitations. Nonetheless, it may still be desirable to decorate high-aspect-ratio/tortuosity nanostructures with CZTS particles or thin films. For

example, CZTS particles could be anchored onto silicon nanowires or carbon nanotubes to improve photoelectrochemical cell performance [245]. Thus, a technique that can efficiently cover high-aspect-ratio/tortuosity nanostructures with CZTS particles or films would be advantageous.

Much work has been performed detailing the deposition of metal thin films and nanoparticles into high-aspect-ratio/tortuous structures by using supercritical carbon dioxide because sc-CO<sub>2</sub> possesses liquid-like solubility and gas-like diffusivity [167, 208]. Furthermore, sc-CO<sub>2</sub> processing is a green, sustainable technique, employing recycled CO<sub>2</sub> as a solvent for precursors. In this chapter of the thesis, a sc-CO<sub>2</sub> continuous-flow reactor (CFR) is employed to deposit CZTS micro- and nanoparticles onto a silicon wafer from metal dithiocarbamate precursors. This work demonstrates that the sustainable sc-CO<sub>2</sub> CFR process is a viable technique for fabricating CZTS particles, establishing the potential for future studies to deposit CZTS in high-aspect-ratio/tortuous nanostructures. Moreover, no postprocessing was required to form the kesterite CZTS phase, although annealing at high temperature and selenization may still be necessary to yield an efficient solar device [17].

## ***2.2 Experimental Methods***

### **2.2.1 Materials**

Toluene (99.99%), methanol (99.99%), acetone (99.99%), isopropyl alcohol (99.99%), copper bis(dimethyldithiocarbamate) (Cu(dmcd)<sub>2</sub>), zinc bis(diethyldithiocarbamate) (Zn(dedc)<sub>2</sub>), sodium diethyldithiocarbamate, tin tetrachloride, chloroform (99.99%), reagent alcohol, and CDCl<sub>3</sub> were purchased from Sigma-Aldrich and used as received. Carbon dioxide gas (99.99%) was purchased from Airgas, GA. Silicon wafers ((100), *p*-type, 10-20 Ω·cm) were purchased from University Wafer and were diced into pieces 1 cm × 5 cm for use as a substrate. Tin tetra(diethyldithiocarbamate) (Sn(dedc)<sub>4</sub>) was synthesized as described by Khare et al. Briefly, a 200 mL solution of 0.375

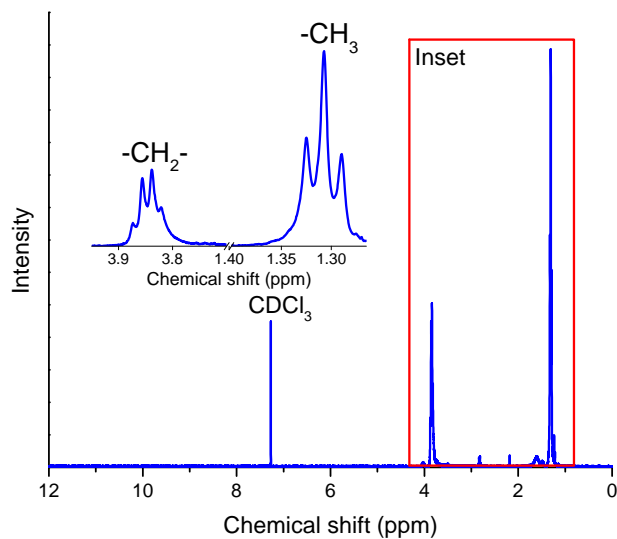


Figure 4: NMR spectrum for  $\text{Sn}(\text{dedc})_4$

M sodium diethyldithiocarbamate was prepared in reagent alcohol. This was added dropwise to 2.5 g of tin tetrachloride dissolved in 50 mL of reagent alcohol under constant stirring. An orange precipitate formed that was collected and thoroughly filtered and washed with  $\text{ddH}_2\text{O}$ , and further dissolved in chloroform and filtered again to remove impurities. A Schlenk line was used to thoroughly dessicate the synthesized product. Ten milligrams of  $\text{Sn}(\text{dedc})_4$  powder was dissolved in  $\text{CDCl}_3$ ; the nuclear magnetic resonance (NMR) spectrum that confirms the compounds structure is shown below (Figure 4). 30 mg of  $\text{Sn}(\text{dedc})_4$  powder was also analyzed by thermogravimetric analysis (TGA), confirming the correct decomposition temperature (175 °C) for  $\text{Sn}(\text{dedc})_4$  (Figure 5).

### 2.2.2 Reactor Design

A schematic of the supercritical  $\text{CO}_2$  continuous flow reactor system is shown in Figure 6.

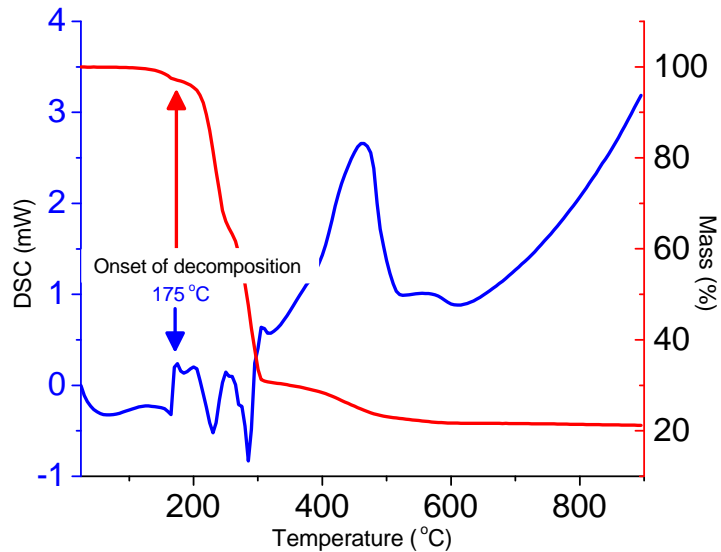


Figure 5: TGA analysis for  $\text{Sn}(\text{dedc})_4$

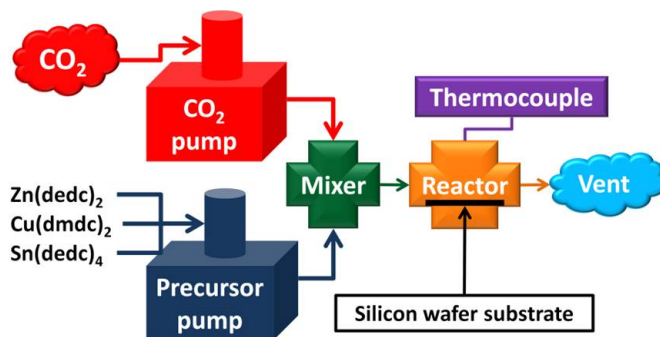


Figure 6: Schematic of supercritical carbon dioxide continuous flow reactor system

### 2.2.3 Deposition Process

A stoichiometric ratio of copper bis(dimethyldithiocarbamate) ( $\text{Cu}(\text{dmdc})_2$ , Aldrich), zinc bis(diethyldithiocarbamate) ( $\text{Zn}(\text{dedc})_2$ , Aldrich), and tin tetra(diethyldithiocarbamate) ( $\text{Sn}(\text{dedc})_4$ , synthesized in-house) were dissolved in 150 mL toluene (99.99%, Aldrich) in a stoichiometric ratio of 2:1:1 for  $\text{Cu}(\text{dmdc})_2 / \text{Zn}(\text{dedc})_2 / \text{Sn}(\text{dedc})_4$ . This corresponds to masses in the ratios 400 mg : 238 mg : 468 mg for  $\text{Cu}(\text{dmdc})_2 / \text{Zn}(\text{dedc})_2 / \text{Sn}(\text{dedc})_4$ . Next, a Teledyne ISCO 500HP pump was filled with the toluene/precursor mixture and pressurized to 124 bar. Similarly,  $\text{CO}_2$  was charged into a Teledyne ISCO 1000D pump and pressurized to 124 bar. Once the steady-state temperature (300 °C) was reached, pure  $\text{CO}_2$  was flowed through the system at a rate of 2 mL  $\text{min}^{-1}$  for 30 min. Next, flow of the toluene/precursor mixture was started at a rate of 1 mL  $\text{min}^{-1}$ . The reaction was run for 2 h, followed by reactor depressurization, cooling, and disassembly to remove the sample from the chamber. Toluene was necessary to achieve sufficient precursor solubility to enable CZTS deposition. However, the toluene could be separated and collected from the carbon dioxide/toluene mix stream by cooling, allowing the toluene to be reused. Furthermore, toluene is a greener and safer choice for a solvent than other methods that have been reported in the literature, such as octadecene and oleylamine [146].

### 2.2.4 Characterization

Scanning electron microscopy images were recorded on a Zeiss Ultra60 SEM at a working distance of 8 mm and accelerating voltage of 10 kV. EDX was conducted on the same Zeiss SEM at an accelerating voltage of 15 kV. The EDX spectrum collected is shown in Figure 7.

X-ray diffraction was conducted with a  $\text{CuK}\alpha$  source at a scan rate of 2°/minute. Raman spectroscopy was carried out on a Nicolet Almega confocal Raman microscope with a 488 nm incident laser and a resolution of 1  $\text{cm}^{-1}$ . UV/Vis spectroscopy was

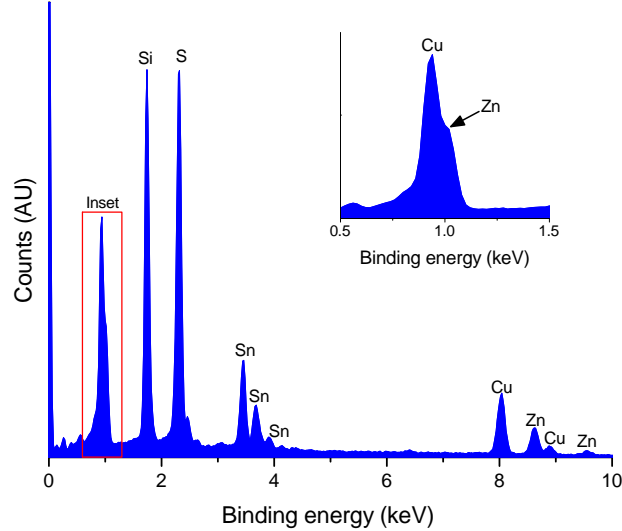


Figure 7: EDX spectrum of CZTS particles on silicon wafer substrate

carried out on an Agilent 8453 UV/Vis spectrophotometer with a resolution of 1 nm. The linear fit of the Tauc plot was carried out on the data in the region from 1.7–2.0 eV.

### 2.3 Results and Discussion

Scanning electron microscopy (SEM) images confirmed the presence of micro- and nanoparticles on the silicon wafer (Figure 8). The particles completely cover the silicon surface and appeared to aggregate, thereby forming a multilayer. At high magnification, particles exhibited a faceted morphology as illustrated in Figure 8c; a cross sectional view is shown in Figure 8d. The particles did not adhere well to the silicon substrate, as they could be removed easily by scratching the surface with a tweezer tip.

Chemical mapping by energy dispersive X-ray spectroscopy (EDX) confirmed the general colocalization and homogeneity of copper, zinc, tin, and sulfur to the observed particles as well as the presence of silicon (from the silicon wafer) in areas where particle density was lower (Figure 9). However, there are patches in the image where

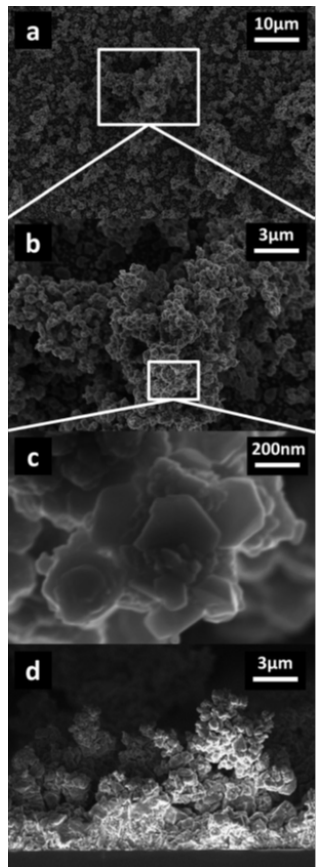


Figure 8: Scanning electron microscope images of CZTS particles formed on a silicon wafer via the sc-CO<sub>2</sub> CFR process. Magnification increases from (a) 2,000×, (b) 5,000×, and (c) 50,000×. White boxes indicate regions viewed at higher magnification in (b) and (c). (d) Cross section image of CZTS on silicon

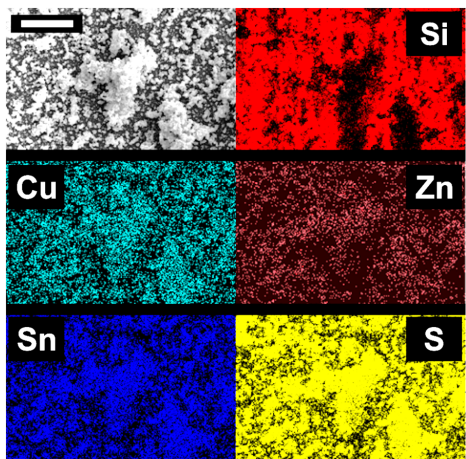


Figure 9: Chemical mapping of CZTS particles on a silicon substrate by energy dispersive X-ray spectroscopy. Scale bar: 15 μm

Table 2: Atomic ratios of  $\text{Cu}_2\text{ZnSnS}_4$  particles as measured by energy dispersive X-ray spectroscopy

Elements	Ideal	Experimental
Cu/Zn	2	2.07
Cu/Sn	2	1.99
Cu/S	0.5	0.542
Zn/Sn	1	0.961
Zn/S	0.25	0.262
Sn/S	0.25	0.273

not all four elements appear. For example, there are regions where Cu, Sn, and S are present, but Zn is absent. This has been reported before, as Zn incorporation is often difficult in CZTS [255].

Quantitative results from EDX illustrated that the stoichiometric ratios between elements were close to the ideal values reported for CZTS (Table 2), although it is possible that the individual particle composition is not necessarily stoichiometric while the overall composition is stoichiometric [114, 146]. Khare et al. observed an excess of sulfur incorporation when using metal dithiocarbamate precursors to form CZTS nanocrystals in octadecene; however, a slight sulfur deficiency was observed here [146]. Yang et al. reported a similar marginal sulfur deficiency when depositing polycrystalline CdS thin films in a continuous-flow sc- $\text{CO}_2$  system due to the higher vapor pressure of S compared to the metal in the supercritical system [321]. The sulfur deficiency observed here is consistent with this explanation.

X-ray diffraction (XRD) analysis established that the sample was crystalline, with diffraction peaks occurring at  $28.7^\circ$ ,  $33.3^\circ$ ,  $47.6^\circ$ , and  $56.6^\circ$  (Figure 10). The observed diffraction pattern has been reported for crystal structures corresponding to both CZTS,  $\text{Cu}_3\text{SnS}_4$ ,  $\text{Cu}_2\text{SnS}_3$ , and ZnS phases [51]. Thus, further confirmation was necessary to determine whether the sample was CZTS or an unwanted phase. Since the crystal lattices of these compounds have different elemental compositions, their

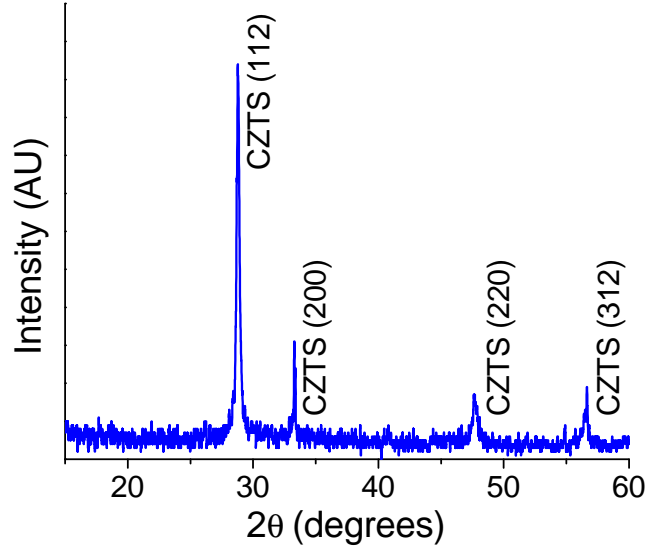


Figure 10: X-ray diffraction pattern for CZTS particles fabricated on silicon via the sc-CO<sub>2</sub> CFR process

phonon normal modes will differ; this difference can be detected using Raman spectroscopy [51]. The most intense Raman peak for the sample was observed at 337 cm<sup>-1</sup> in Figure 11, corresponding to CZTS and indicating that CZTS is the majority phase in the sample [51]. However, the spectra may contain additional peaks of weaker intensity that were not observed, corresponding to ZnS (278 cm<sup>-1</sup>), [15] Cu<sub>3</sub>SnS<sub>4</sub> (318 cm<sup>-1</sup>), and Cu<sub>2</sub>SnS<sub>3</sub> (336 cm<sup>-1</sup>) [91].

The band gap for the deposited sample was estimated by using the Tauc equation:

$$(\alpha h\nu)^n = B(h\nu - E_g) \quad (1)$$

where  $\alpha$  is the absorption coefficient,  $h$  is Planck's constant,  $\nu$  is the frequency of light,  $B$  is a constant of proportionality,  $E_g$  is the band gap energy, and  $n = 2$  for a direct band gap semiconductor such as CZTS [131]. After collecting a UV/Vis spectrum for a dispersion of the CZTS particles dissolved in toluene (Figure 12), the Tauc equation was plotted (inset, Figure 12). Extrapolation of the linear region of the Tauc plot to the abscissa yielded an estimate of the band gap energy, here calculated

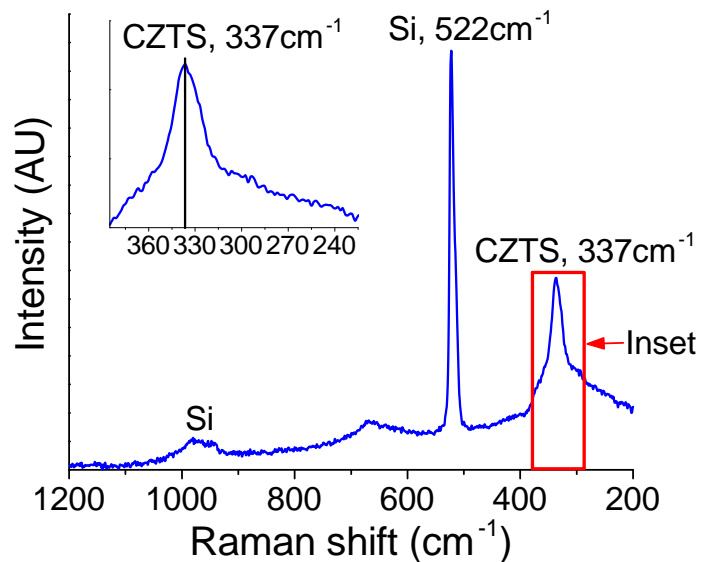


Figure 11: Raman spectrum for CZTS particles deposited on silicon by the sc-CO<sub>2</sub> CFR process. The peak at 337 cm<sup>-1</sup> corresponds to CZTS

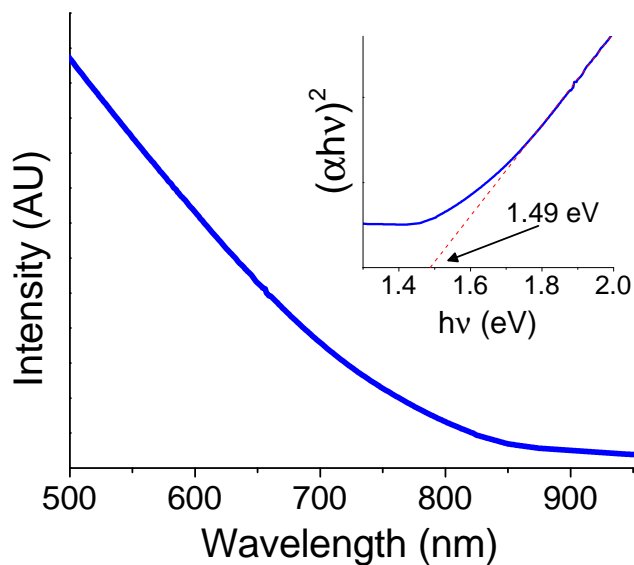


Figure 12: UV/Vis spectrum of CZTS particles. The inset shows the corresponding Tauc plot, and the band gap is estimated where the dashed line intersects the abscissa

to be  $E_g \approx 1.49$  eV (dashed line in inset), which is in agreement with previous reports for direct band gap energies of CZTS thin films and nanoparticles [146].

## ***2.4 Conclusion***

This chapter illustrates the feasibility of synthesizing CZTS particles in a sc-CO<sub>2</sub> process. The deposited particles possessed the characteristic chemical composition, crystal structure, and optical properties that have been previously reported for CZTS.

In the next chapter, the influence of substrate chemistry, reaction time, precursor concentration, and temperature on the deposition of CZTS thin films and particles is described. Each of these variables had a specific effect on the morphology of the fabricated thin films and particles.

## CHAPTER III

# EFFECT OF SUBSTRATE ON $\text{Cu}_2\text{ZnSnS}_4$ MORPHOLOGY IN SUPERCRITICAL CARBON DIOXIDE

### *3.1 Introduction*

Chapter 2 discussed the reasons for synthesizing CZTS in sc- $\text{CO}_2$  and demonstrated the proof-of-concept for using this processing technique to fabricate CZTS. The CZTS particles formed possessed the previously observed composition and crystal structure characteristic of CZTS. In terms of the particle morphology, large agglomerations of CZTS nanoparticles were observed in that work; no film growth was observed. However, it may be desirable to deposit a CZTS film instead of micro- and nanoparticles. It is not clear which processing conditions would control the selective deposition of a CZTS film versus particle formation.

In this chapter, a series of studies were carried out in a batch sc- $\text{CO}_2$  system to determine the effects of substrate, reaction time, precursor concentration, and temperature on the morphology of the synthesized CZTS materials, with the goal of depositing a CZTS thin film. Several substrates were chosen for this study: a gold thin film deposited on Si, a germanium substrate, a molybdenum thin film deposited on Si, and a thermally grown  $\text{SiO}_2$  layer. It was found that the silicon dioxide promoted CZTS film formation, while the Au, Ge, and Mo substrates did not facilitate CZTS film formation, although an oxidized Mo substrate (forming  $\text{MoO}_x$ ) did promote film formation. The processing conditions of reaction time, temperature, and precursor concentration were used to further elucidate the deposition mechanism of CZTS in sc- $\text{CO}_2$ .

## **3.2 Experimental Methods**

### **3.2.1 Substrate choice and preparation**

Germanium wafers with (100) orientation were kindly donated by Professor Michael A. Filler. Gold substrates were kindly prepared by Mr. Tae-Seop Choi by electron beam evaporation, first depositing a 20 nm titanium adhesion layer on a (100) p-type silicon wafer, followed by a  $100 \pm 20$  nm Au layer on the Ti adhesion layer. Thin films of Mo sputter deposited on (100) p-type Si were purchased from LGA Thin Films; the Mo films were of thickness  $100 \pm 20$  nm. Thermally grown  $\text{SiO}_2$  was grown on p-type (100) Si to a thickness of  $300 \pm 50$  nm. The Mo thin films were oxidized in a stream of 50 sccm oxygen at 300 °C to form a  $\text{MoO}_x$  layer.

These substrates were chosen because Ge and Au naturally resist oxide formation, while the thermally grown  $\text{SiO}_2$  oxide is thick and stable [12, 82, 238]. The Mo substrate is the most commonly used substrate for CZTS deposition as it serves as a suitable back contact for device fabrication [5, 248, 297]. Thus, the four substrates selected represent very different surface chemistries in the CZTS deposition process, and it was hypothesized that these surface chemistries would have significant effects on the nucleation and growth processes that lead to potential thin film growth.

All surfaces were cleaned sequentially with methanol, acetone, isopropyl alcohol, and water, and dried under a gentle  $\text{N}_2$  stream, before being loaded into the stainless steel batch reactor. The surfaces were then cleaned *in situ* with hydrogen before initiating the CZTS deposition reaction to remove any residual organic species on the surface.

### **3.2.2 CZTS deposition in sc- $\text{CO}_2$ and characterization**

Stoichiometric ratios of the dithiocarbamate precursors described in Chapter 2 were loaded into the stainless steel batch reactor along with the chosen substrate and 5 mL of toluene as cosolvent. The reactor was pressurized with 400 psi of  $\text{H}_2$  for an *in*

*situ* cleaning step that lasted 10 minutes. The reactor was then heated to the desired temperature and pressurized to 2000 psi with CO<sub>2</sub> and allowed to run for a specified period of time. Samples were characterized using the same SEM, Raman scattering, and XRD techniques detailed in Chapter 2. X-ray photoelectron spectroscopy (XPS) scans were recorded on a Thermo K $\alpha$  XPS system with an Al K $\alpha$  (1486.6 eV) radiation source.

Four conditions were studied for each substrate:

- The base case (300 °C, a ratio of Cu(dmde)<sub>2</sub> : Zn(dedc)<sub>2</sub> : Sn(dedc)<sub>4</sub> of 80 mg: 47.6 mg : 93.8 mg, and one hour reaction time)
- The short time case (same as base case but 1 minute reaction time)
- The low concentration case (same as base case but 5% concentration of precursor of base case)
- The high temperature case (same as base case but run at 400 °C)

### ***3.3 Results and Discussion***

SEM images for deposition of CZTS on oxygen plasma cleaned Si wafer substrates at the base conditions in the batch sc-CO<sub>2</sub> system show that large, agglomerated particles are deposited on the Si wafer surface, as demonstrated in Figure 13a. Moreover, Figure 13b illustrates that no thin film is formed beneath these particles. These results are similar to the CZTS particle morphology found in the continuous flow system observed in Chapter 2.

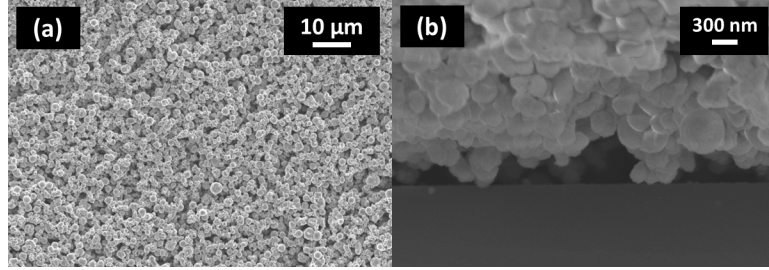


Figure 13: (a) Top-down and (b) cross section view of CZTS particles deposited on oxygen plasma-cleaned Si surface

SEM images for CZTS samples fabricated on Au, Ge, Mo, and SiO<sub>2</sub> surfaces are shown in Figure 14; cross section images for these samples are shown in Figure 15. The cross section images shown in Figure 15 show that CZTS does not form a thin film on Ge or Au substrates; a non-continuous, polycrystalline film with a thickness of about 100 nm is formed on Mo; and a continuous CZTS thin film with a thickness of about 300 nm does form on the SiO<sub>2</sub> substrate.

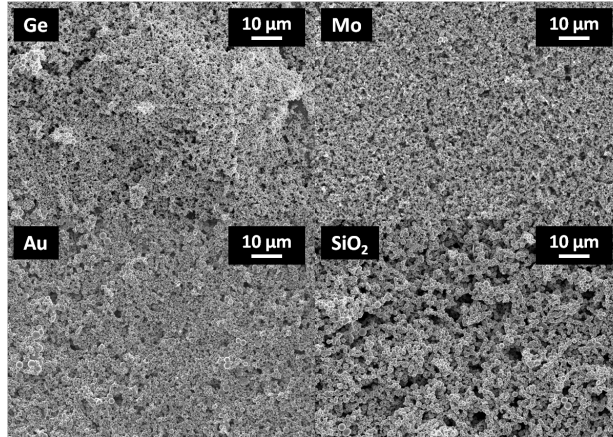


Figure 14: Top-down view of CZTS samples fabricated on Au, Ge, Mo, and SiO<sub>2</sub> substrates

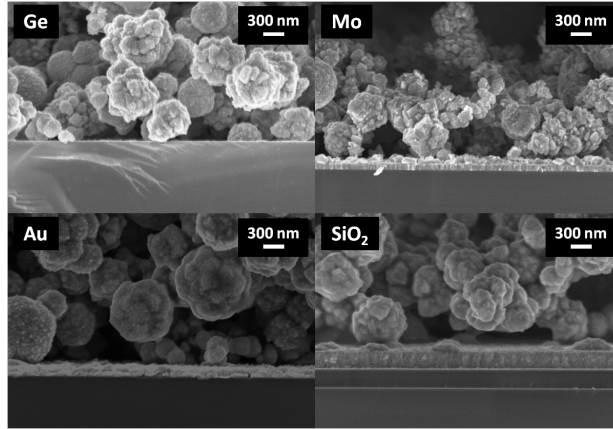


Figure 15: Cross section view of CZTS samples fabricated on Au, Ge, Mo, and SiO<sub>2</sub> substrates

Top-down and cross section SEM images of CZTS samples deposited at 1 minute reaction time are shown in Figures 16 and 17. For the samples deposited at short reaction time (1 minute), large, microscale particles form on the surface of the substrates, although the density of the particles is lower in this case compared to the base case. Figure 17 shows that continuous, uniform thin films again do not form on the Ge, Au, and Mo substrates, but there is CZTS thin film formation on the SiO<sub>2</sub> substrate.

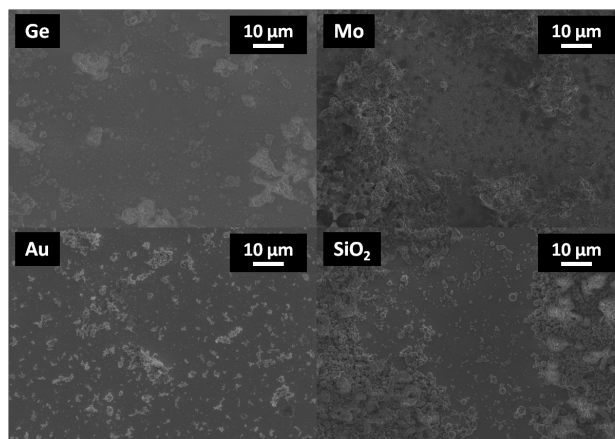


Figure 16: Top-down view of CZTS samples fabricated on Au, Ge, Mo, and SiO<sub>2</sub> substrates at 1 minute reaction time

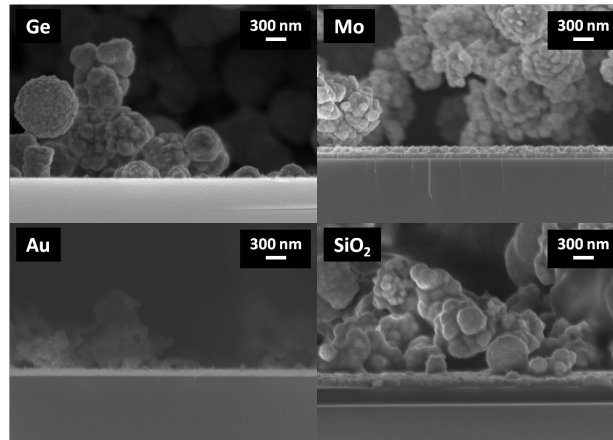


Figure 17: Cross section view of CZTS samples fabricated on Au, Ge, Mo, and SiO<sub>2</sub> substrates at 1 minute reaction time

Top-down and cross section SEM images for CZTS deposition in sc-CO<sub>2</sub> at the low concentration condition are shown in Figures 18 and 19. Films were not observed to form on any of the surfaces at this low concentration condition, and the particle density for particles deposited on the surface was significantly lower than the base case as well.

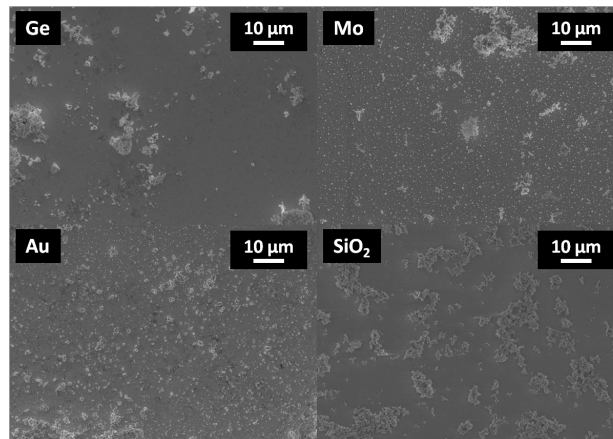


Figure 18: Top-down view of CZTS samples fabricated on Au, Ge, Mo, and SiO<sub>2</sub> substrates at low concentration

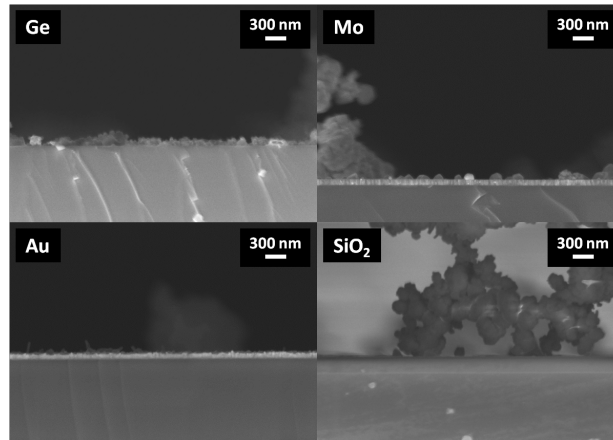


Figure 19: Cross section view of CZTS samples fabricated on Au, Ge, Mo, and SiO<sub>2</sub> substrates at low concentration

Top-down and cross section SEM images for CZTS samples deposited at 400 °C are shown in Figures 20 and 21. Film formation is again poor on the Ge, Au, and Mo substrates; moreover, the thin film formed on the SiO<sub>2</sub> substrate also appears to be less uniform than that in the base case at 300 °C.

Results from XRD and Raman scattering analysis are provided in Appendix A for all samples at all conditions. These results indicate that the samples formed were in fact CZTS.

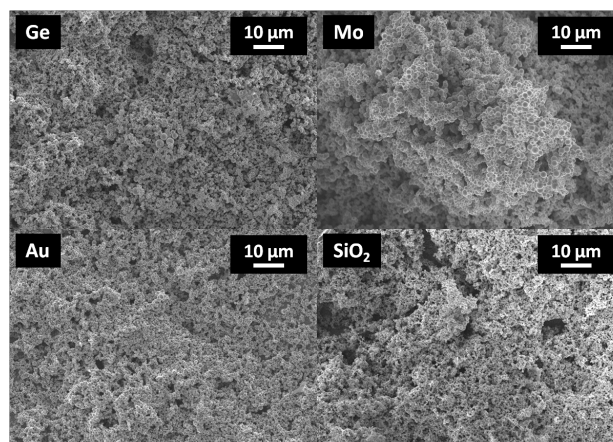


Figure 20: Top-down view of CZTS samples fabricated on Au, Ge, Mo, and SiO<sub>2</sub> substrates at 400 °C

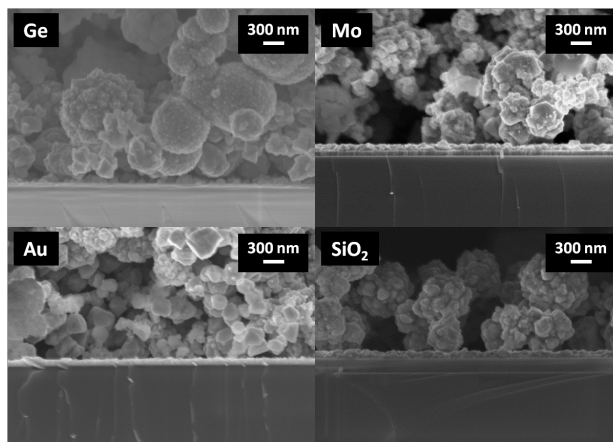


Figure 21: Cross section view of CZTS samples fabricated on Au, Ge, Mo, and SiO<sub>2</sub> substrates at 400 °C

Results from this series of experiments illustrate several points about the deposition mechanism for both CZTS thin film and particle formation. First, from results in the base case described above where a continuous thin film is only formed on the SiO<sub>2</sub> substrate, it appears that the presence of a well-formed, stable oxide layer promotes the formation of the CZTS thin film. Moreover, since the particles formed on all four substrates are similar in size and density, the formation of CZTS particles is insensitive to the surface chemistry and likely occurs in the fluid phase.

Next, data from the 1 minute reaction time condition provide insight into the relative reaction rates of the surface reaction and the fluid phase reaction. At the short reaction time, the thin film still forms on the SiO<sub>2</sub> surface but there is a decreased density of particles compared to the base case. This result implies that the surface reaction initially proceeds more rapidly than the homogeneous (fluid phase) reaction, forming the thin film on the SiO<sub>2</sub> surface, while the CZTS particles form at a slower rate in the fluid phase. Then, these particles that form in the fluid phase deposit on top of the thin film and inhibit the film growth as the reaction proceeds. This inhibition can proceed by two possible mechanisms: the formed CZTS particles may block precursor transport to the thin film, and/or the precursors may react with

the CZTS particles before reaching the developing thin film (this is illustrated in Figure 22). Last, time can potentially be used to selectively form CZTS thin films (at short reaction time) and CZTS particles (at long reaction time).

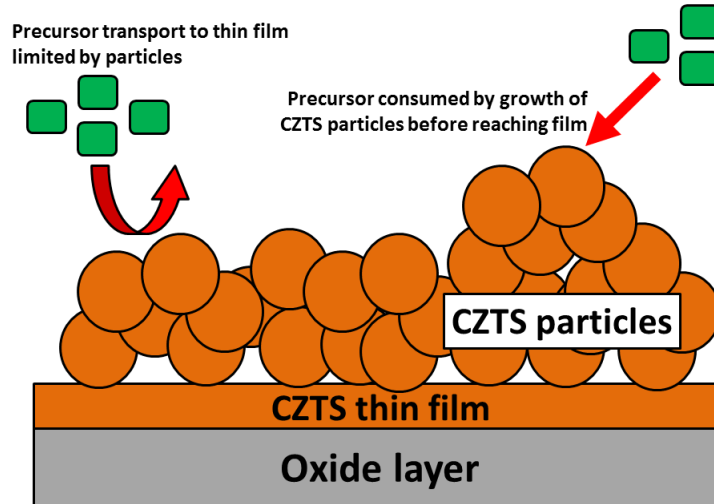


Figure 22: Proposed mechanism for CZTS thin film and particle formation in sc-CO<sub>2</sub>

Results from the low concentration and high temperature conditions also yielded useful information for designing and fabricating CZTS particles and films. At the low concentration condition, the concentration of precursor compounds is too low to promote substantial growth of either a CZTS film or high density CZTS particles (such as those observed in the base case). These data illustrate that concentration can be used to limit both CZTS particle and film formation. At the high temperature condition (400 °C), the thin film formation on SiO<sub>2</sub> was significantly limited compared to the base case while the overall particle density and size was unchanged. It is possible that at the higher temperature, more precursor is consumed in the fluid phase (at a higher reaction rate) and leave less available for the surface reaction to form the thin film. Thus, to selectively form thin films, the reaction should be run at the lowest possible temperature that yields thin film formation.

To test the hypothesis that an oxide layer promotes thin film formation, the Mo

substrate was oxidized at 300 °C in oxygen atmosphere to form an oxide layer on the Mo surface. It was hypothesized that the presence of the oxide layer on the Mo substrate would improve nucleation and growth of CZTS on the surface, leading to an improved, more continuous film forming on the molybdenum oxide compared to the base case. XPS data shown in Figure 23 indicate that the oxidation at high temperature in O<sub>2</sub> atmosphere oxidized the Mo<sup>0</sup> on the surface to MoO<sub>x</sub> [11, 35]. SEM images in Figure 24 show that the MoO<sub>x</sub> layer is on top of the Mo layer and about 15 nm in thickness.

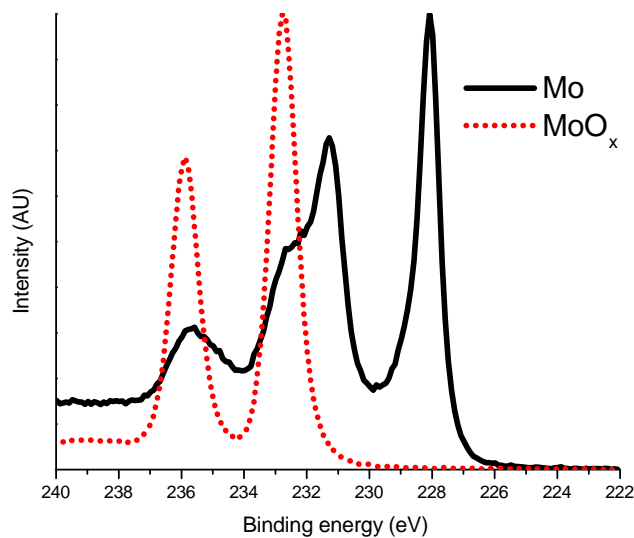


Figure 23: XPS spectra for oxidized and non-oxidized Mo substrate

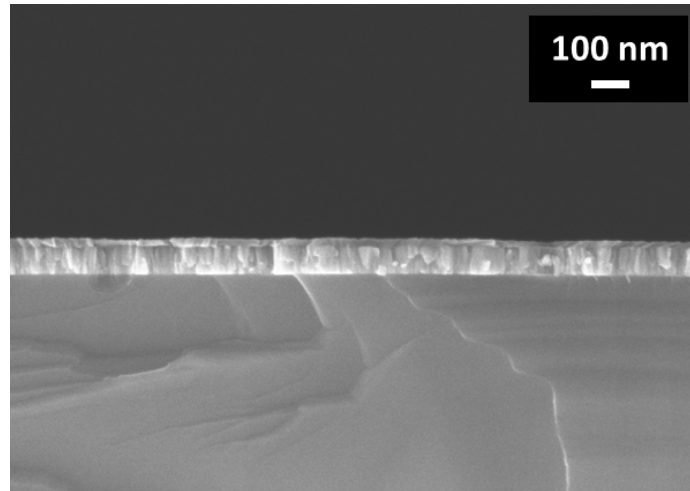


Figure 24: Cross section image of molybdenum oxide layer on Mo substrate

Results from CZTS deposition on the MoO<sub>x</sub> surface show that a continuous CZTS film has formed (Figure 25), in contrast to the semi-continuous, polycrystalline thin film that was formed on the unoxidized Mo substrate in the base case conditions (Figure 15). This result further supports the hypothesis that an oxide layer is vital in promoting CZTS film growth in this sc-CO<sub>2</sub> system. Results from attenuated total reflectance Fourier transform infrared spectroscopy (ATR-FTIR) in the region 3000 – 4000 cm<sup>-1</sup> show an increase in the prevalence of hydroxyl groups on the surface of MoO<sub>x</sub> compared to the Mo substrate (Figure 26) [290]. The hydroxyl groups on the surface are responsible for promoting the adsorption of precursors and/or nucleation of CZTS on the surface in order to form the CZTS thin film, as has been observed in similar sc-CO<sub>2</sub> and CVD systems [179, 323].

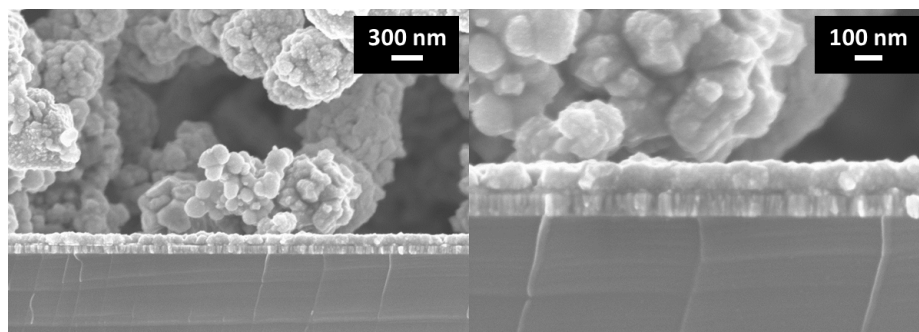


Figure 25: Cross section image of CZTS deposited on MoO<sub>x</sub>

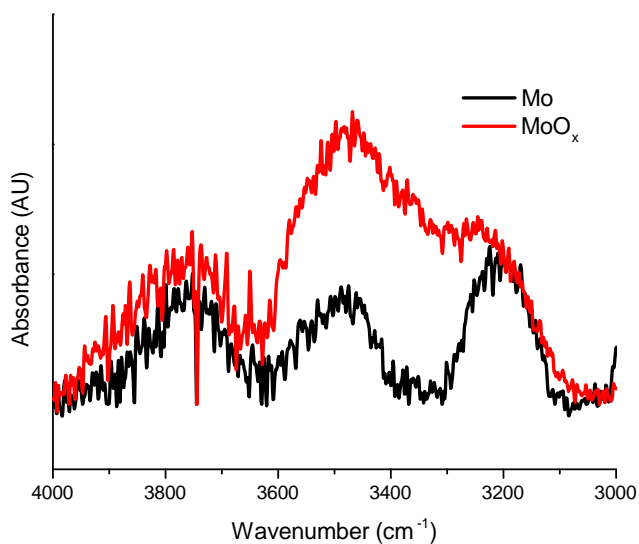


Figure 26: ATR-FTIR spectra of Mo and MoO<sub>x</sub> substrates used for CZTS deposition in sc-CO<sub>2</sub>

### 3.4 Conclusion

This chapter describes how the substrate can influence the deposition and growth of CZTS in a sc-CO<sub>2</sub> process. The presence of an oxide layer was found to promote the growth of CZTS thin films on the surface, while the growth of the large, agglomerated particles was insensitive to the substrate identity. Reaction time and precursor concentration were also shown to be useful process inputs for selectively controlling

the deposition of either CZTS particles or thin films.

In Chapter 4, ZnS nanoparticles are deposited on carbon nanotubes from the zinc diethyldithiocarbamate precursor. This is again a greener synthesis method than the state of the art, and this work on ZnS NP deposition continues the theme of studying the process-structure-property relationships for materials fabricated in supercritical carbon dioxide. The role of surface chemistry on particle nucleation and growth is again observed for depositing ZnS on carbon nanotubes in sc-CO<sub>2</sub>.

## CHAPTER IV

# DEPOSITION OF ZnS NANOPARTICLES ON CARBON NANOTUBES

### *4.1 Introduction*

In the previous chapter, CZTS particles and films were deposited in supercritical carbon dioxide, and the influence of the substrate chemistry on particle and film formation was investigated. In this chapter, zinc sulfide (ZnS) nanoparticles (NPs) were deposited in the sc-CO<sub>2</sub> process as a greener method compared to state of the art techniques used as well as to probe the process-structure-property relationships for this system. Zinc sulfide nanoparticles are useful in many applications due to their optical and electronic properties [156, 262, 292, 334]. ZnS NPs can exhibit phosphorescence and fluorescence depending on their nanostructure and on the presence of metal dopants such as copper and manganese [23, 177]. Carbon nanotubes (CNTs) decorated with ZnS NPs have recently been explored as a novel class of nanocomposites for light emitting diodes, solar cells, photocatalysts, and electroluminescent devices, and several methods have been developed to decorate CNTs with ZnS NPs [90, 147, 257, 304, 329]. The most common techniques are wet-chemical synthesis routes [111]. While these processes are effective in depositing ZnS NPs on CNTs, they also use environmentally unfriendly liquid solvents such as ethylene glycol (a neurotoxin) and sulfur sources such as thioacetamide (a known carcinogen) or hydrogen sulfide (a highly flammable poison) [70, 220, 235, 318, 325, 331].

A less common but more sustainable medium for ZnS NP synthesis is supercritical carbon dioxide (sc-CO<sub>2</sub>), which can replace ethylene glycol as a solvent [92].

Previous reports have described the formation of ZnS NPs using water-in-CO<sub>2</sub> microemulsions as “nanoreactors”, where the ZnS synthesis reaction takes place inside the water core, resulting in NPs with diameters in the range 1–10 nm [207]. However, these efforts do not take full advantage of the transport properties of sc-CO<sub>2</sub> since the ZnS NPs cannot be deposited into high aspect ratio/high tortuosity structures such as CNTs using microemulsions [207]. Furthermore, these techniques use highly specialized, environmentally unfriendly fluorinated surfactants, such as sodium bis(2,2,3,3,4,4,5,5-octafluoro-1-pentyl)-2-sulfosuccinate, to achieve the water-in-CO<sub>2</sub> microemulsion, as well as toxic sulfur sources such as thioacetamide [207]. Using a different approach, Xie et al. deposited ZnS NPs on polymer microspheres from a zinc (II) acetate dihydrate (Zn(Ac)<sub>2</sub>·2H<sub>2</sub>O) precursor, but needed to use thioacetamide as the sulfur source and ethanol as a co-solvent to enhance precursor solubility [315]. Given these previous reports, it is desirable to develop a simpler sc-CO<sub>2</sub> method for ZnS nanocomposite synthesis that avoids the use of environmentally unfriendly surfactants and sulfur sources while allowing deposition of ZnS NPs into high aspect ratio/tortuosity nanostructures such as CNTs. Moreover, to date there has been no significant investigation of the possible deposition mechanisms of ZnS NPs on substrates in the sc-CO<sub>2</sub> system. For example, it is unknown whether the ZnS NPs are synthesized in a homogeneous reaction mechanism in the fluid phase followed by attachment to the substrate or, alternatively, whether the ZnS NPs are synthesized directly on the substrate by a heterogeneous reaction mechanism.

In this chapter, the synthesis of three nanostructures in supercritical carbon dioxide is demonstrated from a single source organometallic precursor, zinc(II) bis(diethyl dithiocarbamate) (Zn(dedc)<sub>2</sub>), via thermal reduction. The three samples fabricated were: ZnS-carbon nanotube nanocomposites (ZnS-CNT); manganese doped ZnS-CNT (Mn:ZnS-CNT); and free ZnS NPs (f-ZnS), which were synthesized in the absence of any substrate. The choice of a single-source precursor eliminated the need

for toxic sulfur sources used in the liquid and sc-CO<sub>2</sub> processes described above, and Zn(dedc)<sub>2</sub> (which thermally decomposes to form ZnS) is significantly less hazardous than these sulfur sources [122, 133]. It should be noted that while this is viewed as a potential improvement over the state of the art in terms of chemicals used in the ZnS NP synthesis, the building block molecules for Zn(dedc)<sub>2</sub>, specifically the dithiocarbamate organic ligands, are likely toxic, although more study of this issue may be necessary [231].

The sc-CO<sub>2</sub> process is greener than liquid processing routes because it replaces environmentally unfriendly solvents with carbon dioxide, providing a use for captured and recycled CO<sub>2</sub>. The method described here also avoids the need for fluorinated surfactants necessary to form a water-in-CO<sub>2</sub> microemulsion, and the transport advantages of the sc-CO<sub>2</sub> technique over previously reported techniques were demonstrated in the deposition of ZnS NPs throughout the CNT matrix. Last, by contrasting the ZnS-CNT and f-ZnS NP samples, it is proposed that a heterogeneous mechanism governs deposition of ZnS NPs onto the CNT substrates.

The synthesized ZnS-CNT formed smaller nanoparticles ( $16.9 \pm 1.9$  nm) that comprise larger nanostructures ( $209 \pm 24$  nm) on the CNTs, while f-ZnS NPs had a mean size of  $178 \pm 15$  nm. The ZnS-CNT nanocomposites were successfully doped with manganese to modify the optical properties of the nanocomposite by inducing emission in the orange region of the spectrum. This doping further demonstrates the applicability of the sc-CO<sub>2</sub> process. Ultraviolet/visible absorption spectroscopy and photoluminescence spectroscopy confirmed the characteristic and desired optical band gap and fluorescence properties of the ZnS-CNT, Mn:ZnS-CNT, and f-ZnS NP products synthesized in the sc-CO<sub>2</sub> process.

## 4.2 *Experimental Methods*

### 4.2.1 **Materials**

Multi-walled, carboxyl-group functionalized carbon nanotubes were purchased from Nano-Lab and used as received; these were selected since it has been speculated that -COOH functionalized CNTs promote nanoparticle nucleation in previous reports [18, 129]. Zinc(II) bis(diethyldithiocarbamate) ( $\text{Zn}(\text{dedc})_2$ , 97%), manganese (III) tris(acetyl acetonate) ( $\text{Mn}(\text{acac})_3$ , technical grade), and methanol (99.99%) were purchased from Sigma-Aldrich. Carbon dioxide (99.99%) was purchased from AirGas.

### 4.2.2 **ZnS nanoparticle deposition and doping in sc-CO<sub>2</sub>**

50 mg of CNT and 100 mg of  $\text{Zn}(\text{dedc})_2$  were loaded into a 30 mL stainless steel hot wall reactor. The reactor was pressurized to 103 bar and heated to 275 °C. This temperature was selected because  $\text{Zn}(\text{dedc})_2$  decomposes to ZnS at 240 °C [146]. Under the experimental conditions, it is unknown what the solubility of the Zn precursor compound is. However, at similar pressures (about 100 bar) and lower temperatures (60°C), previous reports have shown that the solubility of this precursor is on the order of  $10^{-4}$ – $10^{-6}$  mol/L [294]. Thus, at the higher temperature used here, it is likely that the solubility is decreased below these values since solubility in sc-CO<sub>2</sub> decreases with increasing temperature [261, 294].

After two hours, the reaction was terminated by cooling the reactor to room temperature, the system depressurized, and the reactor disassembled to collect and characterize the ZnS-CNT product. The ZnS-CNT nanocomposites were doped with Mn in the same sc-CO<sub>2</sub> system by loading 100 mg of the ZnS-CNT nanocomposite with 10 mg of the  $\text{Mn}(\text{acac})_3$  precursor; the reactor was subsequently pressurized to 103 bar, and heated to 180 °C (above the decomposition temperature of 160 °C). The same method was also used to form f-ZnS NPs except no substrate was added.

The other decomposition products of this reaction are carbon disulfide, diethylamine, ethylisothiocyanate, and ethene [133]. While these are not benign byproducts (and are more toxic than the precursor compound), they are volatile as well as soluble in carbon dioxide and are vented off with the carbon dioxide at the end of the process; thus, humans were not exposed to these chemicals [72, 232]. Furthermore, in an industrial setting, these could be separated from the carbon dioxide and disposed of in an environmentally benign manner.

### 4.2.3 Characterization

Scanning electron microscopy (SEM) was conducted using a Zeiss Ultra60 SEM operated at 5 kV accelerating voltage and 3 mm working distance. Free ZnS NPs were dispersed in methanol, drop cast onto a silicon wafer, and allowed to dry overnight before SEM investigation. Energy dispersive X-ray spectroscopy (EDX) was conducted on the same Zeiss SEM operated at 5 kV accelerating voltage. Transmission electron microscopy (TEM) was conducted using a JEOL 100CX TEM operated at 100 kV accelerating voltage. X-ray diffraction (XRD) was conducted using a PANalytical diffractometer with a  $\text{CuK}\alpha$  source at a scan rate of 2 degrees per minute. Ultraviolet-visible (UV-vis) spectroscopy was conducted using an Agilent 8453 spectrophotometer with a resolution of 1 nm. Photoluminescence spectroscopy (PL) was conducted using a 320 nm light excitation source in a Fluorolog spectrophotometer with a Hamamatsu photomultiplier tube detector. The background spectrum of methanol was subtracted from UV-vis and PL spectra.

## 4.3 *Results and Discussion*

SEM images of ZnS NPs deposited on CNTs are shown in Figure 27a–b. The larger particles appeared to be composed of smaller particles. The average size of the larger particles was determined to be  $209 \pm 24$  nm and the average size of the smaller particles was determined to be  $16.9 \pm 1.9$  nm after measuring 150 nanoparticles of

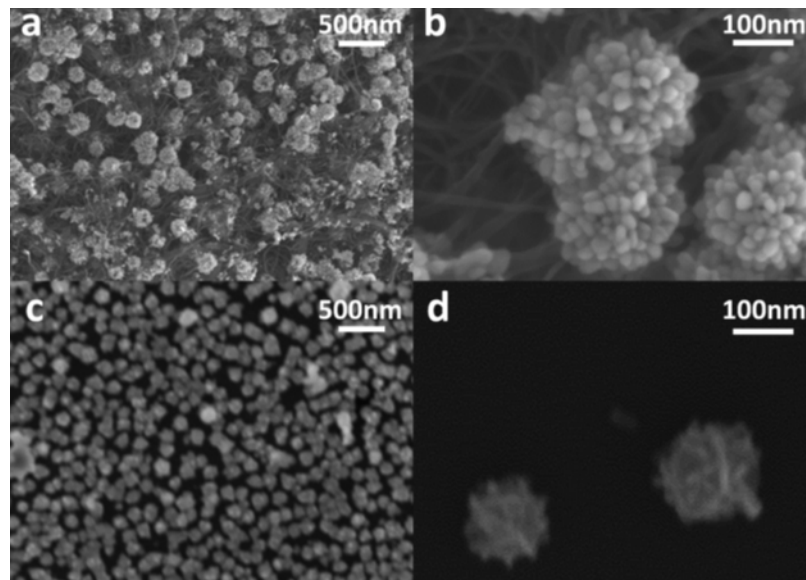


Figure 27: (a)-(b) SEM images of ZnS nanoparticles deposited on carbon nanotubes (c)-(d) SEM image of f-ZnS nanoparticles synthesized in the absence of any substrate

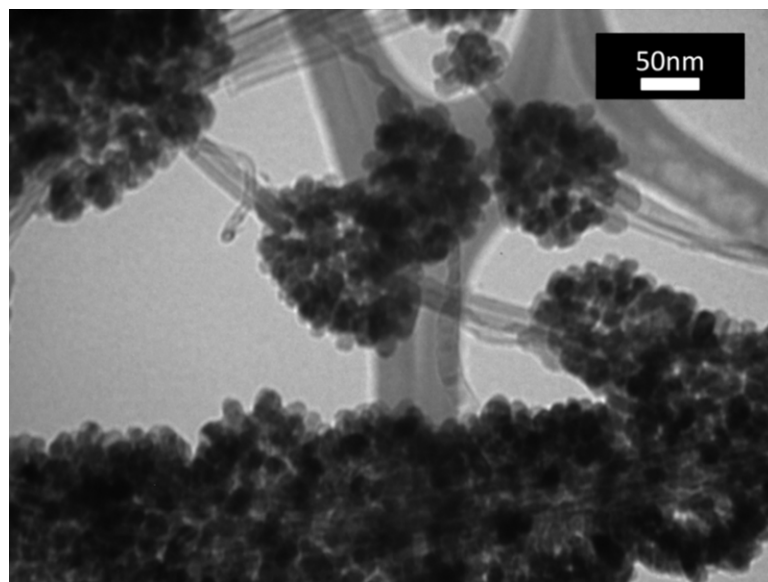


Figure 28: TEM image of ZnS NPs immobilized on CNTs

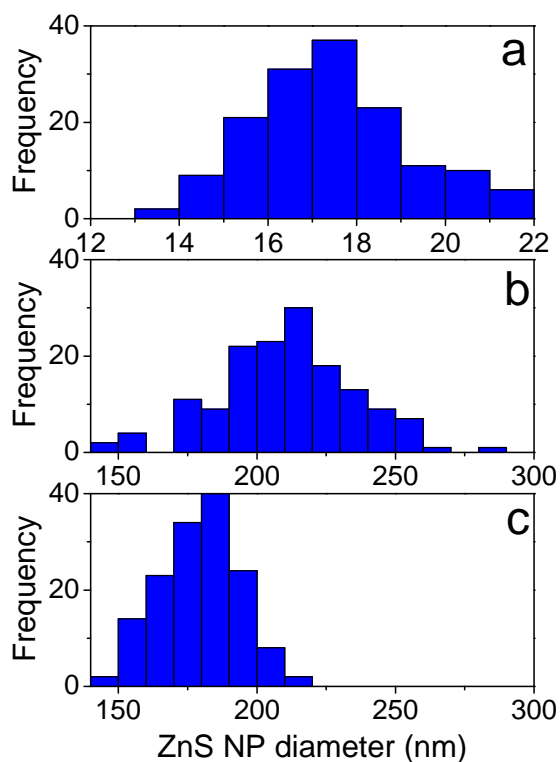


Figure 29: Histograms of (a)  $16.9 \pm 1.9$  nm mean size and (b)  $209 \pm 24$  nm mean size ZnS nanoparticles on CNTs and (c) histogram of  $178 \pm 15$  nm mean size f-ZnS NPs synthesized in the absence of any substrate

Table 3: Atomic composition of ZnS nanocomposites synthesized in  $sc\text{-CO}_2$  as measured by EDX

Element	ZnS-CNT	Mn:ZnS-CNT	f-ZnS
Zn	15.1	14.2	14.9
S	13.9	14	15.3
Mn	0	2.36	0
C	69.3	67.9	4.32
O	1.7	1.54	2.18
Si	0	0	63.3

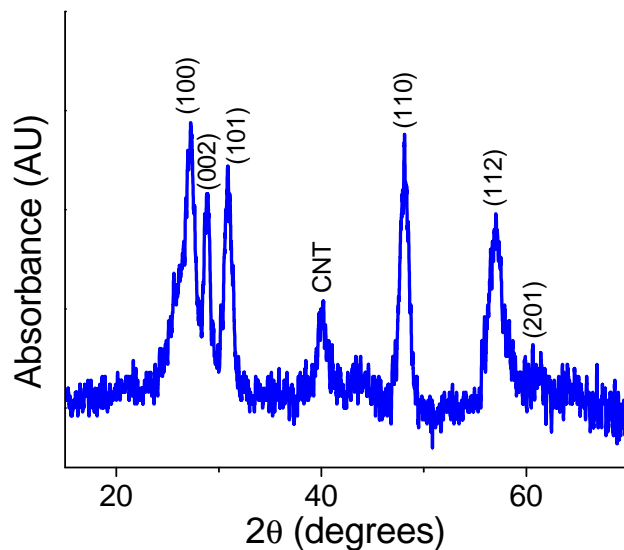


Figure 30: XRD spectrum of ZnS-CNT nanocomposite, illustrating the characteristic peaks for the wurtzite structure of ZnS

each type. Free ZnS NPs synthesized from the  $\text{Zn}(\text{dedc})_2$  precursor in the absence of any substrate are shown in Figure 27c–d. The average size of the particles was  $178 \pm 15$  nm. Results from TEM illustrate that the CNTs were decorated with ZnS NPs (Figure 28). The histograms for each sample calculated from SEM images are shown in Figure 29. The atomic composition of each sample, measured quantitatively by EDX, is shown in Table 3. The EDX spectra corresponding to the ZnS-CNT confirmed the presence of carbon (attributed to the CNTs), oxygen (attributed to carboxyl groups of the CNTs), zinc, and sulfur in the samples. After doping with  $\text{Mn}(\text{acac})_3$  in  $sc\text{-CO}_2$ , manganese was also detected in addition to carbon, oxygen, zinc, and sulfur. Last, the ZnS NPs not attached to a substrate were drop cast on a silicon wafer before EDX analysis, accounting for the high percentage of Si, in addition to some carbon and oxygen contamination that may be present from the organic ligands from  $\text{Zn}(\text{dedc})_2$ .

Figure 30 shows the XRD diffraction pattern for the ZnS-CNT nanocomposite. The characteristic diffraction peaks of wurtzite ZnS occurred at  $27.2^\circ$ ,  $29.0^\circ$ ,  $30.8^\circ$ ,

Table 4: Band gap and peak maxima data from Tauc plot and PL spectroscopy

Sample	$E_g^{Tauc}$ (eV)	$E_g^{PL}$ (eV)	$\lambda_{max}$ from PL (nm)
ZnS-CNT	3.71	2.82	440
Mn:ZnS-CNT	3.69	2.79, 2.07	445, 602
ZnS	3.75	3.56	348

48.1°, 57.1°, and 60.7° [331]. The Scherrer equation estimates crystal size when the crystals are below 100 nm in size:

$$\tau = \frac{0.9\lambda}{\beta \cos\theta} \quad (2)$$

where  $\tau$  is the particle size,  $\lambda$  is the wavelength of X-ray radiation used,  $\beta$  is the full-width at half maximum (FWHM) of the diffraction peak used in the calculation, and  $\theta$  is the diffraction angle of the chosen peak [333]. Using the Scherrer equation with the diffraction peaks that occur at 29.0° and 48.1° (as in previous reports), the crystal sizes were estimated to be 14.4 nm and 14.1 nm, respectively [75]. These values are similar to the mean size of the small nanoparticles ( $16.9 \pm 1.9$  nm) measured in SEM images.

Figure 31 shows the UV-vis spectrum of each sample dispersed in methanol. The peak maximum at 292 nm and band edges present from 300–340 nm correspond to ZnS nanoparticles [329]. The Tauc equation can be used to estimate the optical band gap in a semiconductor material from its UV-vis absorption spectrum:

$$(\alpha h\nu)^n = B(E - E_g^{Tauc}) \quad (3)$$

where  $\alpha$  is the absorption coefficient,  $h$  is Planck's constant,  $\nu$  is the frequency of radiation,  $n = 2$  for a direct band gap semiconductor (such as ZnS),  $B$  is a constant of proportionality,  $E$  is the energy of the electromagnetic radiation (equal to  $h\nu$ ), and  $E_g^{Tauc}$  is the band gap energy measured by the Tauc plot [182]. A plot of  $(\alpha h\nu)^2$  versus  $E$  allows extrapolation of the linear region to the abscissa, which gives an estimate of the band gap for a semiconductor material. Figure 32 shows the Tauc plots for

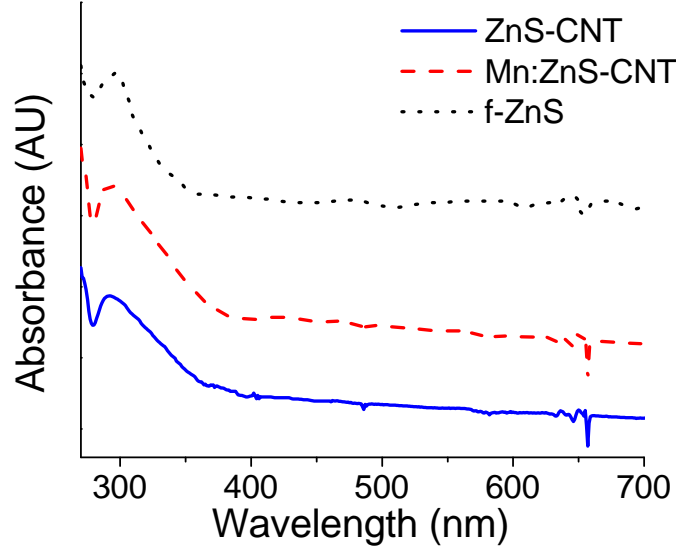


Figure 31: UV-vis absorption spectra of ZnS-CNT and Mn:ZnS-CNT nanocomposites

the absorption band edges observed in the UV-vis spectra, and the extrapolated values for the band gaps for each sample are shown in Table 4. Figure 33 shows the photoluminescence spectra of samples after synthesis in the sc-CO<sub>2</sub> system. The peak maxima in PL spectroscopy ( $\lambda_{max}$ ) are given in Table 4. Values of the band gap energy measured by PL,  $E_g^{PL}$ , were calculated using the Planck-Einstein equation:

$$E_g^{PL} = \frac{1240eV \cdot nm}{\lambda_{max}} \quad (4)$$

and are also shown in Table 4 [12].

#### 4.3.1 Nanoparticle size and morphology

Carbon nanotubes were successfully coated with ZnS NPs using the sc-CO<sub>2</sub> deposition method as illustrated by SEM images in Figure 27a and 1b. The ZnS-CNT possessed a structure in which smaller, discrete NPs were tightly packed to form larger NP structures, while the f-ZnS NPs synthesized in the absence of a substrate did not possess this hierarchical NP structure (Figure 27). These results lead to the hypothesis that in the absence of a substrate the f-ZnS NPs followed a traditional

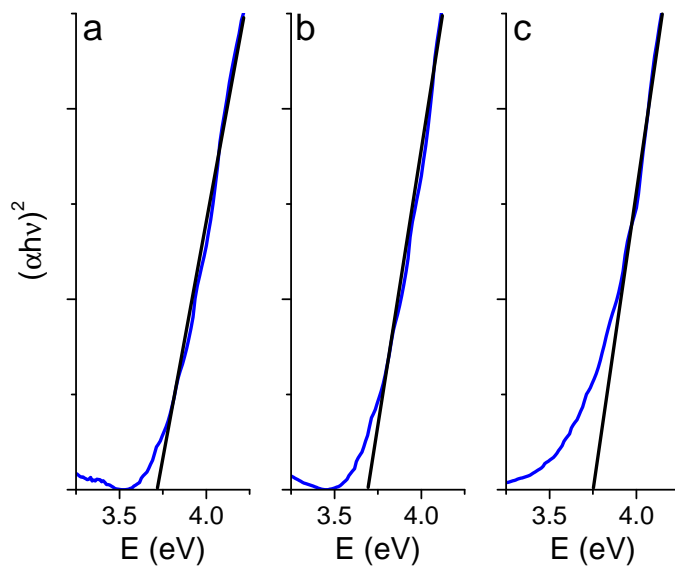


Figure 32: Tauc plots corresponding to UV-vis spectra of (a) ZnS, (b) Mn:ZnS-CNT, and (c) f-ZnS in Figure 31

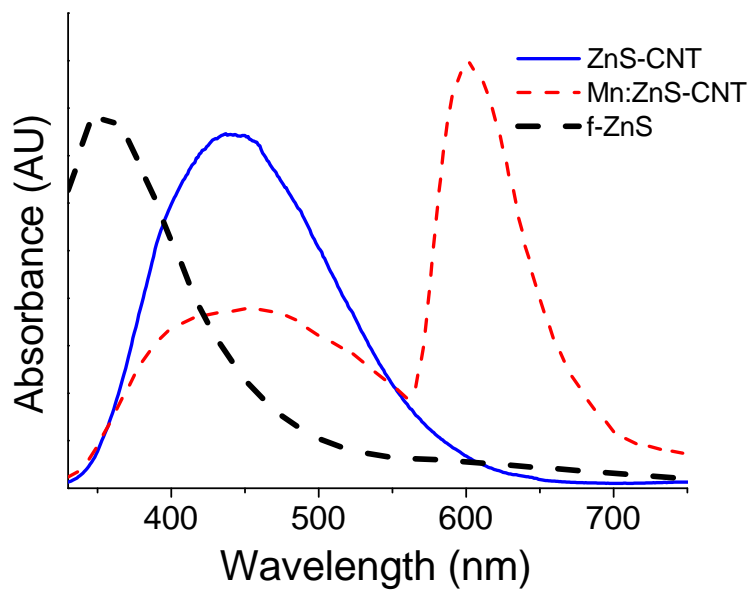


Figure 33: Photoluminescence spectra of ZnS-CNT and Mn:ZnS-CNT nanocomposites

homogeneous nucleation and growth mechanism in the fluid sc-CO<sub>2</sub> phase, similar to homogeneous nucleation and growth that has been previously reported for ZnS NP synthesis in aqueous solution [201, 330]. However, when ZnS NPs formed in the presence of the CNT, the activation energy for nucleation on the CNT surface was lower than the activation energy for homogeneous nucleation, heterogeneous nucleation occurred on the CNTs, which dominated over homogeneous nucleation in the sc-CO<sub>2</sub> phase. Thus, the initial nucleation mechanism is homogeneous in the absence of CNTs and heterogeneous in the presence of CNTs. After ZnS NPs have nucleated in either scenario (homogeneous or heterogeneous), the activation energy for nucleation and growth is even lower, possibly due to an autocatalytic mechanism where ZnS NPs facilitate the reaction of Zn(dedc)<sub>2</sub>, resulting in continued nucleation and growth by the favored mechanism. Moreover, the NPs did not deposit evenly along the entire length of the CNTs but rather clustered together in somewhat irregular shapes, in contrast to previous reports where spherical metal NPs (such as Pt) were deposited evenly along CNTs using sc-CO<sub>2</sub> [18, 129]. Such observations suggest that after ZnS NP had formed on the CNT walls, the Zn(dedc)<sub>2</sub> precursor favored heterogeneous adsorption and reaction on already formed ZnS NP sites over reaction on the CNT walls, further supporting the hypothesis of a heterogeneous reaction mechanism for ZnS NPs deposited on CNTs.

Previous attempts to decorate ZnS NPs on CNTs have focused on synthesizing much smaller NPs (1–10 nm in diameter) for specific applications [207, 329]. For example, 1–10 nm NPs are more desirable for photocatalysis (by increasing the surface area/volume ratio and decreasing costs) or tuning the band gap of ZnS through quantum confinement effects [23, 127, 165]. Thus, depending on the application, a potential drawback of the method established here is the relatively large size ZnS NPs deposited on the CNTs, and future studies of this system will focus on controlling ZnS

NP size and homogeneity on the CNT surface by modifying the CNT surface chemistry and reaction conditions. Nonetheless, the size distributions and nanoparticle structures observed were sufficient to yield fluorescent ZnS-CNT and Mn:ZnS-CNT nanocomposites with desirable optical properties (see next section).

The Mn:ZnS-CNT sample showed the same morphology and size distribution as the ZnS-CNT sample; this was expected since the doped Mn:ZnS-CNT sample was formed from a portion of the ZnS-CNT, and the Mn composition was small (2.36 atomic %). Also, the crystal structure of the Mn:ZnS-CNT and f-ZnS samples were the same as that of the ZnS-CNT sample. The percent yield of the ZnS-CNT deposition reaction was 64.6%, the percent yield from the Mn doping on ZnS-CNT was 55.4%, and the percent yield of the f-ZnS synthesis reaction was 60.2%. These poor yields are accounted for by precursor reaction with the reactor side walls (since it is a hot wall reactor) as well as dissolved precursor that had not yet decomposed when CO<sub>2</sub> was vented.

### 4.3.2 Optical properties

The optical band gap of each sample was studied using UV-vis absorption spectroscopy. The observed optical band gaps measured by UV-vis and a Tauc plot ( $E_g^{Tauc}$ ) of 3.71 eV, 3.69 eV, and 3.75 eV (Table 4) were in agreement with reported values for the band gap of ZnS, which is 3.70 eV [164]. The band gaps for the ZnS-CNT and Mn:ZnS-CNT samples were nearly identical to the band gap for the f-ZnS and ZnS because Mn doping and adherence to the CNT substrate does not affect the energy levels of the valence band (VB) or conduction band (CB) of ZnS, which determine the size of the optical band gap [244]. It should also be noted that none of the ZnS NPs were small enough to exhibit quantum confinement effects, which have been shown to significantly increase the band gap energy for ZnS NPs smaller than 5 nm [320].

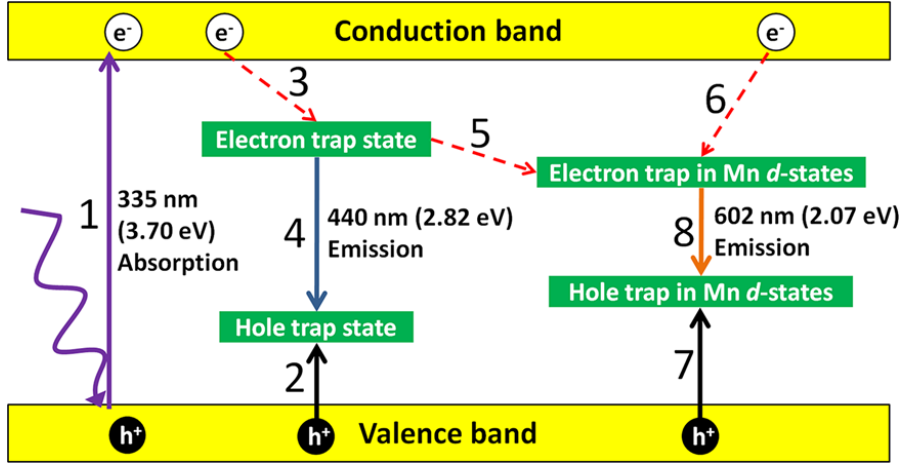


Figure 34: Energy level diagrams for the ZnS-CNT and Mn:ZnS-CNT nanocomposites synthesized in sc-CO<sub>2</sub> (1) Photon absorption and exciton generation (2) Hole promotion to a hole trap state (3) Nonradiative decay into electron trap state (4) Blue light emission as an electron recombines with a hole (5) Nonradiative decay to a Mn *d*-state (6) Nonradiative decay to a Mn *d*-state (7) Hole promotion into a Mn *d*-state (8) Orange light emission as an electron recombines with a hole

Results from photoluminescence spectroscopy demonstrated the fluorescent emission of each sample synthesized in sc-CO<sub>2</sub> upon illumination with 320 nm UV light. However, data from PL spectroscopy yielded  $E_g^{PL}$  values significantly smaller than those measured by  $E_g^{Tauc}$ . Furthermore, the  $E_g^{PL}$  values for each sample differed. The differences in band gap energies between samples and between characterization techniques can be explained by considering the mechanisms of electron excitation and photon emission in ZnS, which have been detailed extensively elsewhere [75, 244]. For completeness, the energy level diagram in Figure 34 outlines these mechanisms, provides a framework for understanding the results, and is briefly summarized here.

Radiation is absorbed to generate an electron-hole pair (exciton) in the VB and CB (Step 1 in Figure 34). This absorption process is observed in UV-vis spectroscopy and leads to the  $E_g^{Tauc}$  values reported in Table 3; moreover, this excitation event is not influenced by the presence of CNTs, Mn, or any other defects in the nanocomposite or NPs. In a band gap emission event, electrons should decay from the conduction band to the valence band, emitting 335 nm (3.7 eV) photons. However, no band gap

emission is observed here, likely due to the presence of defects that introduce usually forbidden energy levels into the band gap that can trap electrons and holes. These energy levels are known as electron or hole trap states and do not exist in defect-free ZnS. For example, electrons from CNTs (from orbitals of the CNTs or O<sup>-</sup> species of carboxyl groups on the CNT walls) can be donated to photogenerated holes in the VB, resulting in hole promotion to hole trap states at higher energy levels than the valence band (Step 2 in Figure 34).

Concurrently, defects in the ZnS crystal lattice increase the likelihood of nonradiative decay processes (i.e., phonon excitation) compared to defect-free ZnS. Such defects include surface effects (i.e., dangling bonds) or physical deformations in the ZnS crystal structure induced by the CNTs. Nonradiative decay events allow electrons to fall from the conduction band to shallow electron trap states (Step 3 in Figure 34). The relaxed electron in a shallow trap state then decays into a hole trap state; this recombination releases a photon with  $E_g^{PL} = 2.82$  eV (Step 4 in Figure 34), which is significantly lower than  $E_g^{Tauc} = 3.71$  eV for the ZnS-CNT sample. The 440 nm ( $E_g^{PL} = 2.82$  eV) peak observed here is also significantly broader than would be attributed to a single electronic transition. This broadening may be due to different defects (such as the number of substitutions or interstitial sites) occurring in different ZnS NPs on the CNTs. These impurity differences may give rise to slightly different energy levels for the electron and hole trap states in the band gap, ultimately leading to transitions that occur at marginally different energies (and hence wavelengths), contributing to the broadness of the peak.

PL spectroscopy of the Mn:ZnS-CNT sample exhibited an orange emission peak at 602 nm ( $E_g^{PL} = 2.07$  eV) in addition to the blue emission peak at 445 nm ( $E_g^{PL} = 2.79$  eV). These peaks are in agreement with previous reports for Mn:ZnS-CNT nanocomposites where the *d* orbitals of Mn introduce usually forbidden energy levels in the ZnS band gap. The mechanism for emission of the broadband blue light is

attributed to the same mechanism described for the ZnS-CNT sample in steps 1–4 in Figure 34. The emission peak at 602 nm ( $E_g^{PL} = 2.07$  eV) is attributed to the presence of Mn doping impurities present on the surface of the ZnS nanoparticles, which introduce empty  $d$  orbitals of the Mn atoms into the spacing between the valence and conduction bands of ZnS. These unoccupied  $d$ -states can accept electrons from shallow trap states (Step 5 in Figure 34) or from the conduction band (Step 6 in Figure 34) via nonradiative decay while the electron occupied  $d$  orbitals can donate electrons to the VB, resulting in promoted holes at higher energy levels with reference to the VB (Step 7 in Figure 34). Emission of orange 602 nm ( $E_g^{PL} = 2.07$  eV) light occurs when an electron falls from a shallow trap state to a trapped hole state (Step 8 in Figure 34). The broadness of the peak is attributed to the same mechanism described for the ZnS-CNT nanocomposite. The intensity of the 602 nm ( $E_g^{PL} = 2.07$  eV) peak is significantly higher than that of the 445 nm ( $E_g^{PL} = 2.79$  eV) peak in the Mn:ZnS-CNT sample, indicating that decay events resulting in orange light emission occur more frequently than those resulting in blue light emission, an observation that has been previously reported [244].

The f-ZnS NPs not formed on a substrate displayed an emission peak at 348 nm ( $E_g^{PL} = 3.56$  eV). Defect-free ZnS NPs would have shown an optical band gap emission peak at 335 nm (3.7 eV) as discussed above. Thus, it is likely there is some sample contamination present (for example, carbon or oxygen arising from the organic ligands of  $\text{Zn}(\text{dedc})_2$  as was detected in EDX) that introduced forbidden energy levels into the band gap of the f-ZnS NPs. However, compared to the ZnS-CNT and Mn:ZnS-CNT spectra, the  $E_g^{PL}$  for the f-ZnS NPs are closest to the optical band gap energy for defect free ZnS NPs, indicating that the f-ZnS NPs have relatively fewer defects than ZnS-CNTs or Mn:ZnS-CNTs, as expected. Furthermore, comparing  $E_g^{PL}$  for the three samples, it is clear that the CNT substrate and Mn doping significantly red-shifted the  $\lambda_{max}$  of the nanocomposites through the introduction of additional

defects into the ZnS compared to the f-ZnS NPs.

#### **4.4 Conclusion**

In this chapter, zinc sulfide nanoparticles were deposited on carbon nanotubes using a one-step batch supercritical carbon dioxide process with the single source precursor zinc(II) bis(diethylthiocarbamate). Comparing the deposition of ZnS NPs on CNTs versus ZnS NP synthesis in the absence of any substrate supports the hypothesis that ZnS NP decoration on CNTs proceeds by a heterogeneous reaction mechanism. The ZnS-CNT nanocomposite was then doped using manganese(III) tris(acetylacetonate) in sc-CO<sub>2</sub>. This represents a greener, more environmentally friendly process for decorating CNTs with ZnS NPs and doping ZnS compared to current methods and also leverages the advantages of sc-CO<sub>2</sub> for nanoparticle deposition. The ZnS nanoparticles possessed two characteristic sizes: smaller particles ( $16.9 \pm 1.9$  nm) that agglomerated to form larger particles ( $209 \pm 24$  nm), while ZnS NPs synthesized in the absence of any substrate had a mean size of  $178 \pm 15$  nm. The differences between the ZnS-CNT and f-ZnS NPs suggested a difference in the reaction mechanism (heterogeneous versus homogeneous) between the two samples. Red shifting and broadening of the fluorescent peaks of the nanocomposites were attributed to defects in the ZnS crystal structure, resulting in usually forbidden energy levels being introduced into the band gap. Future efforts will be dedicated to decreasing the ZnS NP size and increasing ZnS NP homogeneity on the CNT surface.

The work developed in this chapter extends the motif of the important relationship between surface chemistry and the nucleation and growth phenomena first observed in Chapter 3. The carboxyl groups present on the CNT surface played a similar role in promoting ZnS particle nucleation and growth that hydroxyl groups did in promoting these processes for CZTS deposition.

In the next chapter, silver nanoparticles are deposited on silicon and glass substrates, and the influence of surface pretreatment, surface chemistry, and temperature on silver nanoparticle size and density are investigated. The silver nanoparticles were applied in surface enhanced Raman spectroscopy. These studies continue the theme of understanding the process-structure-property relationships for nanomaterials fabricated in supercritical carbon dioxide.

## CHAPTER V

# CONTROLLING DEPOSITION OF SILVER NANOPARTICLES IN SUPERCRITICAL CARBON DIOXIDE

### *5.1 Introduction*

In the previous chapter, ZnS nanoparticles were deposited on carbon nanotubes for photoluminescent application. In this present chapter, silver nanoparticles are deposited on silicon and glass surfaces using sc-CO<sub>2</sub> for application in surface enhanced Raman spectroscopy (SERS).

Several methods have been explored to fabricate surface enhanced Raman spectroscopy active surfaces for trace concentration analyte detection. Nanosphere lithography (NSL) can fabricate large arrays of nanostructures that can be used in SERS [134]. In this technique, a monolayer of polystyrene nanospheres is spin-coated on top of the surface, usually silicon or glass. A metal thin film is then deposited by vapor deposition in the regions between spheres and annealed at 300 °C – 500 °C; the spheres are then removed by dissolution in a solvent. While the reproducibility of this technique is excellent, it requires high vacuum conditions as well as high temperature annealing and uses environmentally unfriendly chemicals such as polystyrene, which cannot be recycled and require hundreds of years to biodegrade.

Two other methods used to make SERS active surfaces are glancing angle deposition (GLAD) and electron beam lithography (EBL). In GLAD, metal nanostructures are deposited on a substrate by sputtering from a source positioned at about 85 degrees from the substrate normal [170]. This technique can effectively create multiple

types of nanostructures, such as arrays of nanorods that could detect the model analyte Rhodamine 6G (R6G) at a concentration of  $10^{-12}$  M [332]. However, it is difficult to achieve reproducibility and uniformity in this system. In EBL, small nanostructures can be patterned with precision and repeatability by the highly focused electron beam [142]. However, the EBL process requires a large capital investment, high vacuum conditions, does not scale easily to larger substrates, and has low throughput.

One relatively unexplored method for making SERS active surfaces is the use of supercritical carbon dioxide (sc-CO<sub>2</sub>) for the direct deposition of nanoparticles from an organometallic precursor on a substrate. Supercritical carbon dioxide possesses several advantages over other methods such as NSL, GLAD, and EBL. The synthesis of nanoparticles on surfaces via sc-CO<sub>2</sub> can be performed in a single reactor, is rapid (2 h or less), and can be used with a wide variety of substrates. Furthermore, sc-CO<sub>2</sub> possesses high diffusivity, low viscosity, and no surface tension, enabling rapid transport of the organometallic precursor to the substrate surface [261]. Last, the sc-CO<sub>2</sub> technique offers a method to recycle captured carbon dioxide and does not generate CO<sub>2</sub> in the nanoparticle deposition process, making it more environmentally friendly than the techniques described above because it provides a use for captured CO<sub>2</sub>.

Supercritical CO<sub>2</sub> has been used previously to deposit noble metal nanoparticles and metal thin films on several substrates for applications in catalysis, fuel cells, and microelectronics; however, SERS applications have not been extensively pursued [39, 168, 180, 242, 323]. The only previous report that invoked sc-CO<sub>2</sub> to fabricate SERS active surfaces impregnated the organometallic precursor silver(I) hexafluoroacetylacetonate cyclooctadiene (Ag(hfac)(COD)) into a polycarbonate matrix [118]. This step was followed by reduction in hydrogen atmosphere to synthesize silver nanoparticles (AgNPs) inside the matrix. Hasell et al. reported a sensitivity of 2 mM for the surface detection of R6G on the surface of the polycarbonate matrix. A

nanoparticle size of 2–10nm was reported, but no attempt was made to use process conditions to control the particle size; however, the penetration depth of AgNPs into the matrix could be extended by increasing the duration of the impregnation step of their process.

Since the size, density, and shape of AgNPs ultimately influence the SERS efficiency of a surface, it is important to understand how process conditions in the sc-CO<sub>2</sub> deposition process, such as temperature or surface chemistry, affect the nucleation, growth, and diffusion processes that might be occurring in this reaction system [142, 264, 278]. Previous work has addressed these mechanistic considerations for homogeneous nanoparticle synthesis in the fluid phase for supercritical water and CO<sub>2</sub> systems [1, 206, 211]. However, there remains a paucity of knowledge regarding how experimental parameters affect processes occurring in the sc-CO<sub>2</sub> system for heterogeneous nanoparticle deposition on substrates. Thus, investigation is necessary to establish and understand the mechanisms that govern nanoparticle deposition on surfaces in the sc-CO<sub>2</sub> system. By understanding these fundamental processes, it will be possible to manipulate experimental parameters to rationally design and control nanoparticle properties in order to optimize the performance of a desired product.

The contributions of the present work address these issues. First, heterogeneous AgNP deposition on oxygen plasma treated silicon, oxygen plasma treated glass, and HCl treated silicon surfaces was demonstrated to be temperature controlled, suggesting that the process is limited by kinetics rather than transport of precursor to the substrate in the sc-CO<sub>2</sub> system. Second, temperature and surface chemistry were shown to have significant effects on mean AgNP size, density, and surface coverage in the sc-CO<sub>2</sub> deposition system, providing two experimental parameters that can be used to rationally manipulate AgNP properties for SERS applications. Last, the SERS substrates fabricated by the sc-CO<sub>2</sub> method in this work exhibit three orders of magnitude improved sensitivity compared to previous reports using sc-CO<sub>2</sub> for SERS

surface fabrication in that a target analyte was detected at 1  $\mu$ M concentration in the present study. The sc-CO<sub>2</sub> system used here represents a potentially greener method for fabricating SERS active surfaces compared to the current state of the art.

## **5.2 *Experimental Methods***

### **5.2.1 Materials**

Carbon dioxide gas (99.99%) and hydrogen gas (99.99%) were purchased from Air-gas. The organometallic precursor silver hexafluoroacetylacetonate cyclooctadiene (Ag(hfac)(COD)), methanol, acetone, isopropyl alcohol, solid Rhodamine 6G (R6G), and concentrated hydrochloric acid (HCl, 12 M) were purchased from Sigma Aldrich and used as received. Test silicon wafers (*p*-type, 10–20  $\Omega$ ·cm, (100)) were purchased from University Wafer. Soda lime glass slides were purchased from Fisher Scientific.

### **5.2.2 Surface pretreatment**

The substrates were cut into 2 cm x 3 cm pieces and rinsed with methanol, acetone, and isopropyl alcohol sequentially, then dried under a gentle stream of N<sub>2</sub>. Test silicon wafer and glass substrates were pretreated by two methods. In the first method, substrates were subjected to 10 minutes of cleaning in an oxygen plasma in a Harrick PDC-32G Plasma Cleaner, and these surfaces are hereafter referred to as “plasma treated.” In the second method, surfaces were subjected to a 30 minute wash in a 12 M solution of HCl. Substrates were then washed thoroughly with deionized water and dried under a gentle N<sub>2</sub> stream, and are hereafter referred to as “HCl treated” surfaces. Plasma and acid treatments were chosen because they are simple, frequently used, and their effects on surface chemistry are well characterized [236].

### **5.2.3 Nanoparticle deposition**

In order to deposit AgNPs on the substrates under study, 50  $\pm$  0.1 mg of the Ag(hfac)(COD) precursor was loaded into a 30 mL hot wall stainless steel reactor along with

the desired substrate. The reactor was initially pressurized by  $400 \pm 10$ psi of hydrogen, then brought to  $1500 \pm 10$ psi pressure by introduction of carbon dioxide by a Teledyne ISCO 500HP pump; the reactor configuration has been previously described [161]. During pressurization, the reactor was simultaneously heated to 60 °C, 120 °C, or 180 °C ( $\pm 5$  °C) by a hot plate. These temperatures were chosen based on previous reports that demonstrate AgNP synthesis in the range from 60 °C to 180 °C [53, 135, 322]. Temperature and pressure were monitored by a thermocouple inserted into the center of the reactor and a pressure transducer, respectively. The reaction was allowed to run for two hours, followed by depressurization over a 10 minute period and removal of the products.

#### 5.2.4 Characterization

Scanning electron microscope (SEM) images were recorded using a Zeiss Ultra60 SEM operated at 5 kV accelerating voltage and 3 mm working distance. Image analysis of SEM images was carried out using the Image Analysis toolbox in MATLAB in order to eliminate experimenter bias. Using the *regionprops* function, it is possible to measure the area of each AgNP; assuming a spherical particle, the diameter of the AgNP can be determined. Nanoparticle density was calculated by dividing the number of particles observed by the total area sampled; interparticle distance was established by determining the particle density, taking the reciprocal of this value, and calculating the square root. The area covered by AgNPs was estimated by dividing the area of all of the AgNPs by the total area sampled. Transmission electron microscopy (TEM) images were recorded using a JEOL 100CX-2 TEM operated at 100kV accelerating voltage in both imaging and diffraction modes.

SERS spectra were collected using a Nicolet Almega Raman microscope with a laser wavelength of 785 nm and power of 2 mW launched by a 50 $\times$  objective lens. The spot size was about 1  $\mu$ m, the resolution of the detector was 4  $\text{cm}^{-1}$ ,

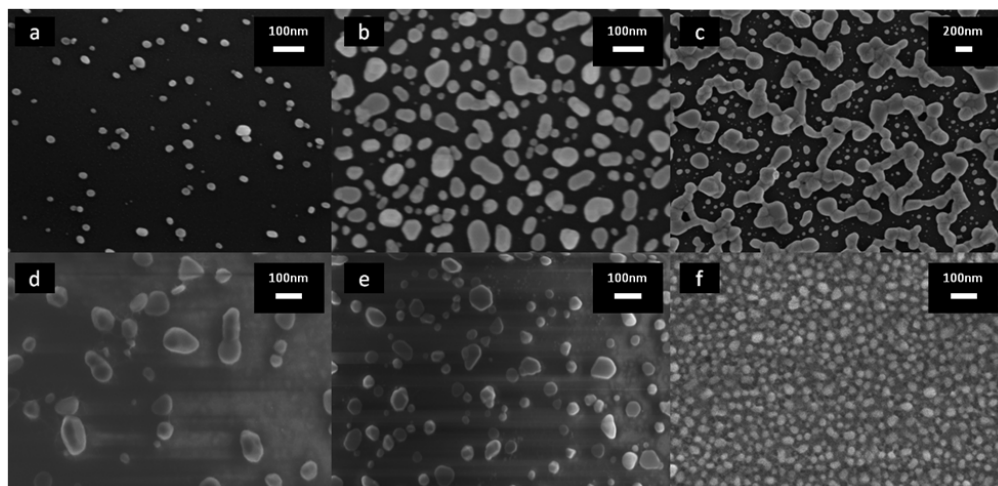


Figure 35: SEM images of AgNPs deposited on plasma treated silicon at (a) 60 °C, (b) 120 °C, and (c) 180 °C and plasma treated glass at (d) 60 °C, (e) 120 °C, and (f) 180 °C

and for each sample a single scan was conducted with an acquisition time of 10 s. Before collecting SERS spectra, AgNP coated substrates were submerged in a 1  $\mu$ M solution of R6G for 30 minutes and dried with a gentle N<sub>2</sub> stream; SERS spectra were recorded immediately afterward. X-ray diffraction (XRD) patterns were recorded using a PANalytical X'Pert PRO diffractometer with a scan rate of 2 degrees per minute in the range 30–50°. Energy dispersive X-ray (EDX) analysis was carried out on the same Zeiss Ultra60 SEM with an accelerating voltage of 20 kV and a working distance of 8 mm. X-ray photoelectron spectroscopy (XPS) survey scans were recorded on a Thermo K $\alpha$  XPS system with an Al K $\alpha$  source (1486.6 eV) radiation.

## 5.3 Results and Discussion

### 5.3.1 Scanning electron microscopy

Representative SEM images for AgNPs deposited on plasma treated silicon and glass surfaces are shown in Figure 35, and histograms plotting fraction versus nanoparticle diameter are given in Figure 36. Statistics calculated for each condition studied are presented in Table 5; replicates are separated by commas in the table.

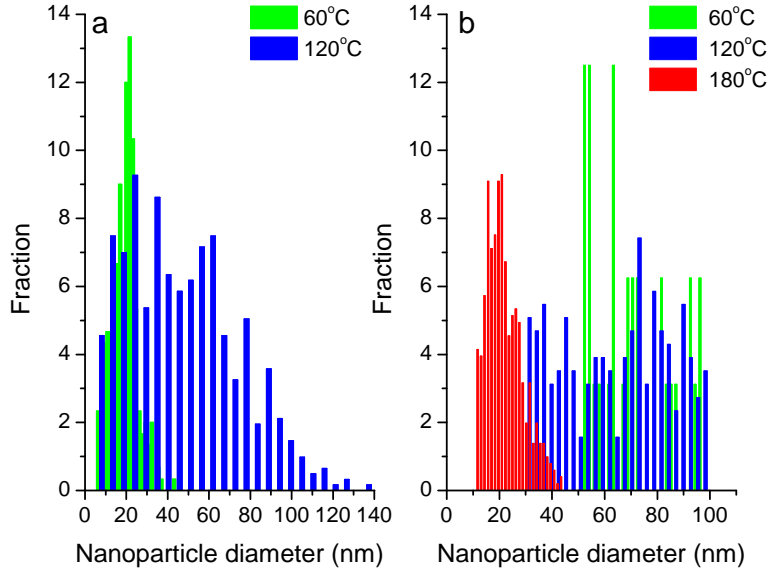


Figure 36: Histograms for AgNPs deposited on plasma treated (a) silicon and (b) glass surfaces in the temperature range 60 °C–180 °C

Table 5: Descriptive statistics for AgNPs deposited on plasma treated silicon and glass in the temperature range 60 °C–180 °C. Replicates are separated by commas; standard deviations are included for mean nanoparticle size

Substrate	Silicon			Glass		
	60 °C	120 °C	180 °C	60 °C	120 °C	180 °C
Temperature	60 °C	120 °C	180 °C	60 °C	120 °C	180 °C
Mean nanoparticle size (nm)	18.3 ± 6.7, 17.8 ± 7.4	47.5 ± 26.6, 44 ± 23.8	-	69.9 ± 14.6	64.6 ± 20.4	21.6 ± 5.98
Particle density (Particles/nm <sup>2</sup> )	8.26 × 10 <sup>-5</sup> , 3.50 × 10 <sup>-5</sup>	2.0310 <sup>-4</sup> , 1.6510 <sup>-4</sup>	-	2.31 × 10 <sup>-5</sup>	8.02 × 10 <sup>-5</sup>	6.94 × 10 <sup>-4</sup>
Mean interparticle distance (nm)	110, 169	70.2, 77.7	-	208	112	38
Fractional surface coverage of AgNPs	0.037, 0.035	0.39, 0.40	0.58	0.093	0.33	0.274

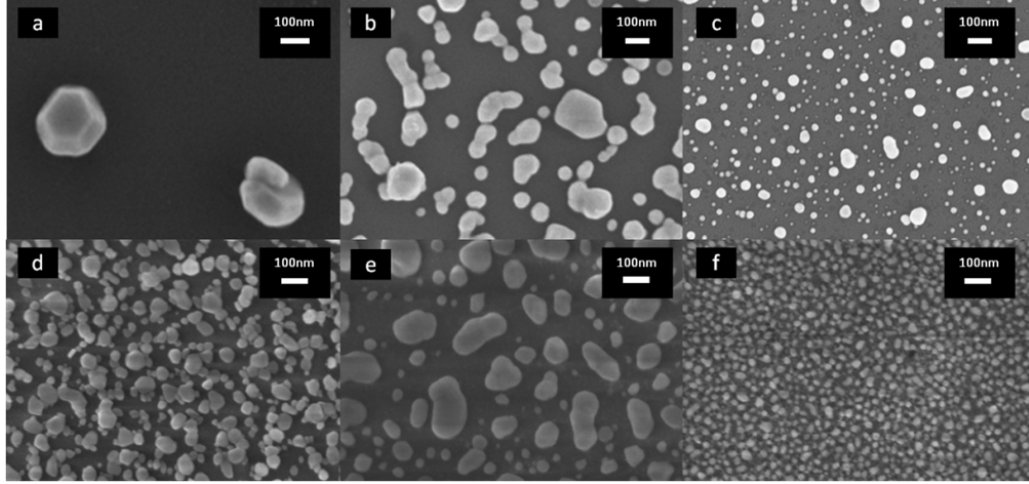


Figure 37: SEM images of AgNPs deposited on HCl treated silicon at (a) 60 °C, (b) 120 °C, and (c) 180 °C and HCl treated glass at (d) 60 °C, (e) 120 °C, and (f) 180 °C

Table 6: Descriptive statistics for AgNPs deposited on HCl treated silicon and glass at different reaction temperatures. Replicates are separated by commas; standard deviations are included for mean nanoparticle size

Substrate	Silicon			Glass		
	60 °C	120 °C	180 °C	60 °C	120 °C	180 °C
Temperature	60 °C	120 °C	180 °C	60 °C	120 °C	180 °C
Mean nanoparticle size (nm)	196 ± 56.2, 207 ± 50.2	104.5 ± 48.5, 99.3 ± 44.8	27.7 ± 20.2, 32.8 ± 26.5	24.6 ± 16.0	39.4 ± 32.9	22.8 ± 7.07
Particle density (Particles/nm <sup>2</sup> )	1.01 × 10 <sup>-6</sup> , 8.73 × 10 <sup>-7</sup>	2.16 × 10 <sup>-5</sup> , 3.63 × 10 <sup>-5</sup>	1.11 × 10 <sup>-4</sup> , 7.97 × 10 <sup>-5</sup>	3.79 × 10 <sup>-4</sup>	8.31 × 10 <sup>-5</sup>	6.61 × 10 <sup>-4</sup>
Mean interparticle distance (nm)	996, 1070	215, 166	94.9, 112	51.3	110	38.9
Fractional surface coverage of AgNPs	0.071, 0.068	0.33, 0.37	0.40, 0.42	0.26	0.17	0.3

The mean size for nanoparticles deposited on plasma treated silicon at 120 °C is about 45 nm, roughly double that of nanoparticles synthesized at 60 °C on the same surface. At 180 °C it appears that particles have begun to coalesce, precluding statistical analysis of nanoparticle size at this condition. At 60 °C, plasma treated glass supports a distribution of larger, faceted particles. Since the particles are not spherical, an equivalent particle diameter is calculated by assuming that the particles are spherical. The nonconductive nature of glass caused surface charging artifacts, leading to the lower quality image for AgNPs on glass compared to silicon. At 120 °C the particle density of larger AgNPs has increased. At 180 °C the AgNP distribution appears unimodal and the particles are densely packed; however, they do not appear to coalesce, as is the case for AgNP on plasma treated silicon.

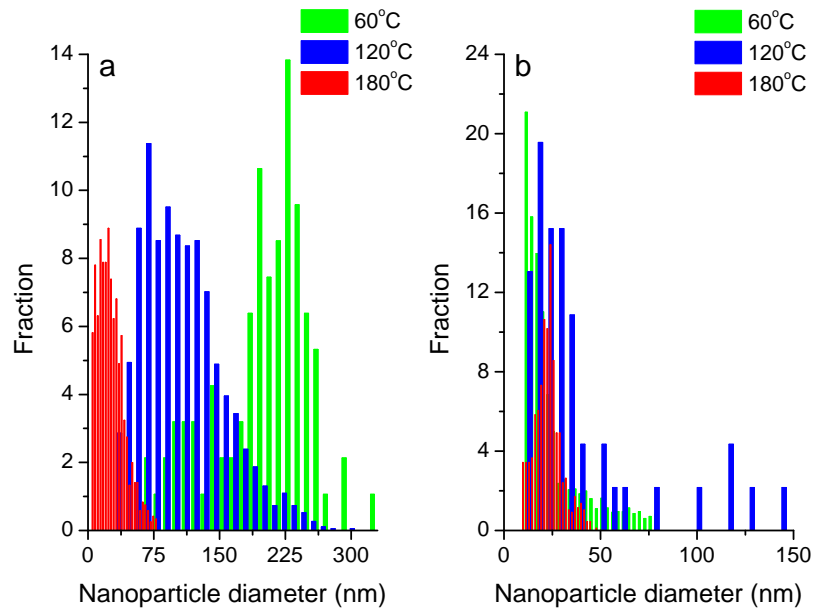


Figure 38: Histograms for AgNPs deposited on HCl treated (a) silicon and (b) glass surfaces in the temperature range 60 °C–180 °C

SEM images for AgNPs deposited on HCl treated silicon and glass surfaces are shown in Figure 37, histograms plotting fraction versus nanoparticle diameter are given in Figure 38, and statistics for each condition studied are presented in Table 6. For AgNPs deposited on HCl treated silicon at 60 °C, AgNPs have a mean size of about 200 nm, an interparticle distance of about 1 micron, and appear faceted in morphology. For AgNPs deposited on HCl treated silicon at 120 °C, the AgNPs are denser, smaller, and have less obvious faceting than those deposited at 60 °C. At 180 °C, the faceted morphology of the particles is virtually eliminated and only small, round AgNPs are observed. For HCl cleaned glass substrates, a higher density of particles was observed at 60 °C compared to HCl treated silicon at this temperature. At 120 °C, the AgNPs appear slightly larger than particles fabricated at 60 °C on HCl treated glass. Last, at 180 °C, small, dense AgNPs are fabricated on HCl treated glass, nearly identical to those deposited on plasma treated glass at 180 °C.

EDX analysis confirmed that the nanoparticles synthesized on all substrate/surface treatment combinations are in fact silver (Figure 39).

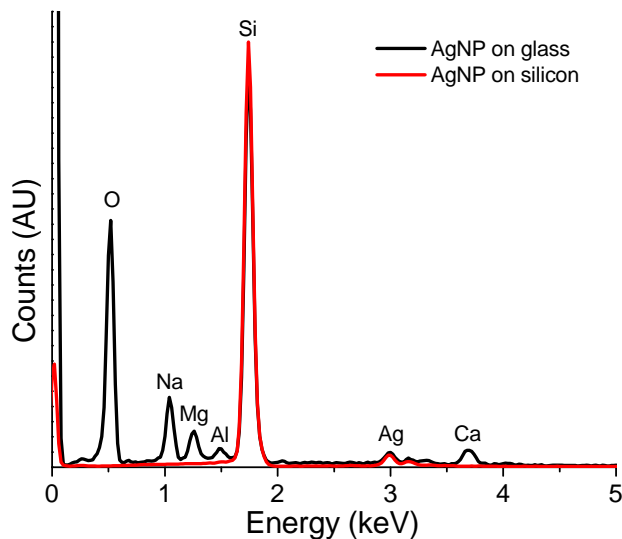


Figure 39: EDX spectra of AgNPs deposited on silicon and glass substrates

### 5.3.2 Analysis of kinetics

Previous reports have studied the reaction mechanisms for metal nanoparticle synthesis in the homogeneous, or fluid, phase of a supercritical  $\text{CO}_2$  system, where it is possible to monitor nanoparticle formation online and/or collect nanoparticles after the reaction to determine conversion [1, 206, 211]. However, these are not viable methods to study the reaction mechanisms in the system presented in the current work because AgNPs are deposited heterogeneously on a surface, making *in situ* monitoring or *ex situ* particle recovery particularly difficult. A similar challenge was addressed by Zong and Watkins, who studied the temperature and reactant concentration dependence of copper thin film deposition on substrates in  $\text{sc-CO}_2$  [335]. In that study, the film thickness was assumed to indirectly measure reaction rate because a faster reaction rate would deposit a thicker film for a fixed period of time. Under this assumption, the authors were able to gain significant insight into the underlying mechanism of the process they studied, which is a primary goal of the current work [335].

Table 7:  $R^2$  values and activation energy values for (a) plasma-treated silicon, (b) plasma-treated glass, (c) HCl-treated silicon, and (d) HCl-treated glass; 95% confidence intervals are included for activation energy values on the model prediction of the mean

Substrate	(a)			(b)			(c)			(d)		
	$R^2$	$E_a$ (kJ/mol)		$R^2$	$E_a$ (kJ/mol)		$R^2$	$E_a$ (kJ/mol)		$R^2$	$E_a$ (kJ/mol)	
Calculated from $\ln(\text{AgNP density})$	0.75	19.7	5.6	0.92	32.8	4.9	0.96	49.0	5.0	0.018	3.81	14.0
Calculated from $\ln(\text{Mean AgNP size})$	0.95	15.2	1.7	0.72	-11.8	3.4	0.93	-19.4	2.5	0.0025	-0.282	2.8

In the present study, the reaction mechanism is divided into two steps that occur in the system: first, a nucleation process where AgNP nuclei form on the surface, and second, a growth process where the existing AgNP increase in size. Applying an assumption analogous to that proposed by Zong and Watkins, AgNP density was assumed to increase with nucleation rate and mean AgNP size was assumed to increase with growth rate [335]. In other words, a faster nucleation rate would yield more particles on the surface (i.e., a higher particle density) for the fixed two hour reaction time, and a faster growth rate would yield larger particles for the fixed two hour reaction time. Under these assumptions, it is possible to fit Arrhenius plots using particle density and AgNP size. It is noted that although the nucleation process precedes growth for any particular AgNP deposited on the surface, these two processes can occur simultaneously on different sites of the surface throughout the deposition process. This observation can account for some of the larger standard deviation values reported, which add ambiguity to the Arrhenius plots fitted using mean nanoparticle size. However, this issue does not introduce any uncertainty into the Arrhenius plots fitted using nanoparticle density since the particles are simply counted and normalized by the area sampled.

The Arrhenius plots for AgNPs deposited on the four substrate/treatment combinations are shown in Figure 40; two additional data points, at 90 °C and 150 °C, are included in Figure 40a for plasma treated silicon, since AgNP size and density could not be calculated for the 180 °C condition. The  $R^2$  values and activation energies for these Arrhenius plots are given in Table 7.

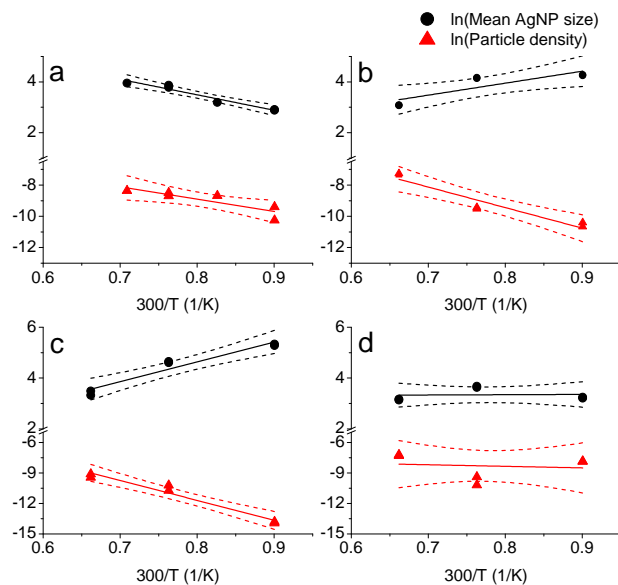


Figure 40: Arrhenius plots for AgNPs deposited on (a) plasma treated silicon, (b) plasma treated glass, (c) HCl treated silicon, and (d) HCl treated glass. Dotted lines indicate the 95% confidence interval on the model prediction of the mean

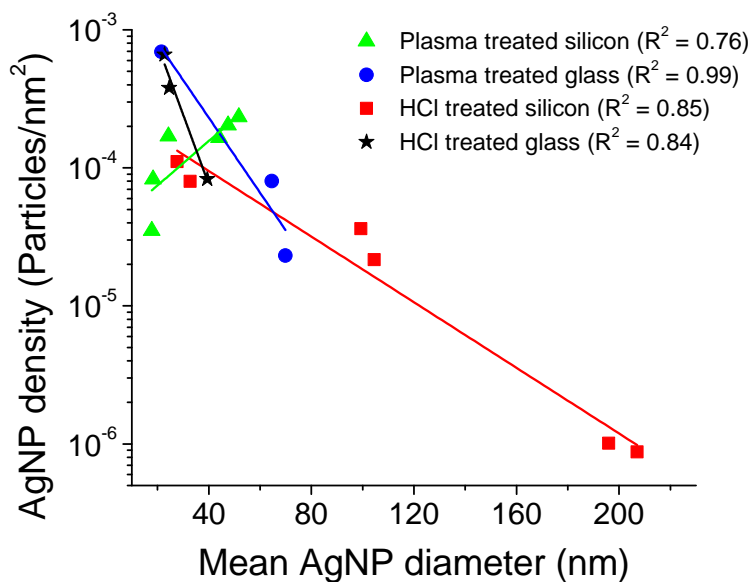


Figure 41: Combinations of AgNP mean diameters and densities that can be achieved in the sc-CO<sub>2</sub> system. R<sup>2</sup> values for the fitted lines are included in the legend

Table 8: Surface atomic percent composition of plasma and HCl treated silicon and glass substrates as measured by XPS before AgNP deposition

Element	Plasma-treated silicon	Plasma-treated glass	HCl-treated silicon	HCl-treated glass
Si	59.40	33.71	59.69	30.90
C	2.70	1.59	10.15	14.51
O	37.90	59.61	27.71	52.52
Cl	0.00	0.00	2.45	0.81
Na	0.00	2.40	0.00	0.33
Mg	0.00	0.93	0.00	0.19
Ca	0.00	1.75	0.00	0.74

The combinations of AgNP sizes and densities that can be achieved in the sc-CO<sub>2</sub> system described in this work are shown in Figure 41.

### 5.3.3 X-ray photoelectron spectroscopy

XPS analysis was conducted after plasma or HCl treatment of silicon or glass to assess the differences in the resulting surface chemistry before AgNP deposition. Surface atomic percentages measured by XPS are presented in Table 8. Oxygen plasma cleaning of the glass or silicon substrate is used to grow a thin silicon dioxide layer and remove carbonaceous contamination [149]. Here, XPS analysis showed that plasma treated silicon possessed only silicon, oxygen, and carbon on the surface. The oxygen was due to hydroxyl groups on the surface as well as adventitious water; the carbon was due to adventitious carbon contamination on the surface. For plasma treated glass, the ratio of silicon to oxygen was roughly 1:2, likely due to the presence of silicon dioxide in the glass in addition to water and hydroxyl groups on the surface. Also, the glass components sodium, magnesium, and calcium were detected, along with adventitious carbon. HCl treatment is usually used to remove metallic contamination from a surface, but it does not remove carbonaceous contamination from or oxidize a surface [214]. Here, XPS analysis revealed that HCl treatment did not reduce carbonaceous contamination and did not increase the oxygen content of the silicon and glass surfaces in comparison to the plasma treated substrates. HCl treatment also left behind a small amount of chlorine contamination on the silicon and glass

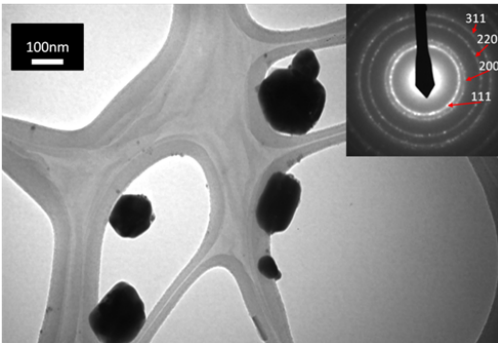


Figure 42: TEM image of AgNPs deposited on HCl treated silicon 60 °C, removed and placed on lacy carbon TEM grid. Inset shows the SAED pattern indicating fcc crystal structure

surfaces.

#### 5.3.4 Transmission electron microscopy and selected area electron diffraction

In order to investigate the crystal structure of AgNPs deposited on silicon through selected area electron diffraction (SAED), AgNPs deposited on HCl treated silicon at 60 °C were mechanically removed by carefully scraping a lacy carbon TEM grid (Ted Pella) along the surface of the silicon wafer [268]. The inset SAED pattern in Figure 42 confirms the polycrystalline fcc structure of the AgNPs deposited on silicon at this condition.

#### 5.3.5 X-ray diffraction

XRD analysis was conducted to demonstrate the crystal structure of AgNPs deposited on glass; XRD diffractograms are not shown for AgNPs deposited on silicon because the signal intensity due to diffraction from the silicon substrate was so high that peaks from diffraction due to AgNPs were obscured. Since XRD patterns were recorded for glass samples, mechanical removal of the nanoparticles for TEM/SAED investigation was not pursued. The XRD diffractograms shown in Figure 43 confirm the fcc structure of the AgNPs deposited on plasma and HCl treated glass. The (111) crystal face is dominant over the (200) face; higher order peaks were not observed when XRD

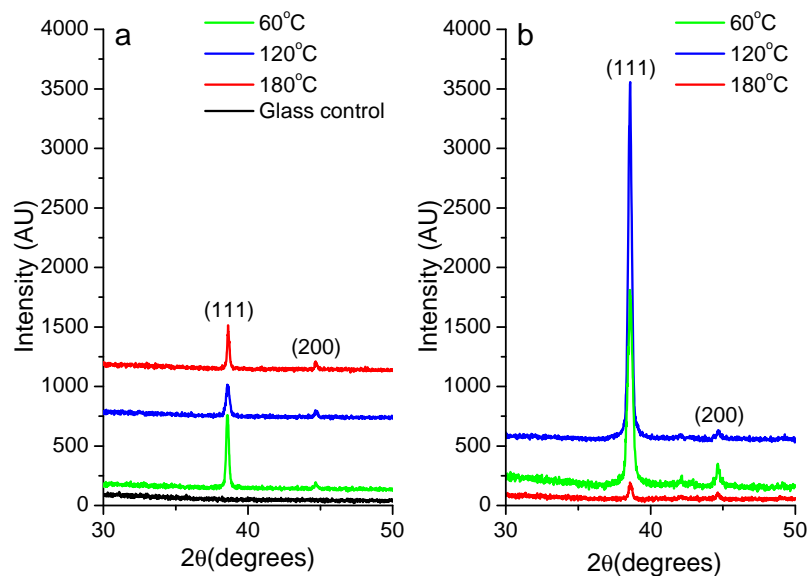


Figure 43: XRD diffractogram of AgNPs deposited on (a) plasma treated and (b) HCl treated glass. Spectra were offset slightly to ease interpretation

spectra were collected above 50 °. Spectra were offset slightly to ease interpretation.

### 5.3.6 Surface enhanced Raman spectroscopy

SERS activity was studied for AgNPs deposited on each substrate/surface treatment condition. Figure 44 shows a Raman spectrum for R6G on AgNPs deposited at 120 °C on plasma treated silicon. Spectra of control samples without AgNPs confirm the need for AgNPs to enable the SERS effect, and control samples without R6G confirm that the detected signal is not due to either AgNPs or ligands attached to the surface from the Ag(hfac)(COD) precursor. The Raman active vibrational modes for R6G that were observed have been previously assigned as  $\nu(\text{C-C-C})$  ring bending mode at 614  $\text{cm}^{-1}$ ;  $\nu(\text{C-H})$  out-of-plane bending mode at 774  $\text{cm}^{-1}$ ;  $\nu(\text{C-H})$  in-plane bending mode at 1183  $\text{cm}^{-1}$ ; and  $\nu(\text{C-C})$  stretching modes at 1363  $\text{cm}^{-1}$ , 1509  $\text{cm}^{-1}$ , 1572  $\text{cm}^{-1}$ , and 1650  $\text{cm}^{-1}$  [124]. These peaks appear in all subsequent SERS spectra. The plateau peak in the range 975  $\text{cm}^{-1}$ –925  $\text{cm}^{-1}$  is assigned to silicon [282]. Figure 45 shows the SERS spectra for R6G on AgNPs deposited at the three reaction temperatures

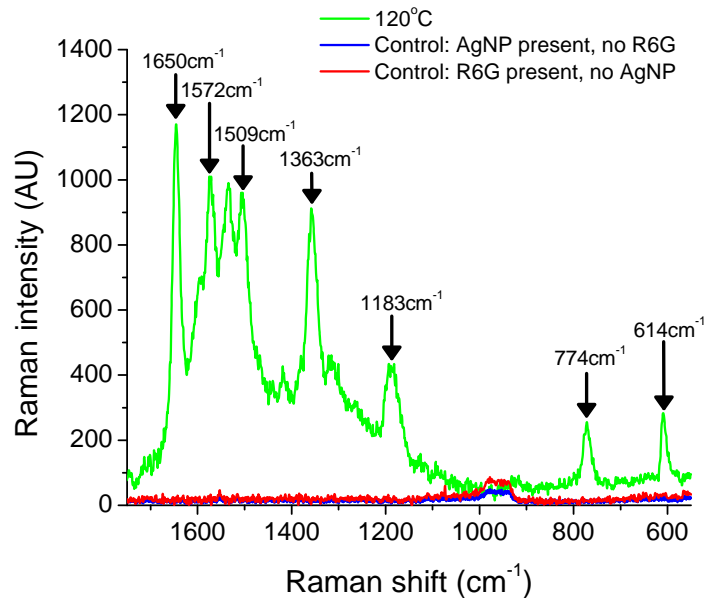


Figure 44: SERS spectra of  $1 \times 10^{-6}$  R6G on AgNPs deposited at 120 °C on plasma treated silicon as well as controls lacking either R6G or AgNPs. R6G peaks are assigned

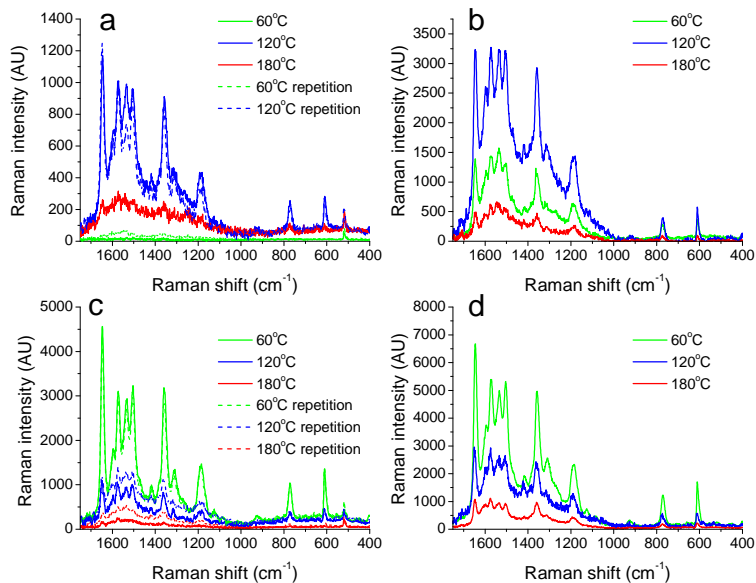


Figure 45: SERS spectra of  $1 \times 10^{-6}$  R6G on AgNPs deposited on (a) plasma treated silicon, (b) plasma treated glass, (c) HCl treated silicon, and (d) HCl treated glass

Table 9: SERS enhancement factors for AgNPs coated surfaces synthesized at 60 °C, 120 °C, and 180 °C. Replicates are separated by commas in the table

	Plasma-treated silicon	Plasma-treated glass	HCl-treated silicon	HCl-treated glass
60 °C	1×10 <sup>1</sup> , 1×10 <sup>1</sup>	3×10 <sup>5</sup>	9×10 <sup>5</sup> , 9×10 <sup>5</sup>	1×10 <sup>6</sup>
120 °C	2×10 <sup>5</sup> , 2×10 <sup>5</sup>	6×10 <sup>5</sup>	8×10 <sup>4</sup> , 8×10 <sup>4</sup>	6×10 <sup>5</sup>
180 °C	4×10 <sup>4</sup>	1×10 <sup>5</sup>	2×10 <sup>4</sup> , 4×10 <sup>4</sup>	2×10 <sup>5</sup>

for each substrate/surface treatment combination studied.

The SERS enhancement factor (EF) can be estimated in order to compare the signal enhancement between each sample. The SERS EF can be calculated as:

$$EF_{SERS}(\omega_\nu) = \frac{(I_{SERS}(\omega_\nu))/(N_{SERS})}{(I_{NRS}(\omega_\nu))/(N_{NRS})} \quad (5)$$

where  $EF_{SERS}(\omega_\nu)$  is the SERS enhancement factor as a function of the scattering frequency  $\omega_\nu$ ;  $I_{SERS}(\omega_\nu)$  is the SERS enhanced Raman intensity normalized by  $N_{SERS}$ , the number of analyte molecules bound to the surface;  $I_{NRS}(\omega_\nu)$  is the normal Raman scattering intensity normalized by  $N_{NRS}$ , the number of analyte molecules bound to the surface; and  $\omega_\nu$  is the Raman scattering frequency [308]. The EF was calculated using the  $\omega_\nu = 1650 \text{ cm}^{-1}$  peak for all samples since this peak was clearly discernible for each spectrum. To measure  $I_{NRS}(\omega_\nu)$ , uncoated glass and silicon surfaces were immersed in 0.1 M R6G for 30 minutes and then analyzed by the Raman microscope as done for all other samples. Values for  $N_{SERS}$  and  $N_{NRS}$  were assumed to depend only on the molarity of the R6G solution used and not on the adsorption efficiency of R6G on the silicon and glass surfaces, a conservative assumption that presumes a high degree of surface coverage of R6G [152]. Thus,  $N_{SERS}$  was estimated to be  $6.02 \times 10^{17}$  molecules R6G and  $N_{NRS}$  was estimated to be  $6.02 \times 10^{22}$  molecules R6G. EF values for each sample are given in Table 9.

### 5.3.7 Heterogeneous AgNP deposition on substrates in sc-CO<sub>2</sub>

It was hypothesized that increasing temperature would increase both the size and nanoparticle density for every substrate/surface treatment combination studied; however, results indicate this occurred only for plasma treated silicon. Analysis of SEM images showed that for plasma treated silicon substrates, the mean AgNP size, density, and surface coverage increased as temperature increased (Table 5). Moreover, the Arrhenius plots shown in Figure 40a indicate that both nanoparticle size and nanoparticle density increased with temperature. Since a traditional kinetic mechanism comprised of elementary molecular steps was not postulated here, the absolute values of the activation energies corresponding to the Arrhenius plots were not useful for comparisons to other reaction systems or between substrate/treatment conditions in this system. Nonetheless, the Arrhenius dependence demonstrated here indicates that the nucleation and growth processes were both thermally activated for AgNPs deposited on plasma treated silicon. Furthermore, this dependence on temperature suggested that the overall deposition process on plasma treated silicon was reaction limited and not limited by transport of the Ag(hfac)(COD) precursor to the surface. This was not surprising since organometallic precursors are highly soluble in sc-CO<sub>2</sub> compared to other systems where precursor transport is often the rate-limiting process, such as chemical vapor deposition [13, 303]. In addition, the low temperature range used in the present work also favors a reaction limited regime over a transport limited regime [96]. Overall, these results imply that temperature can be used to tune AgNP size and density on plasma treated silicon. However, the AgNP size and density on plasma treated silicon cannot be tuned independently: increasing temperature increased both particle size and particle density.

For AgNPs deposited on plasma treated glass and HCl treated silicon, Arrhenius plots indicated that mean AgNP size decreased with temperature while particle density increased with temperature (Figures 40b and 40c). These results indicated

that the growth process for AgNPs deposited on these surfaces was not thermally activated while the nucleation process was thermally activated. These data contrast with those observed for plasma treated silicon, where mean AgNP size and particle density both increased with temperature. Furthermore, for plasma treated glass and HCl treated silicon substrates, mean AgNP size decreased as particle density increased (Figure 41), again in contrast to results from AgNPs deposited on plasma treated silicon.

XPS data clearly indicated that the plasma treated silicon and glass substrates and the HCl treated silicon substrate have significantly different compositions of species on the surface (Table 8). Consequently, although nucleation density increased with temperature for the three substrate/surface treatment combinations discussed thus far, it is hypothesized that chemical species on the surface are responsible for differences in the nucleation and/or growth of AgNPs on plasma treated glass and HCl treated silicon compared to plasma treated silicon. For example, glass possesses several cationic species ( $\text{Na}^+$ ,  $\text{Ca}^{2+}$ , and  $\text{Mg}^{2+}$ ) that may have repelled the positively charged silver center in the  $\text{Ag}(\text{hfac})(\text{COD})$  precursor as it attempted to adsorb and/or diffuse on the surface, limiting particle nucleation and/or growth. For HCl treated silicon, the HCl treatment did not oxidize the surface or remove carbonaceous contamination from the silicon surface compared to the plasma cleaned silicon surface (Table 8). Thus, the lack of hydroxyl groups on the surface or the presence of carbon-containing surface contamination may have decreased the adsorption and/or surface mobility of the  $\text{Ag}(\text{hfac})(\text{COD})$  precursor in a manner similar to that posited for cationic species in plasma treated glass.

Regardless of the nucleation and growth mechanism, it is apparent that surface chemistry had a significant effect on mean AgNP size and nucleation density. Furthermore, at low AgNP densities, large AgNPs were able to form on the plasma treated glass and HCl treated silicon surfaces, while at high AgNP densities, only

small AgNPs were able to form. From this observation, it is hypothesized that the nuclei on these two surfaces undergo competition for precursor: as the nucleation density increased, competition for the Ag(hfac)(COD) precursor increased, yielding smaller AgNPs. Conversely, as nucleation density decreased, more Ag(hfac)(COD) precursor was available per nucleus for growth, yielding larger AgNPs. In addition to competition, particles may experience a crowding effect on the surface: at higher particle densities, there may not be enough space for particles to continue growth, while at lower particle densities, growth may be possible. This explanation can also account for the positive slope and negative activation energies reported for the Arrhenius plots shown in Figure 40 and Table 7, respectively: as temperature increased, particle density increased due to a faster nucleation rate, leading to more competition for precursor on these surfaces and consequently smaller AgNPs.

Nonetheless, it is noted that the surface chemistry of the plasma treated silicon surface did not induce this competition effect for AgNP deposition: as AgNP density increased on the plasma treated silicon surface, larger particles were deposited, in contrast to the results obtained for plasma treated glass and HCl treated silicon surfaces. Compared to these two surfaces, plasma treated silicon did not possess significant levels of cationic or carbon-containing species on the surface. Thus, these contrasting results support the hypothesis that surface chemistry has a mediating role for AgNP growth as well as the role in controlling AgNP nucleation that was described above. For example, it is possible that the surface chemistry of plasma treated silicon allowed AgNP nucleation and growth to be thermally controlled, in contrast to results for plasma treated glass and HCl treated silicon, where surface species likely affected adsorption and/or diffusion of the precursor as it migrated toward nascent particles.

Last, for AgNPs deposited on HCl treated glass, there does not appear to be any correlation between temperature and either the mean AgNP size or particle density in the Arrhenius plots shown (Figure 44d). This result implies that the nucleation and

growth processes were not thermally activated for this substrate/surface treatment combination and that some other process may have controlled particle deposition here, in contrast to the results obtained for plasma treated silicon and glass and HCl treated silicon. However, mean AgNP size did increase as particle density decreased (Figure 41), again implying that the surface chemistry may have caused competition for precursor on this surface even though neither nucleation nor growth was thermally activated.

The range of AgNP sizes and densities that can be achieved in the sc-CO<sub>2</sub> system described in this work is shown in Figure 41. It is clear that mean AgNP size can be tuned over an order of magnitude (20–200 nm) and particle density can be tuned over three orders of magnitude ( $10^{-6}$ – $10^{-3}$  AgNP/nm<sup>2</sup>) simply by changing the temperature and substrate used in the deposition route, while the mechanistic considerations described above account for the behavior observed in Figure 41. Moreover, understanding the mechanisms that govern the heterogeneous deposition of AgNPs in the sc-CO<sub>2</sub> system can ultimately lend insight into how to choose process conditions for the end use application, which in this work is SERS.

The deposition of AgNPs on the glass substrates can be contrasted to the deposition of CZTS on the SiO<sub>2</sub> substrates described in Chapter 2. Since both substrates are predominantly made of SiO<sub>2</sub>, one would expect that the morphologies of the deposited materials (CZTS and Ag) would be similar. However, such behavior is not observed here, as CZTS forms a continuous thin film on the surface of SiO<sub>2</sub> while discrete AgNPs deposit on the glass substrate. One potential explanation is that the Ag(hfac)(COD) precursor does not nucleate as well on SiO<sub>2</sub> as well as the dithiocarbamate precursors used for CZTS deposition. Alternatively, it is possible that the temperature used in AgNP deposition (60 °C – 180 °C) is not high enough to encourage film formation, whereas at 300 °C it was possible to form a CZTS film. At the 180 °C condition it is possible that the AgNP are transitioning to a film. Last,

the precursor concentration of Ag(hfac)(COD) may have been too low to enable film formation.

### 5.3.8 SERS application of AgNP coated substrates fabricated in sc-CO<sub>2</sub>

SERS active surfaces were successfully fabricated on both silicon and glass substrates under both plasma and HCl treatment conditions; R6G was detected at a concentration of 1  $\mu$ M. Recent work by Stampeleskie et al. showed that the SERS EF for R6G on AgNPs depended linearly on the size of the nanoparticles in the range from 10–70 nm while the SERS EF varied over the range  $1 \times 10^5$  to  $3 \times 10^5$ . Thus, although there was an observed correlation between AgNP size and SERS EF, manipulating AgNP size alone in this previous work did not afford a method for significantly tuning SERS activity by orders of magnitude. Nonetheless, the SERS EF observed in the current study were clearly within the range observed in the previous work. Furthermore, the sensitivity of the SERS surfaces studied here (1  $\mu$ M) was a three orders of magnitude improvement over previous reports using sc-CO<sub>2</sub> to fabricate SERS active surfaces [118].

AgNP properties had a clear effect on SERS EF for two of the substrate/treatment combinations studied in the current work. First, for AgNPs deposited on plasma treated silicon surfaces, the SERS EF exhibited a maximum at 120 °C but significantly lower values at 60 °C and 180 °C. This behavior is explained by considering the effects of both nanoparticle size and surface coverage presented in Table 5. While the roughly 18 nm AgNPs fabricated at 60 °C on plasma treated silicon should be SERS active according to previous reports, the surface coverage (0.035) is too low to effectively support a significant SERS EF, calculated here to be  $1 \times 10^1$  [118, 264]. At 180 °C, the surface coverage of the Ag nanofilm (0.58) was high enough to sustain a SERS EF, calculated to be  $4 \times 10^4$  [216]. At 120 °C, discrete particles in the 40 nm range were observed and the surface coverage (0.40) of the AgNPs was high enough to allow a

SERS EF of 2105, in agreement with previous studies [264]. Thus, for plasma treated silicon, there was a clear correlation between temperature and AgNP properties that ultimately influenced SERS EF.

Second, for AgNPs deposited on plasma treated glass surfaces, another optimum was observed at 120 °C. The same explanation is offered for this surface as for plasma treated silicon: at 60 °C, the AgNP decorated surface did not have enough AgNPs to enable a significant SERS effect, while at 180 °C the particles were not sufficiently isolated, limiting localized surface plasmon resonance effects. For the other substrate/surface treatment conditions studied, there were no clear relationships correlating temperature to AgNP properties and their effect on SERS enhancement factor.

The overall lack of a clear relationship between AgNP properties and SERS EF for HCl treated silicon and glass indicates that other factors may have influenced the SERS effect. One possible explanation for this is the presence of other species on the surface that somehow modulate the efficiency of the SERS active surface. For example, previous reports have shown that the chloride anion can have an activating effect in SERS, and chloride was detected by XPS on surfaces treated with HCl [210, 225, 259]. Thus, it is possible that the presence of chloride ion on the surface influenced the SERS enhancement factor in addition to the AgNPs on the surface.

It should also be noted that the most frequently observed SERS EF over all of the conditions studied is on the order of  $10^5$ . Previous reports have demonstrated SERS EF using AgNPs on the order of  $10^8$ – $10^{12}$  with the ability to detect analytes at concentrations of  $10^{-12}$  M [48, 102, 170]. These studies achieve such high sensitivity by fabricating anisotropic silver nanostructures or depositing spherical AgNPs on more exotic substrates such as silicon nanowires [48, 102, 170]. Thus, future studies should focus on ways to increase the SERS efficiency of surfaces modified in sc-CO<sub>2</sub> by exploring such alternatives. In particular, due to its lower viscosity and zero surface tension compared to liquid processing methods, sc-CO<sub>2</sub> is well-suited to

deposit nanoparticles in two- or three-dimensional structures where liquids would be transport limited for nanoparticle deposition by higher viscosity and surface tension.

## **5.4 Conclusion**

The results presented here provide scientific insight into the underlying mechanisms that control heterogeneous AgNP deposition on surfaces in the sc-CO<sub>2</sub> system as well as engineering insight into what parameters can be used to tune AgNP properties such as size, density, and surface coverage. For plasma treated silicon, it was shown that both the nucleation and growth processes were thermally activated and temperature was used to tune both the nanoparticle size and density. For plasma treated glass and HCl treated silicon, it was shown that the nucleation process was thermally activated, and furthermore that the combination of substrate/surface treatment had a significant effect on both the nucleation and growth processes by limiting nucleation and/or growth (similar to Chapters 3 and 4) to ultimately cause competition for the silver precursor.

While the exact molecular mechanisms of these processes remain uncertain, it is clear from this work that temperature and surface chemistry significantly influenced the nucleation and growth processes, ultimately influencing the size, particle density, and surface coverage of AgNPs deposited on silicon and glass substrates. This chapter advances the theme developed in Chapters 2 through 4 that the surface chemistry of the substrate has a significant influence on the nucleation and growth of nanoparticles in the sc-CO<sub>2</sub> deposition system.

In addition, these results offer two simple, useful variables that can be used to tune the properties of AgNPs deposited on substrates by the sc-CO<sub>2</sub> system. The AgNPs deposited on silicon and glass served as SERS active substrates that could detect R6G at a concentration of 1  $\mu$ M, which represents a three orders of magnitude improvement over previous efforts to fabricate SERS substrates using sc-CO<sub>2</sub>. Furthermore, it was

shown that the AgNP properties had a significant effect on the SERS efficiency.

Finally, this chapter concludes the PSP investigations carried out for sc-CO<sub>2</sub> fabrication techniques in this thesis. In the following chapters, novel experimental design approaches are implemented to rapidly optimize the synthesis of nanomaterials in sc-CO<sub>2</sub>. The AgNP deposition process described in this chapter is used as the model system for implementing the novel experimental design methods described in Chapters 6 through 8.

## CHAPTER VI

# LAYERS OF EXPERIMENT WITH ADAPTIVE COMBINED DESIGN

### *6.1 Introduction*

In Chapters 2 through 5, the process-structure-property relationships of various nanomaterials synthesized in supercritical carbon dioxide were investigated. In this chapter, the first novel experimental design methodology is developed and implemented for optimizing the deposition of AgNPs on a silicon wafer surface in supercritical carbon dioxide. Here, optimization implies finding the process conditions (temperature) that yields the desired mean nanoparticle size of the fabricated products. A short introduction to the current methods used for experimental design under uncertainty are described, and this is followed by a description of the contributions of the Layers of Experiment with Adaptive Combined Design methodology.

Models are used by engineers and scientists to understand and improve a process. Once a model has been built, it can be used to predict the results of future experiments or locate optimum process conditions. Models can be either mechanistic or empirical, depending on how they are constructed. Mechanistic models are based on the fundamental physical laws that govern a process, such as a chemical reaction, in order to fit the parameters in the system, such as reaction rate coefficients [169, 305]. Empirical models do not invoke a model structure from first principles; instead, a simple model structure (e.g. polynomial) is selected and fit by the experimental data [193]. In order to refine either type of model, it is often necessary to conduct sequential experiments based on results from previous experiments [2, 249]. Thus, planning

experiments, selecting the best model structure, and refining this structure are distinct challenges for the experimenter constructing a model of a chemical process.

Mechanistic models generally have greater predictive power than empirical models since they utilize fundamental scientific understanding of the process [31]. For this reason, mechanistic models can be used with more confidence than empirical models to extrapolate from the data, i.e., to predict responses outside of the region of experimental data collection [28]. Lastly, mechanistic models can be reformulated if the process under study changes in a significant way, without the need to collect data to identify a new model from the very beginning, a step that would be necessary for an empirical model [267].

Systems are often studied under highly idealized conditions to simplify the corresponding mechanistic model. For example, a surface reaction system when studied under ultra-high vacuum (UHV) conditions on a single crystalline surface is significantly simplified compared to the actual conditions where a catalyst would be applied [60]. This idealized system can be represented by a simpler mechanistic model than would a more realistic reaction system at atmospheric pressure on a polycrystalline surface; furthermore, it is possible to collect experimental data both *in situ* through spectroscopy and *ex situ* through measurements of metrics such as conversion by using this simplified system [20, 173, 205, 302].

To study more complicated and realistic surface reaction systems, previous reports have combined mechanistic and empirical modeling techniques, making it possible to study catalytic surface reactions over a wider range of pressure conditions and materials compared to UHV, single crystalline systems [3, 227]. For example, Vlachos and coworkers have established models for hydrogen formation from methane and hydrogen oxidation on the surface of a polycrystalline platinum catalyst at atmospheric pressure by implementing a hierarchical, multiscale modeling technique [186, 219]. This technique optimized the kinetic parameters while increasing the usefulness of

the resulting models by incorporating thermodynamic data in the semi-empirical model [65, 187]. Thus, it was possible to postulate a reaction mechanism, develop a semi-empirical model based on this reaction mechanism and previously collected data, refine the model, and validate it against further experimental data collected outside the design window used to construct the model.

Nonetheless, not all chemical reaction systems can be confidently described from first principles calculations, i.e., in terms of a postulated reaction mechanism. This is especially true in advanced technology processes such as nanofabrication: it is challenging to simultaneously propose, select, fit, and optimize empirical and/or mechanistic models for nanomanufacturing processes. In such cases, one common approach is to implement a factorial experimental design. Xu et al. implemented a sequential fractional factorial experimental design approach to maximize the aspect ratio of zinc oxide nanorods synthesized in a hydrothermal process [319]. Alternatively, empirical or hybrid (semi-empirical) models can be proposed for complicated systems where the underlying processes are difficult to describe mechanistically or are not well understood. Wissmann and Grover proposed a novel sequential experimental design methodology employing both empirical and hybrid models in order to optimize the film roughness of a yttrium film fabricated in a chemical vapor deposition process [310, 311]. The authors compared the use of a random (model free) design and a D-optimal (model dependent) experimental design for conducting each experiment in a sequential manner. The random experimental design was shown to be better than the D-optimal design for finding the process optimum when conducting experiments one at a time (i.e., not in a batch-wise manner).

While these approaches address critical challenges in experimental design for nanofabrication, there are several key issues that remain unexplored. For example, there may be significant uncertainty in the *design region* of a nanomanufacturing process as well as uncertainty in *model structure* for the process. Moreover, conducting

many experiments throughout an unknown design region is prohibitively expensive in terms of both time and money for nanomanufacturing, motivating the need to efficiently allocate the number of experiments necessary to model and/or optimize a process. Lastly, it is often necessary to meet some engineering tolerance for a nanofabrication process given significant uncertainty in either the design region or model structure of a process. Consequently, it is vital to develop a systematic procedure to study and optimize a nanofabrication process that presents these three distinct challenges.

These issues are addressed in the current work, which presents a novel sequential experimental design methodology, termed Layer of Experiments (LoE) with Adaptive Combined Design (ACD), to optimize a nanofabrication process. The LoE component of this methodology can “zoom in” or “zoom out” to find the process optimum after each round of experiments based on a novel uncertainty metric that takes into account stochastic, parameter, and structural uncertainty. Consequently, this LoE algorithm decreases uncertainty in the design region while also implementing an evaluation metric to determine whether the model is sufficiently accurate for the engineering tolerance specified by the investigator. Since experiments are conducted in layers (as opposed to sequentially one at a time), characterization costs are reduced and random blocking can be implemented to reduce experimenter bias. The ACD component of the LoE/ACD method balances two goals: exploring the region around the process optimum by using a space-filling design while refining the model parameters using a D-optimal design. It should be noted that the LoE/ACD methodology is implemented to model and optimize the mean behavior of a system and focuses on uncertainty of the mean behavior, as opposed to uncertainty attributed to within- or between-batch variance.

The proposed LoE/ACD methodology is implemented to model and optimize a sc-CO<sub>2</sub> assisted deposition process for silver nanoparticles (AgNPs). The sc-CO<sub>2</sub>

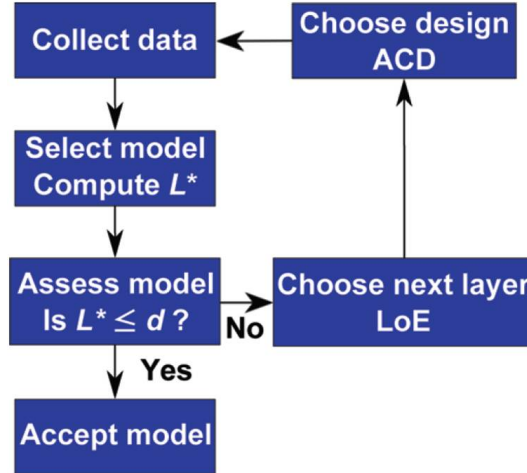


Figure 46: Layers of Experiments with Adaptive Combined Design Algorithm. The uncertainty metric  $L^*$  is used to assess model accuracy in each layer of experiments

process is a nanofabrication technique that is environmentally friendly and has been employed extensively to deposit metal nanoparticles on substrates for applications in microelectronics [39, 303] and catalysis [168, 323, 328]. However, rigorous modeling and optimization approaches to the sc-CO<sub>2</sub> nanofabrication system have not been pursued since it is a relatively new advanced technology that has a design region with significant uncertainty, does not possess a well-defined model structure, and is not easily characterized by *in situ* or *ex situ* techniques. Consequently, it is an ideal system to study using the proposed experimental design methodology. The LoE/ACD technique successfully reduced the design region sequentially, concentrated design points around the process optimum, and found the process optimum by conducting 12 total experiments (six in each layer).

## 6.2 Methodology

The overall LoE/ACD approach is outlined in Figure 46. First, a set of experiments is conducted and data is collected. Then, an empirical model is chosen and the model is fit using the experimental data. Next, the accuracy of the predictions made by the model is assessed. If the accuracy is within the engineering tolerance set by the

experimenter, the model is deemed acceptable and used to optimize the process. If not, the next subregion for experiments is selected using the LoE technique, design points are chosen using the ACD methodology, and the algorithm iterates until the accuracy of the model falls within the engineering tolerance set by the experimenter. Each of these steps is described in detail below.

### 6.2.1 Model Selection

Several methods have been used to select the best model from a set of candidate models based on experimental data. Three different methodologies are used here for model selection: the Akaike Information Criterion (AIC) [38], the Bayesian probability ( $P_B$ ) [266], and the minimization of the confidence interval. The AIC is given by:

$$\text{AIC}_j = n(\ln(2\pi \text{MSE}_j) + 1) + 2p_j \quad (6)$$

where  $n$  is the number of experiments conducted,  $p_j$  is the number of parameters in model  $j$ , and  $\text{MSE}_j$  is mean squared error:

$$\text{MSE}_j = \frac{\sum_{i=1}^n (y(\mathbf{x}_i) - \hat{y}_j(\mathbf{x}_i))^2}{n} \quad (7)$$

where  $y(\mathbf{x}_i)$  are the observed experimental responses and  $\hat{y}_j(\mathbf{x}_i)$  are the responses predicted by model  $j$ . The model structure with the smallest AIC is chosen as the best fit for the data. The Bayesian probability  $P_B$  is calculated as

$$P_B = P(M_j) \times 2^{-p_j/2} \times \text{MSE}_j^{-\nu_e/2} \quad (8)$$

where  $P(M_j)$  is the *a priori* likelihood of model  $M_j$  and  $\nu_e$  is the number of repetitions for each data point. The model with the largest  $P_B$  is chosen as the best fit for the data. The confidence for model  $j$  interval is defined by:

$$\text{CI}_j(\mathbf{x}) = \pm t_{\alpha, n-p_j} \sqrt{\sigma_j^2(\mathbf{x})} \quad (9)$$

where  $\alpha$  is the confidence level selected by the experimenter. The predicted variance,  $\sigma_j^2(\mathbf{x})$ , is given by:

$$\sigma_j^2(\mathbf{x}) = \mathbf{a}^{(j)}(\mathbf{A}_j^T \mathbf{A}_j)^{-1} \mathbf{a}^{(j)T} \hat{\sigma}_j^2 \quad (10)$$

The model variance,  $\hat{\sigma}_j^2$ , is given by:

$$\hat{\sigma}_j^2 = \frac{\sum_{i=1}^n (y(\mathbf{x}_i) - \hat{y}_j(\mathbf{x}_i))^2}{n - p_j} \quad (11)$$

which is similar to Eq. 7 except that  $p_j$  degrees of freedom have been lost by assuming a model structure and this must be subtracted from  $n$  in the denominator.  $\mathbf{a}^{(j)}$  is defined as the row vector  $\frac{\partial \hat{y}_j}{\partial \theta} |_{\mathbf{x}}$  and the design matrix for model  $j$ ,  $\mathbf{A}_j$ , is defined as  $\frac{\partial \hat{y}_j}{\partial \theta} |_{\mathbf{x}_i}$ . The  $\text{CI}(\mathbf{x})$  function is optimized over the design space, and the model structure with the smallest confidence interval is chosen as the best fit for the data. The model fitting was carried out by least squares fitting in MATLAB R2010a.

### 6.2.2 Assessment of Model Accuracy

In this work, uncertainty on the mean prediction of the model is studied; modeling of variance is not considered. Uncertainty in a model is usually divided into three components: structural uncertainty, which deals with uncertainty in model structure; parameter uncertainty, which introduces uncertainty due to estimation of model parameters that are not known exactly; and stochastic uncertainty, due to randomness in the process that is difficult to reduce [62]. Parameter and stochastic uncertainty are usually quantified using a confidence interval measurement; however, these do not assess structural uncertainty. Since nanofabrication processes possess significant structural uncertainty in addition to uncertainty within and between experimental runs, it is important to assess all three types of uncertainty when deciding whether a model is acceptable within engineering tolerance. However, this has not been previously pursued, to the best of our knowledge. Thus, a novel uncertainty metric,  $L$ , was proposed and defined as [148]

$$L = \max(|T - (\hat{y}(\mathbf{x}) + \text{CI}(\mathbf{x}))|, |T - (\hat{y}(\mathbf{x}) - \text{CI}(\mathbf{x}))|) \quad (12)$$

where  $T$  is the targeted value for the process output and  $CI(\mathbf{x})$  is the confidence interval defined in Eq. 9. The uncertainty metric,  $L$ , is optimized over the design space:

$$\mathbf{x}^* = \min_{\mathbf{x}} L(\mathbf{x}) \quad (13)$$

The result of this optimization,  $L^*$ , is compared to some preselected engineering tolerance,  $d$ . If  $L^* > d$ , the algorithm dictates that the experimenter continue on to the next layer of experiments in order to further refine the model and find the process optimum. If  $L^* \leq d$ , the model is accurate to within the necessary engineering tolerances specified by the experimenter and can be used to optimize the process. Optimization routines were performed using the *fminunc* function in MATLAB 2010a.

### 6.2.3 Selection of Next Layer

A key component of the LoE methodology is the ability to “zoom in” or “zoom out” on the next region for data collection. This procedure is important in efficiently handling uncertainty in the design region: the next layer will “zoom in” on a design region if the optimum is found within the selected region, or “zoom out” if the process optimum is not found in the selected region and change the design window for the next layer of experiments. In addition, this ability to “zoom in” is critical for the efficient allocation of resources in a smaller design window near the process optimum. The LoE procedure must balance the objective of decreasing the window for the next layer as much as possible with the objective of assuring that the process optimum is not left out of the next layer. The first step to choose a new layer is selecting the center of the new region. This could be achieved by simply optimizing

$$\min_{\mathbf{x}} |T - \hat{y}(\mathbf{x})| \quad (14)$$

However, if there is significant uncertainty regarding the model structure (as will be the case for a nanofabrication process), this is not desirable. Instead, bootstrapping is

used to resample residuals to generate a distribution of center point values using multiple potential model structures and optimizing these models as described by Eq.14. The details of this procedure are described elsewhere [148]. Once this histogram has been constructed, the center of the new subregion,  $c^*$ , is calculated as the mean of the most frequent bin in the histogram.

After the center point has been determined, the size of the next layer must be chosen. As stated above, if the size of the subregion is too small, it may miss the process optimum, while if too large, it may decrease the algorithm's efficiency in finding the optimum. It is necessary to use some rigorous criterion to choose the optimal size instead of making an arbitrary choice. The histogram of all possible center points can be used as an indicator for the decision of subregion size. Given a center point  $c^*$ , as the subregion size increases, the probability for including the process optimum in the new subregion also increases. The probability for the subregion to include the true optimum with respect to a distance  $r$  from the center is given by

$$\psi(r) = \frac{1}{N} \sum_{j=1}^m \sum_{l=1}^{n_j} I(c^* - r \leq \tilde{c}_{l_j}^{(j)} \leq c^* + r) \quad (15)$$

where  $n_j$  is the total number of optimization steps performed on model  $j$ ,  $m$  is the highest order model that was used,  $N$  is the total number of optimizations (i.e.  $N = \sum_{j=1}^m n_k$ ),  $\tilde{c}_{l_j}^{(j)}$  is the center point calculated using model  $j$  for the  $l^{th}$  optimization, and  $I$  is the indicator function. Then the size of the new subregion,  $r^*$ , is calculated as

$$r^* = \min(r | \psi(r) \geq \alpha) \quad (16)$$

where  $\alpha$  is some confidence level determined by the experimenter. Once the new subregion has been selected, the ACD methodology can be implemented to choose design points in this layer.

#### 6.2.4 Adaptive Combined Design

Experimental designs can take several forms. They can be model based optimal designs such as D-optimal [99], which excels in parameter estimation but must assume some model structure which may be incorrect; or they can be space-filling, model-free designs [56] (such as minimax or Latin hypercube), which can efficiently explore a complex response surface for the process optimum. In order to balance different design goals, previous reports have applied combined criteria that combine experimental designs in order to choose design points for a process. For example, Goel et al. implemented a design where half of the data points were collected using a D-optimal design and the other half were collected using a Latin hypersquare design [106]. Alternatively, Joseph and Hung implemented a constrained design combining D-optimal and T-optimal criterion, termed DT-optimal, where a tuning parameter was introduced to control how the new criterion's characteristics were weighted between D-optimal and T-optimal [139]. The goals of this study were model discrimination and parameter estimation.

In the current work, the goal is to find a process optimum for the sc-CO<sub>2</sub> process when no single validated model is available for the system at the outset. Thus, it would be useful to incorporate both model-dependent and model-free designs. In the ACD methodology proposed here, a new design criterion combining a D-optimal, model-dependent criterion and a minimax, model-free design criterion is applied in a constrained manner; to the best of our knowledge this has not been previously attempted. The D-optimal design minimizes the determinant of the inverse of the information matrix,  $\mathbf{M} = \mathbf{A}^T \mathbf{A}$  [27]:

$$\min |(\mathbf{M})^{-1}| \tag{17}$$

For the model-free design, a minimax design is applied, which seeks to minimize the distance between adjacent design points. Let  $\xi$  be the design of  $N$  points,  $x \in \mathfrak{R}^k$

represent an arbitrary point in the feasible region,  $\tau$  be the Euclidean distance, and  $\rho(x, \xi)$  the distance between  $x$  and its closest design point [137]:

$$\rho(x, \xi) = \min_{x_i \in \mathfrak{R}} \tau(x, x_i) \quad (18)$$

Thus, the minimax design  $\xi^*$  of  $N$  points has a distance

$$\rho^* = \min_{\xi \subset \Omega} \max_{x \in \Omega} \rho(x, \xi) \quad (19)$$

where  $\Omega$  denotes a set of sites. In the combined design, the objective function to be minimized is defined as:

$$\kappa |\mathbf{M}(\xi)^{-1}| + (1 - \kappa)\rho(\xi) \quad (20)$$

where  $0 \leq \kappa \leq 1$  is the pre-specified weighting parameter. The details of applying this criterion are described elsewhere [148]. An important feature of this methodology is the rigorous selection of the weighting parameter,  $\kappa$ , for the next layer. This selection should reflect the uncertainty in the current layer. The  $\kappa$  value in the  $k^{th}$  layer is defined as

$$\kappa = 1 - \frac{\max(0, L_{k-1}^* - d)}{L_0^* - d} \quad (21)$$

where  $L_0^*$  is the evaluation metric with simple mean model  $\hat{y}(\mathbf{x}) = \mu + \epsilon$  and  $L_{k-1}^*$  is the value of the  $L^*$  metric in the previous layer.

### 6.3 *Experimental Methods*

The sc-CO<sub>2</sub> deposition method has been detailed elsewhere (Chapter 5, so only a brief description is offered here. This method was used to decorate a silicon wafer with silver nanoparticles on the surface for application in surface enhanced Raman spectroscopy (SERS). Briefly, a 2 cm × 3 cm size silicon wafer purchased from University Wafer (10–20 Ω·cm, (100), *p*-type) was cleaned in an oxygen plasma for 10 minutes to populate the surface with reactive silanol groups. The substrate was placed in a 30 mL stainless steel reactor along with 50 mg of the silver precursor silver (I) hexafluoroacetylacetonate cyclooctadiene (Ag(hfac)(COD)). The reactor was then charged

Table 10: Results of first layer of experiments

Temperature ( $^{\circ}\text{C}$ )	Mean AgNP size (nm)
60	18.3
60	17.8
90	24.3
120	44.0
120	47.5
150	51.8

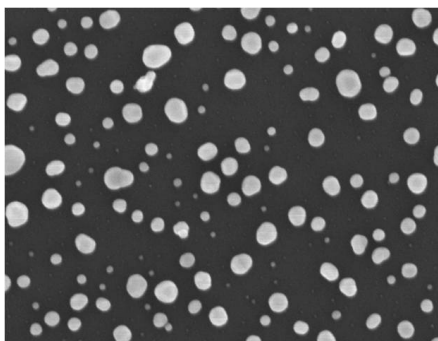


Figure 47: Typical SEM image used for data collection of AgNP size on silicon wafer with 400 psi of hydrogen gas as reducing agent and the final pressure was increased to 1500 psi by introduction of carbon dioxide from a Teledyne ISCO 500HP high pressure pump. Surfaces were characterized using a Zeiss Ultra60 scanning electron microscope operated at 3 mm working distance and 5 kV accelerating voltage. Images were analyzed using the Image Analysis Toolbox in MATLAB R2010a and mean nanoparticle size was calculated based on this automated analysis.

#### ***6.4 Results and Discussion***

For the first layer of experiments the model structure was completely unknown before collecting any data, therefore a space-filling design was used to choose design points for the first layer of experiments. Results of these experiments are given in Table 10. A typical SEM image is shown in Figure 47. The target mean nanoparticle size,  $T$ , was chosen to be  $T = 40$  nm. This value was selected because it was shown to be an optimum nanoparticle size for silver nanoparticles used in SERS,

Table 11: Model selection criteria for first layer

Model order	AIC	$P_B$	CI*( $\mathbf{x}^*$ )	$L^*(\mathbf{x}^*)$
1	35.8	0.59	7.37(100)	8.05(115)
2	37.7	0.41	34.2(128)	38.3(113)

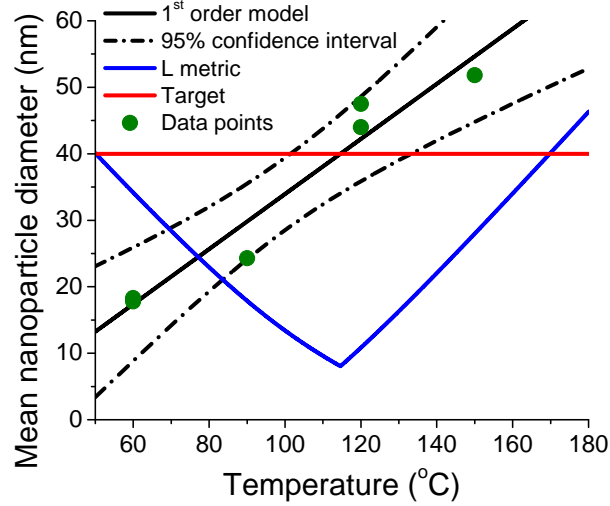


Figure 48: Linear model fit of data collected in the first layer of experiments with 95% confidence interval and the associated L metric

where nanoparticle decorated surfaces function to detect trace amounts of analytes [264]. The SERS performance depends on the nanoparticle size falling within a tight engineering tolerance [264], thus,  $d$  was chosen to be  $d = 5$  nm. Fitting linear and quadratic models to these data, all three metrics (AIC,  $P_B$ , and confidence interval) for model selection indicated that a linear model was the best fit (Table 11). After fitting the linear model, the results of the optimization defined by Eq. 38 yielded an  $L_1^*$  value of  $L_1^* = 8.05$  nm, which was larger than the chosen engineering tolerance of  $d = 5$  nm. Figure 48 shows the linear model, observed data, the uncertainty metric  $L_1$ , the 95% confidence interval, and the target mean particle size as functions of temperature. Since  $L_1^* > d$ , the LoE/ACD algorithm dictates that it is necessary to move to the next layer to conduct more experiments to decrease uncertainty in the model and locate the process optimum. A histogram of center points from both 1<sup>st</sup>

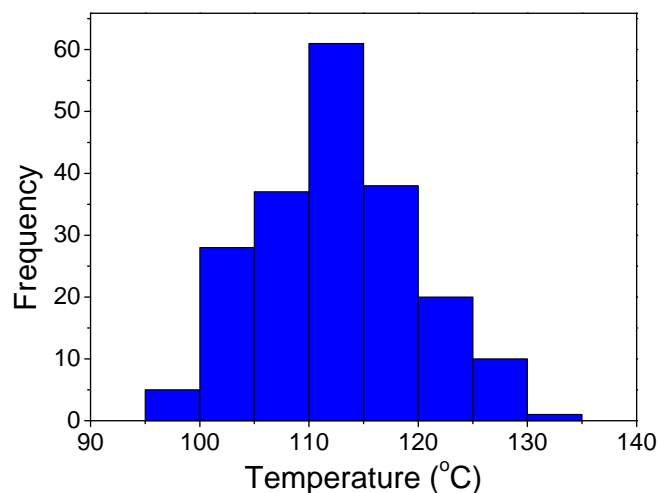


Figure 49: Histogram of center points calculated from bootstrapping and using Eq. 14

Table 12: Results of second layer of experiments

Temperature (°C)	Mean AgNP diameter (nm)
98	32.3
98	29.2
108	34.9
121	41.8
128	42.0
128	49.0

and 2<sup>nd</sup> order models was constructed by the method described in the Methodology section, and  $n_1 = n_2 = 100$  optimizations were carried out to calculate center points for each model type (Figure 49). The mean of the most frequent bin was  $c^* = 113$  °C, which was chosen as the center point for the next subregion. The size of the next subregion was calculated using Eq. 15, and the results are shown in Figure 50. Choosing an  $\alpha$  level of  $\alpha = 0.98$ , the size of the new window is calculated to be  $r^* = 15$  °C (dashed lines in Figure 50). Thus, the next layer is centered at 113°C bounded by [98 °C, 128 °C].

Subsequently, the ACD criterion was applied to choose design points in the next layer. To calculate  $\kappa$ , which is the weighting factor between a minimax ( $\kappa = 0$ ) and

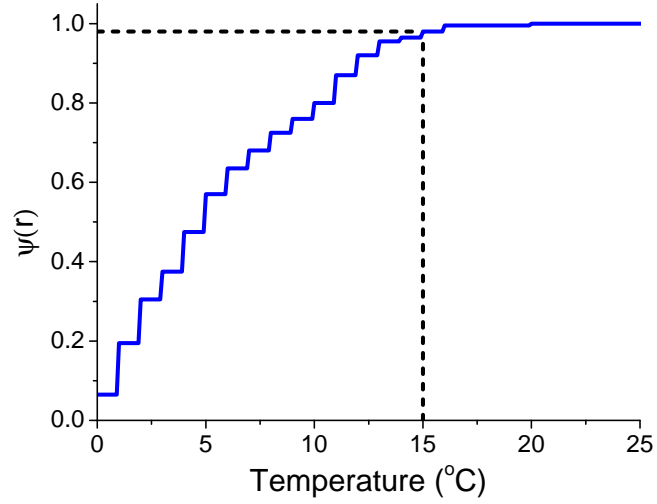


Figure 50: Plot of  $\psi(r)$  versus  $r$  using Eq.15 on the data shown in Figure 49; the horizontal dashed line indicates the  $\alpha = 0.98$  confidence level and the vertical line corresponds to the window size of the next layer for this confidence level

Table 13: Model selection criteria for second layer

Model order	AIC	$P_B$	$CI^*(\mathbf{x}^*)$	$L^*(\mathbf{x}^*)$
1	55.1	0.39	2.83(116)	2.83(117)
2	52.0	0.36	3.12(107)	3.25(113)
3	54.0	0.25	4.18(120)	5.15(113)

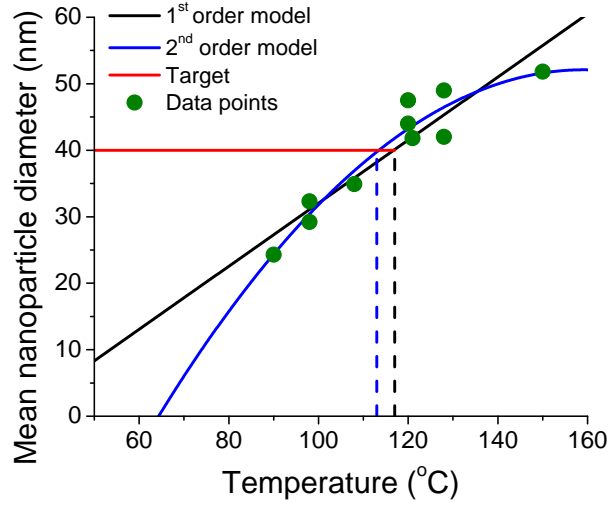


Figure 51: Plot of linear and quadratic models fit in second layer of experiments

D-optimal ( $\kappa = 1$ ) design, Eq. 21 was applied with a linear model for the D-optimal design; this resulted in a  $\kappa$  value of  $\kappa = 0.836$ . Using this  $\kappa$  value, design points for the second layer were calculated. This design and corresponding results are shown in Table 12. The AIC metric for model selection indicated that a quadratic model should be selected to fit these data, while the  $P_B$  and confidence interval metrics indicated that a linear model should be used (Table 13). The optimal value of the performance metric,  $L_2^*$ , for the linear and quadratic models were found to be  $L_2^* = 2.83$  nm and  $L_2^* = 3.25$  nm, respectively. Either value was less than the specified engineering tolerance,  $d = 5$  nm. Since  $L_2^* < d$ , the model uncertainty is acceptable with respect to structural, parameter, and stochastic uncertainty, indicating that the model was sufficient and the algorithm was stopped. It should be noted that the design points at 90 °C, 120 °C, and 150 °C came from the first layer of experiments but are used here in addition to the design points specified from the ACD algorithm since they are the next design points adjacent to the new design region. Linear, quadratic, and cubic models for the data collected in the second layer are shown in Figure 51.

The LoE/ACD sequential experimental design methodology was successful in systematically optimizing the sc-CO<sub>2</sub> process under design region uncertainty, model structure uncertainty, and a tight engineering tolerance specified by the experimenter. While the simple model structures used in this work sufficiently described the system’s behavior, it was not known *a priori* that this would be the case. The simplicity of the resulting models built here does not decrease the significance or utility of the LoE/ACD methodology since it would still be able to capture more complex model behavior if it were present. Furthermore, the evaluation metric falling below the specified engineering tolerance is an indicator that the process is *repeatable*, a significant conclusion despite the fact that the models used were simple. Moreover, the systematic approach of the LoE/ACD methodology was shown to robustly handle uncertainty in the design region by either “zooming in” on the design region that contains the process optimum or “zooming out” if the optimum was missed in the current layer. The ability of the LoE/ACD algorithm to “zoom in” or “zoom out” is vital for studying the *local* behavior of a system near the process optimum; efficiently allocate resources in a reduced, local design region; and meet the engineering tolerance specified by the investigator. In the current study, the LoE/ACD algorithm was able to systematically “zoom in” on the process optimum, decreasing uncertainty in the design region while efficiently allocating resources in the second layer of experiments where the process optimum was found while meeting the specified engineering tolerance. However, the LoE/ACD algorithm could have just as easily “zoomed out” if the original design region chosen did *not* contain the process optimum. Thus, the primary contribution of the LoE/ACD method presented here is the ability to efficiently find the process optimum given a tight engineering tolerance in a minimum of experimental runs despite uncertainty in the design region and a lack of foreknowledge of the sc-CO<sub>2</sub> system’s behavior.

In the first layer of experiments in the present work, six runs were conducted over a

window size [60 °C, 150 °C]. In the second layer, six experiments were conducted over a window size [98 °C, 128 °C]; four of the data points from the first layer were also used in constructing the model at the second layer. Thus, the window size was decreased while yielding a reliable model after conducting only 12 experiments. Furthermore, the model constructed can be used to optimize silver nanoparticle deposition for the conditions used in the sc-CO<sub>2</sub> process over the range [90 °C to 150 °C] if different mean nanoparticle sizes are desired for other applications. A linear model best described the dependence of mean silver nanoparticle size on temperature in the first layer (Table 10 and Figure 48). In the second layer, the AIC indicated that a quadratic model was the best fit for the data while the  $P_B$  and confidence interval suggested that a linear model was the best fit (Table 11). When the linear, quadratic, and cubic models are plotted along with the data, all three fit the data well (Figure 51). Indeed, the evaluation metrics for both the linear ( $L_2^* = 2.83$  nm) and quadratic ( $L_2^* = 3.25$  nm) models were less than the desired engineering tolerance ( $d = 5$  nm). This is an instance where engineering knowledge of the system is useful in model selection. If it is hypothesized that nanoparticle size increases monotonically with temperature in this system, the linear model may be the better choice. Alternatively, if it is hypothesized that the nanoparticle size will reach some type of limit as temperature increases, a quadratic model may be better, although this would necessitate further experiments above 150 °C in this system to validate this model, an unnecessary step if the model is to be refined only near the process optimum. The AIC,  $P_B$ , and  $CI(\mathbf{x})$  values all indicated that the cubic model would be a poor choice and yield an evaluation metric  $L_2^* = 5.15$  nm which was greater than the engineering tolerance and  $d = 5$  nm.

In the first layer of experiments, a space-filling design was applied since there was no foreknowledge of what the underlying model structure would be. In the second layer, the ACD methodology was applied to balance the experimental design between minimax and D-optimal. The weighting value  $\kappa$  between these two values

was  $\kappa = 0.836$ , which indicates that the design applied was weighted toward a D-optimal design. This reflects the fact that the model built in the first layer yielded an uncertainty metric  $L_1^* = 8.05$  nm which was relatively close to the engineering tolerance specified by the experimenters from the start ( $d = 5$  nm). If the model constructed in the first layer yielded a larger  $L_1^*$  value, implying more uncertainty in the model structure and parameters, the ACD methodology would have dictated a weighting toward a minimax design in order to “spread out” design points and explore the design space more thoroughly. For example, if  $L_1^*$  were instead  $L_1^* = 20$  nm, the resulting  $\kappa$  value would have been  $\kappa = 0.194$ , yielding a design more heavily weighted toward the minimax design in Eq. 20, reflecting a higher degree of model uncertainty; the selection of the  $\kappa$  parameter is another example of how the LoE/ACD methodology can simultaneously handle both design region and model uncertainty.

The experimental design in the second layer, bounded by [98 °C, 128 °C], was [98 °C, 98 °C, 108 °C, 121 °C, 128 °C, 128 °C]. The design points placed at the boundaries of the second layer reflect the D-optimal design employed in the ACD technique; if a purely D-optimal design were implemented, the design points would have been only at the boundaries of the design region (108 °C and 128 °C) because a linear model was used to make the D-optimal design of the second layer. Instead, the points at 108 °C and 121 °C reflect the minimax design employed in the ACD and are important to further explore points around the process optimum. Consequently, the ACD methodology successfully balanced the opposing design goals of design space exploration using the space-filling, minimax design and parameter estimation using the model-dependent, D-optimal design. In addition, it was noted that three data points from the first layer were incorporated into the model construction in the second layer. However, the ACD algorithm did not take these points into account when constructing the design for the second layer, a consideration that may improve the ACD methodology in future studies.

## 6.5 Conclusion

A novel sequential experimental design methodology, termed Layers of Experiment with Adaptive Combined Design, was implemented to study an elevated pressure, elevated temperature carbon dioxide nanoparticle deposition process. It was shown that the LoE/ACD algorithm was able to robustly study and optimize the sc-CO<sub>2</sub> system under significant uncertainty in the design region and model structure in addition to a tight engineering tolerance. The LoE component of this technique decreased the design space to be explored from [60 °C, 150 °C] to [98 °C, 128 °C] while increasing reliability in the model built around the target nanoparticle size,  $T = 40$  nm. The ACD component of this technique balanced the design goals between a space-filling, minimax experimental design that explores the design space around the process optimum and a model-based, D-optimal design that seeks to improve the model structure. Conducting only 12 experiments in two layers, the LoE/ACD approach was able to rapidly find the process optimum for this system and yield models that can be used with confidence in statistical inference for this advanced technology process.

In Chapter 7, the LoE/ACD methodology is implemented to optimize the sc-CO<sub>2</sub> deposition system for a mean AgNP size of  $T = 20$  nm. The efforts outlined in Chapter 7 highlight the ability of the LoE/ACD methodology to zoom out and zoom in on regions where the process optimum is located.

## CHAPTER VII

### A SECOND CASE STUDY FOR LAYERS OF EXPERIMENT WITH ADAPTIVE COMBINED DESIGN

#### *7.1 Introduction*

In this chapter, the LoE/ACD methodology developed in Chapter 6 is applied to optimize the AgNP deposition process for a target AgNP size of  $T = 20$  nm. This LoE/ACD algorithm was able to find the process optimum for a nanoparticle deposition process using the CO<sub>2</sub>-assisted process by conducting eight experiments in two layers. In the first layer, the target mean nanoparticle size was not achieved, exemplifying uncertainty in design region for this process. Consequently, the LoE/ACD algorithm redirected the second layer of experiments to a new design region, resulting in the successful optimization of the process at 69 °C.

#### *7.2 Experimental Methods*

##### **7.2.1 Layers of Experiments with Adaptive Combined Design**

The LoE/ACD algorithm begins by conducting a set of experiments and collecting data. Then, a model (empirical or otherwise) is chosen and the model is fit using the experimental data. Next, the accuracy of the predictions made by the model is assessed. If the accuracy is within the engineering tolerance set by the experimenter, the model is deemed acceptable and used to optimize the process. If not, the next subregion for experiments is selected using the LoE technique, design points are chosen using the ACD methodology, and the algorithm iterates until the accuracy of the model falls within the engineering tolerance set by the experimenter. Each of these steps is detailed below.

### 7.2.1.1 Model selection

Polynomial models for data were selected using the Akaike information criterion (AIC) and Bayesian probability ( $P_B$ ). Methods for calculating these metrics are given elsewhere [38, 266].

### 7.2.1.2 Assessment of model accuracy

A target size  $T = 20$  nm and an engineering tolerance  $d = 5$  nm were chosen with surface enhanced Raman spectroscopy (SERS) as the motivating application [264]. The evaluation metric,  $L$ , is implemented to assess the model accuracy and is defined as [148]:

$$L = \max\{|T - (\hat{y}(\mathbf{x}) + CI(\mathbf{x}))|, |T - (\hat{y}(\mathbf{x}) - CI(\mathbf{x}))|\} \quad (22)$$

where  $\hat{y}(\mathbf{x})$  is the fitted model and  $CI(\mathbf{x})$  is the confidence on the model prediction. If  $L > d$ , the LoE algorithm specifies that a new layer with additional experiments is necessary. If  $L \leq d$ , the model is sufficiently accurate and the LoE/ACD algorithm stops.

### 7.2.1.3 Selection of next layer

The next step in the LoE algorithm is choosing the location and size of the next layer (subregion). To choose the center of the next layer, the optimization problem

$$\min_x |T - \hat{y}(\mathbf{x})| \quad (23)$$

is solved  $n_j$  times for each candidate model  $j$  by calculating residuals of the model  $\hat{y}(\mathbf{x})$  and experimental responses  $y(\mathbf{x})$ , randomly resampling (bootstrapping) these residuals to formulate synthetic response variables, fitting each candidate model to these synthetic responses, and solving Equation 23. A histogram of the center points calculated from each optimization of each candidate model,  $\tilde{c}_{lj}$ , is created; the mean of the most frequent bin in the histogram is chosen as the center point for the next layer,  $c^*$ . To choose the size of the next layer, the histogram of potential center points

is used: as the size of the subregion increases, the probability for the subregion to include the true optimum with respect to a distance  $r$  from the center is given by [148]:

$$\psi(r) = \frac{1}{N} \sum_{j=1}^m \sum_{l=1}^{n_j} I(c^* - r \leq \tilde{c}_{lj} \leq c^* + r) \quad (24)$$

where  $N$  is the total number of optimizations performed (i.e.,  $N = \sum_{j=1}^m n_j$ ) and is the number of candidate models used in the optimization routine.

#### 7.2.1.4 Adaptive combined design

A combined design methodology is implemented to choose design points in the layers used in the LoE/ACD methodology. This combined design uses a constrained approach to weight and optimize the design based on two criteria: one for a model free, minimax design, and one for a model dependent, D-optimal design. Let  $\xi$  be the design of  $N$  design points; then we define  $\rho(\xi)$  as the metric to be minimized that yields a design minimizing the maximum distance between adjacent design points. A D-optimal design seeks to minimize the determinant of the inverse of the information matrix for the most probable model, that is,  $|\mathbf{M}(\xi)^{-1}|$ . Thus, the weighted combined design metric to be optimized is [148]:

$$\kappa |\mathbf{M}(\xi)^{-1}| + (1 - \kappa)\rho(\xi) \quad (25)$$

where  $0 \leq \kappa \leq 1$  is the weighting factor between these two design metrics. The parameter  $\kappa$  is calculated as:

$$\kappa = 1 - \frac{\max\{0, L_{t-1}^* - d\}}{L_0^* - d} \quad (26)$$

where  $L_{t-1}^*$  is the  $L^*$  metric from the previous layer and  $L_0^*$  is the  $L$  metric calculated fitting a simple mean model  $\hat{y}(\mathbf{x}) = \mu + \epsilon$ .

## 7.2.2 Experimental procedure

The silver nanoparticle deposition method by elevated pressure, elevated temperature CO<sub>2</sub> has been detailed elsewhere (Chapter 5), so only a brief description is presented

Table 14: Results of experiments and model selection criteria in first layer

Temperature ( $^{\circ}\text{C}$ )	Mean AgNP size (nm)	Model order	AIC	$P_B$
120	44	1	26.1	0.59
130	41.6	2	28.1	0.41
140	55.2			
150	51.8			

here. A 2 cm x 3 cm silicon wafer ((100),  $p$ -type, 10–20  $\Omega$  cm) was purchased from University Wafer and cleaned in an oxygen plasma to populate the surface with reactive silanol groups. The substrate was loaded into a stainless steel high pressure reactor with the organometallic precursor, silver hexafluoroacetylacetonate cyclooctadiene, hydrogen as reducing agent, and carbon dioxide. The reaction was run at 103 bar at the specified temperature. Products were characterized by a Zeiss Ultra60 scanning electron microscope (SEM), and mean nanoparticle sizes were extracted from SEM images using automated image analysis in MATLAB 2010a.

### 7.3 Results and Discussion

#### 7.3.1 First layer

A space-filling experimental design was chosen for the first layer of experiments in the region [120  $^{\circ}\text{C}$ , 150  $^{\circ}\text{C}$ ]. Results from these experiments are shown in Table 14. The AIC and  $P_B$  indicated that a linear model was the best fit for the data. Using a linear model, the  $L^*$  metric was calculated to be  $L^* = 38.8$  nm at  $x^* = 130$   $^{\circ}\text{C}$  (Figure 52). Since  $L > d$ , the LoE/ACD algorithm dictated that another experimental layer was necessary to optimize the process.

#### 7.3.2 Second layer

The center and size of the next subregion were calculated using the procedures described above. The histogram of center points is shown in Figure 53a; the mean of the most frequent histogram was  $c^* = 63$   $^{\circ}\text{C}$ , which was chosen as the center of the next

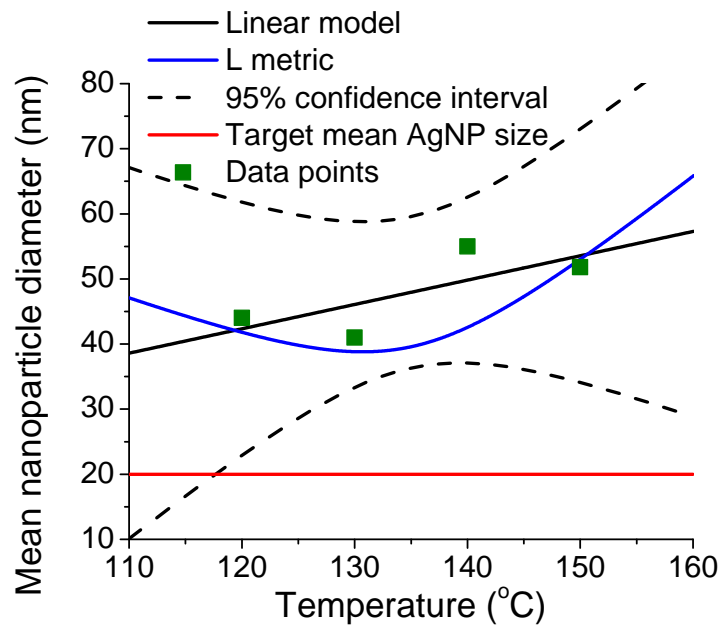


Figure 52: Linear model fit of data collected in first LoE with 95% confidence intervals and  $L$  metric

Table 15: Results of experiments and model selection criteria in second layer

Temperature (°C)	Mean AgNP size (nm)	Model order	AIC	$P_B$
44	12.1	1	39.9	0.54
56	17.3	2	40.3	0.46
69	19.2			
82	24.1			

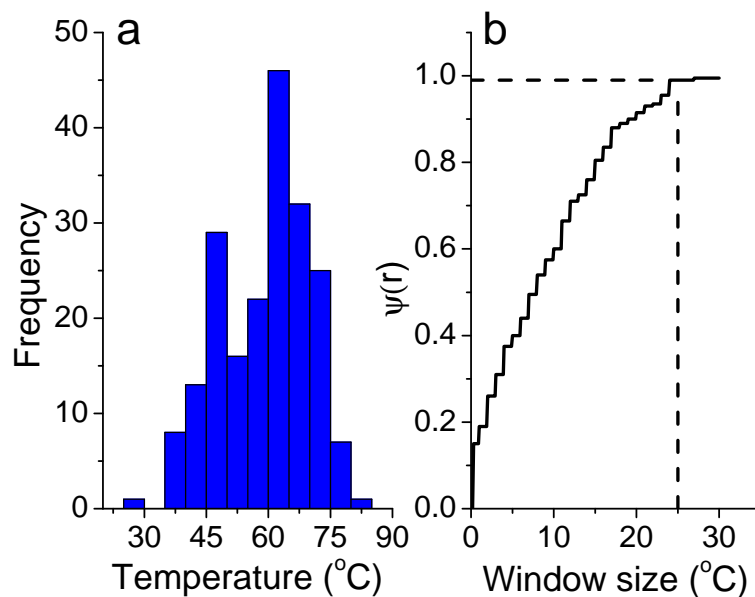


Figure 53: (a) Histogram of potential center points (b)  $\psi(r)$  vs.  $r$ ; dashed lines indicate 99% confidence level and window size

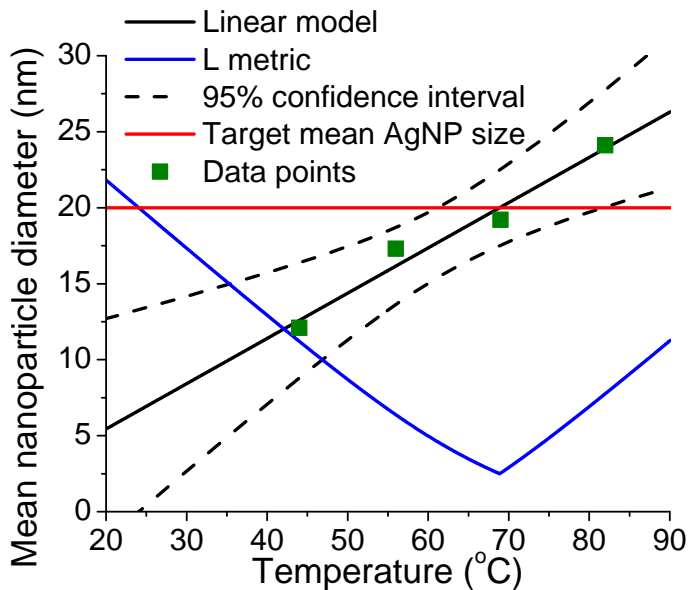


Figure 54: Linear model fit of data collected in second LoE with 95% confidence interval and  $L$  metric

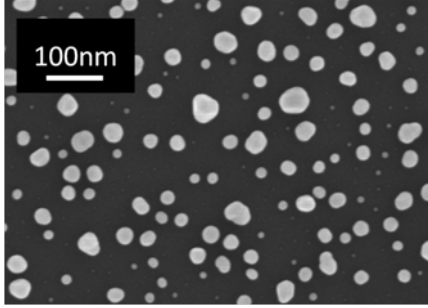


Figure 55: Typical SEM image of silver nanoparticles on silicon wafer surface

region. The size of the next window was chosen using Equation 24 to be  $25^\circ\text{C}$ , corresponding to a  $\psi$  level chosen to be  $\psi = 0.99$  in Figure 53b so that there is a higher degree of confidence that the optimum lies in the design region than confidence in the model prediction (with confidence interval of 95%). The value for  $\kappa$  was calculated to be  $\kappa = 0.01$  from Equation 26; using this value in the ACD algorithm resulted in an experimental design that is essentially minimax due to the weighting. Results from this design are given in Table 15; the AIC and  $P_B$  metrics indicated a linear model should be fit to the data in this window. Using this model,  $L^*$  was calculated to be  $L^* = 2.49$  nm. Since  $L^* \leq d$ , the model was sufficiently accurate to within engineering tolerance and accepted; the plot of this model is shown in Figure 54, along with the 95% confidence interval and the  $L$  metric. Figure 55 shows a typical SEM image with silver nanoparticles deposited on a silicon wafer surface.

The goal of the LoE/ACD methodology was to rapidly and systematically optimize the sc-CO<sub>2</sub> AgNP deposition process under uncertainty in model structure, design space, and an engineering tolerance requirement on the mean AgNP size,  $T = 20$  nm. The investigators chose the design region [ $120^\circ\text{C}$ ,  $150^\circ\text{C}$ ] as the initial layer in which to conduct experiments; however, results indicated that this was a poor choice for the chosen target. This is an example of how uncertainty in the design region for a system can affect process optimization. Nonetheless, the LoE/ACD algorithm was able to efficiently redirect the second layer of experiments to a region that was likely

to contain the process optimum. However, due to the uncertainty in model structure from the previous layer of experiments (i.e. the relatively large  $L^*$  value in the first layer), the weighting parameter between the minimax design and D-optimal design was weighted significantly toward the minimax design in the ACD algorithm. This is because a space-filling design like a minimax design is model free, so it will not suffer bias from a poor model choice in constructing an experimental design; consequently, the design points chosen for the second layer were well “spread out” in order to locate the process optimum.

The results of these experiments indicated that the process optimum did indeed fall within the design region explored in the second layer. Furthermore, the small  $L^*$  metric ( $L^* = 2.49$  nm) indicated that the linear model structure selected for the specified target in this region was acceptable. If a further layer of experiments were to be conducted, the weighting factor  $\kappa$  would be  $\kappa = 1$ , weighted completely toward the D-optimal design since there is a higher degree of confidence in the linear model in this region of the design space. These experiments based on the model dependent D-optimal design would refine the model parameters. Last, the method can be generalized to multiple independent variables (such as pressure or reaction time).

## **7.4 Conclusion**

The LoE/ACD methodology was implemented to optimize a silver nanoparticle deposition process under structural uncertainty, design region uncertainty, and an engineering tolerance requirement. After eight experiments conducted in two sequential layers, the algorithm found the process optimum at  $T = 69$  °C for a target mean nanoparticle size of  $d = 20$  nm with a tolerance of  $d = 5$  nm.

In the next chapter of this thesis, an initial experimental design methodology is developed for planning the first round of experiments for a system that is expensive

to study (in terms of time and money), not well understood, and related to a similar, non-identical system. This methodology is implemented to plan the first round of experiments for iridium nanoparticle deposition in sc-CO<sub>2</sub> based on prior data for the AgNP deposition system in sc-CO<sub>2</sub> as well as expert conjecture.

## CHAPTER VIII

# INITIAL EXPERIMENTAL DESIGN INCORPORATING PRIOR DATA, ENGINEERING MODELS, AND EXPERT OPINION

### *8.1 Introduction*

In the final chapter of this thesis, an initial experimental design methodology is developed and implemented to plan the first round of experiments for a system that is expensive and time-consuming to study, not well understood, and is related to (but non-identical to) another system.

The methodology termed design of experiments (DoE) encompasses many statistical approaches that seek to study the behavior of a system where variation is present [30, 193, 243]. For example, factorial designs are implemented to study behavior in a system where multiple independent variables can influence behavior and it is unclear which variables have the most effect on the system output [30, 190]. The factorial design approach seeks to separate the main effects (due to a single independent variable) and interaction effects (due to the influence of multiple independent variables) that can influence the system output, and a polynomial model is then developed to predict the future output of the system and/or optimize the system [61, 295, 319].

A vital factor to consider when implementing any DoE approach is how to choose which experiments to run within the design space. If a system is expensive to study in terms of time and money, running many experiments within the design space to find the process optimum is infeasible and undesirable. For instance, many advanced technology processes, such as nanofabrication methods in nanotechnology, cannot be evaluated cost effectively via many experiments due to expenses associated with

running experiments (e.g., energy and capital costs) and/or product characterization (e.g., costs associated with electron microscopy and/or device fabrication) [120, 150, 175].

Furthermore, it is often the case that a new process in nanotechnology to be optimized may be similar but non-identical to a previously studied, older process. A purely statistical approach to designing experiments on the new process would implement a space-filling design. The most straightforward of these is a uniform design, where the design points are placed the same distance away from one another [87]. A Latin hypercube approach is also applicable to fill a design space when a model is not known for a system [265]. However, since the space-filling design will fill the entire design space selected by the investigator, some experiments may be a waste of resources if far from the process optimum. Moreover, if there are multiple process inputs that must be optimized, the multidimensional space-filling would likely dictate an infeasible number of experiments. Last, any domain knowledge that may exist for the older, related system is not used when designing experiments, losing an important advantage for judiciously selecting design points.

On the other hand, it is possible to rely solely on specific domain knowledge of the system to guide the experimental design, avoiding the use of a traditional DoE approach. A domain-knowledge oriented approach may focus more on areas of interest to the investigator compared to a purely statistical approach. However, it is possible that the selection of the design space is incorrect, or that the domain knowledge is incomplete and insufficient to effectively guide the experimental design. Thus, resources would be wasted and the process optimum may never be found using only domain knowledge.

Consequently, choosing a purely statistical or a purely domain knowledge-oriented approach to selecting design points for a new system may lead to inefficiencies and

wasted resources while attempting to find the process optimum in the initial experimental design. In order to overcome this challenge, Vastola developed a novel methodology, termed here Initial Experimental Design (IED), that is a hybrid of statistical and domain knowledge-based approaches for designing experiments for a new system when a related, older system exists [291]. Previous approaches have been used to combine data from multiple sources, such as experimental data and expert opinion, in selecting an experimental design [121, 138, 144, 234]. The contribution of the current IED approach is that it synthesizes expert opinion, statistical experimental design, prior data on a non-identical system, and engineering models for choosing the initial design region for the new system.

As a demonstration of the potential utility of the IED approach, Vastola examined data from a study by Zong and Watkins for the supercritical carbon dioxide-mediated synthesis of copper thin films on silicon [291, 335]. Vastola analyzed data relating thin film growth rate,  $R$ , as a function of precursor concentration,  $[P]$ , in the work of Zong and Watkins as prior data in the IED methodology [291]. While data for  $R$  vs. hydrogen concentration,  $[H_2]$ , was reported by Zong and Watkins as well, Vastola treated this data as “unknown” and implemented the IED approach to design experiments for studying  $R$  as a function of  $[H_2]$  [291]. The investigators incorporated the prior data of  $R$  vs.  $[P]$  with hypothetical expert opinion while implementing the IED methodology to generate a combined model that was used in selecting design points for studying the variation of  $R$  with hydrogen concentration. This work resulted in an initial design for studying the dependence of  $R$  on  $[H_2]$  that balanced a space-filling, maximin design (reflecting uncertainty in the design space) with an objective-oriented optimization design (reflecting prior data and expert conjecture for the system). While this application by Vastola showed the potential use of the IED methodology, it was not applied to guide actual experiments conducted in the laboratory and thus could not be fully validated [291].

In the present work, we apply the approach developed by Vastola to select the initial experimental design points in the deposition of iridium nanoparticles (IrNP) from an organometallic precursor, iridium (I) hexafluoroacetylacetonate cyclooctadiene (Ir(hfac)(COD)), on a Si wafer surface [291]. This study also makes original contributions to Vastola’s approach by using a survey instrument to elicit expert responses, resolving conflicts between expert opinions, and using a local model approach to select experiments in the subsequent experimental design layer. The previous data and system for the current study come from the work of Casciato et al., where silver nanoparticles were deposited on a silicon wafer substrate [43, 44]. Thus, the main difference between the two systems is the selection of precursor: Ir(hfac)(COD) for the “new” system and Ag(hfac)(COD) for the “old” system. The new model system using Ir(hfac)(COD) was chosen because it is costly to study in terms of time and money and also has not been extensively studied in previous work using sc-CO<sub>2</sub> deposition techniques: this precursor has been used in limited cases for Ir deposition in vacuum-based chemical vapor deposition techniques [316, 317]. In the current work, IrNPs with a mean size of 40 nm and within a tolerance of 5 nm were targeted for deposition since iridium nanoparticles have application in catalysis and biosensors, and the size of the particles is often important for optimal function [98, 128, 326]. Expert opinions were elicited from four investigators, each of whom has more than ten years of experience in the area of nanomaterials synthesis, via a survey instrument that was distributed via e-mail.

The results of the present study show that the IED methodology was able to successfully plan experiments near the predicted optimum based on the experts’ conjectures. However, two morphologies were observed for the deposited IrNPs. In one morphology, the particles were small (nanoscale) and discrete. For these particles, the target mean size of 40 nm was achieved, and an Arrhenius model was fit to the data. However, the tolerance on the model predictions did not fall within the 5

nm engineering tolerance set by the investigators, so additional experiments would be necessary to refine the Arrhenius model to meet this tolerance. In the second morphology, the particles were large (near microscale) and agglomerated. A discussion of the performance of the IED methodology along with the obtained results is presented.

## **8.2 Methodology**

### **8.2.1 Summary of the IED methodology**

Vastola gives a thorough treatment of the IED methodology that is applied in this work [291]. Thus, a summary is presented of the steps taken to implement the IED methodology as it was applied to the current system (deposition of Ir nanoparticles) based on data from the old system (deposition of Ag nanoparticles) given expert opinion and engineering models. These steps are:

1. Choose a location and size for the design window based on experts' responses and confidences
2. Build individual models based on each expert's responses and respective confidences
3. Build a unified model based on the individual models and the experts' respective confidences in the individual models
4. Choose experimental design points based on the unified model, balancing between space-filling and objective-oriented designs

### **8.2.2 Survey for expert conjecture**

A short survey was developed to elicit responses from experts in the field of nanomaterials synthesis for the deposition of IrNP in sc-CO<sub>2</sub> based on prior data for AgNP deposition in sc-CO<sub>2</sub>. Approval of the Georgia Institute of Technology's Institutional

Review Board (IRB) was obtained prior to distributing the surveys via e-mail. The survey instrument used is available in Appendix B. In the prior work on AgNP deposition, the range of deposition was [60 °C, 150 °C], and Casciato et al. implemented an Arrhenius model to describe the mean nanoparticle size,  $\bar{y}$ , as a function of temperature:

$$\ln(\bar{y}) = \beta_0 - \frac{E_a}{RT} \quad (27)$$

where  $\beta_0$  is a fitting parameter related to the pre-exponential factor in the Arrhenius equation,  $R$  is the ideal gas constant, and  $E_a$  is the effective activation energy [43, 44]. The Arrhenius plot included in the survey and based on data from Casciato et al. is shown in Figure 56, along with the estimated values for  $\beta_0$  and  $E_a$ . Given this

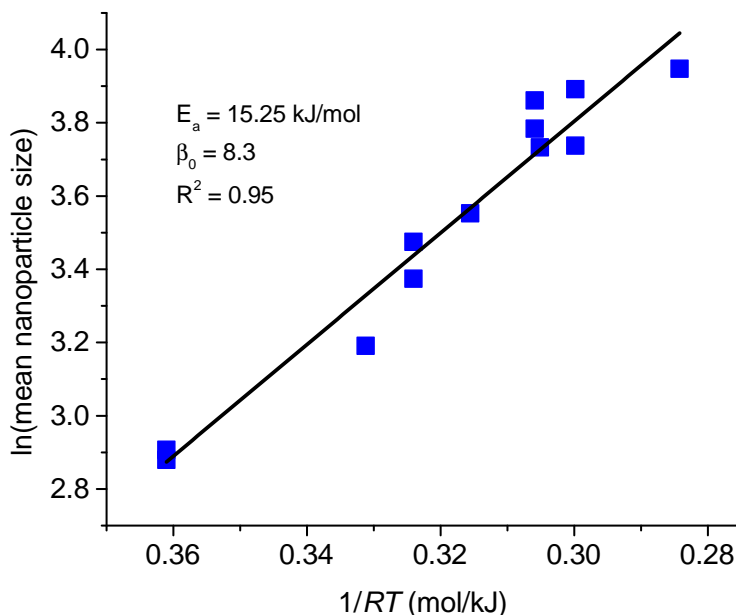


Figure 56: Arrhenius plot of prior data from AgNP deposition experiments in sc-CO<sub>2</sub> [43, 44]

information, experts were asked for their best conjectures for the following:

1. Location and size of the design region and confidence in this conjecture

2. Values of the parameters in the Arrhenius equation ( $\beta_0$  and  $E_a$ ) and confidence in these conjectures
3. Confidence that the IrNP system can be modeled using the Arrhenius equation

Experts reported confidence on a scale of 0–10, with 0 denoting a complete guess in the conjecture and 10 denoting absolute certainty in the conjecture. For the model parameters, experts were asked directly for their conjectures about  $E_a$  but indirectly for their conjectures of  $\beta_0$ . This was done by asking the experts for their conjecture of the mean IrNP size in the center of their chosen design space and extrapolating their resulting individual model to its  $y$ -intercept. Each of these conjectures is used in the following sections that are concerned with choosing the design window, building the individual models, building the unified model, and choosing the experimental design.

### 8.2.3 Choosing the experimental design window

The first step in the IED methodology is selecting the size and location of the experimental design window. Since the chemical and physical properties of the precursors used in the previous system and current system are different, it is likely that the temperature ranges for nanoparticle deposition from the Ag and Ir precursors are different. Thus, experts were asked to give their conjectures for the lower bound (LB) and upper bound (UB) on the design window for the current system, in the form of a 95% confidence interval for both the LB and UB. The experts were also asked to rate their confidence in this conjecture with a single value on a scale from 0–10. This approach synthesizes the experts' knowledge in choosing the region for the design window and resolves potential conflicts in the experts' opinions given via the survey.

The unified design window based on all experts' responses was determined by using the reported confidence as a weight on the smallest value in the LB and largest value in the UB. Thus, if Expert  $i$ 's responses were of the form  $[a_i, b_i]$  for the 95% confidence interval of the LB and  $[c_i, d_i]$  for the 95% confidence interval of the UB,

then the unified lower bound,  $LB_U$ , based on all experts' responses would be calculated as:

$$LB_U = \sum_{i=1}^n \frac{u_i^D a_i}{\sum_{j=1}^n u_j^D} \quad (28)$$

where  $u_i^D$  is the confidence of expert  $i$  in this conjecture about the design region and  $n$  is the number of experts surveyed. The same approach is implemented to calculate the unified upper bound, using  $d_i$  in the summation instead of  $a_i$ . The individual models are then built over this design window, as detailed in the next section.

#### 8.2.4 Building individual models based on expert opinion and prior data

The next step in the IED methodology is to develop individual models based on each expert's responses for the conjectured model parameters as well as prior data from the previous system. A summary of the approach Vastola proposed is provided here as it is applied to this work [291].

The response data for the old system,  $\tilde{\mathbf{Y}}$ , was updated to that of the new system,  $\mathbf{Y}$ . This was achieved using the difference between the Arrhenius model predictions for the old system,  $g(\mathbf{X}, \tilde{\beta})$ , and that of the current system,  $g(\mathbf{X}, \beta)$ , in the updated design window given by each expert,  $\mathbf{X}$ . The updated response data is then:

$$\mathbf{Y} = \tilde{\mathbf{Y}} + (g(\mathbf{X}, \tilde{\beta}) - g(\mathbf{X}, \beta)) \quad (29)$$

where  $\tilde{\beta}$  are the parameters for the old system and  $\beta$  are the conjectured parameters for the new system, taken from the midpoint of the expert's conjecture. A model based on each individual expert's conjectures and the prior data could then be fit to this *pseudo-data*. However, it is unlikely that the values for  $\beta$  and  $\mathbf{X}$  are known exactly, and this misspecification may be significant and should not be ignored. Consequently, the 95% confidence intervals specified by the experts for the design region lower bound, design region upper bound,  $\beta_0$ , and  $E_a$  were used to add variance terms to the models. Similarly, the model for the new system may be misspecified; an additional variance term is added to  $g(\mathbf{X}, \beta)$  to account for this uncertainty. Introducing these variance

terms to the model makes it a hierarchical Bayes model [63, 104]. This step increases the model’s utility by assuming it is not possible to precisely know the conjectured design region and parameters. With these variance terms included in the Bayesian hierarchical model, the model is then simulated using Gibbs sampling. The result is an Arrhenius model with updated parameters based on the conjectures of each expert and the prior data for the AgNP system. These models are then unified via weighting, as detailed in the next section. For an in-depth treatment of the implementation of this hierarchical model, see Vastola [291].

### 8.2.5 Building a unified model

The unified model is built using the experts’ confidence (on the 0–10 scale) in the conjectured design window, conjectured parameters, and confidence that the Arrhenius model structure is correct. Each confidence is considered a probability ( $p(\textit{Design})$ ,  $p(\textit{Parameters})$ , and  $p(\textit{Structure})$ , respectively) that the conjecture is correct, and these independent probabilities are multiplied together to calculate the total trust each expert has in his or her individual model,  $\hat{u}_i(\mathbf{x})$ :

$$\hat{u}_i(\mathbf{x}) = p(\textit{Design}) \times p(\textit{Parameters}) \times p(\textit{Structure}) \quad (30)$$

Then the weight given to expert  $i$ ’s opinion (i.e., the normalized trust) is denoted as:

$$w_i(\mathbf{x}) = \frac{\hat{u}_i(\mathbf{x})}{\sum_{i=1}^n \hat{u}_i(\mathbf{x})}. \quad (31)$$

The unified model,  $\mathbf{Y}(\mathbf{x})$ , is then defined as

$$\mathbf{Y}(\mathbf{x}) = \sum_{i=1}^n w_i(\mathbf{x}) \mathbf{Y}_i(\mathbf{x}). \quad (32)$$

where  $\mathbf{Y}_i(\mathbf{x})$  is expert  $i$ ’s individual model. Using the experts’ confidences for weighting these models is another contribution of the present work. This unified model is then used to simulate predictions for use in selecting the experimental design points in the design window; results are presented in the next section.

### 8.2.6 Choosing the experimental design points

A minimum energy design (MED) is used to choose the experimental points within the design window [64]. The concept of the MED can be understood through a simple example. Consider  $n$  positively charged particles: if they are all placed into a box, they will spread out in such a way to minimize the energy of the system of particles. The analogy to the experimental design is that the location of the particles represents the design points and the design window is the box where the particles are placed. As charge increases for a design point, the nearest design points are pushed farther away, and vice versa. The total potential energy for this type of experimental design is

$$E_n = \sum_{i=1}^{m-1} \sum_{j=i+1}^m \frac{q(\mathbf{x}_i)q(\mathbf{x}_j)}{d(\mathbf{x}_i, \mathbf{x}_j)} \quad (33)$$

where  $m$  is the total number of experimental design points,  $d$  is the Euclidean distance between design points, and  $q$  is the charge of design point  $x_i$ . Vastola defined this charge function so that an expert's confidence in the individual model and how close the model comes to the target nanoparticle size,  $T_{NP}$ , both influence the charge and subsequently the experimental design [291]. The probability that the model response at a point  $x$  is within a tolerance  $d$  of the target size,  $T_{NP}$ , is defined as

$$p(\mathbf{x}) \equiv \mathcal{P}(T_{NP} - d \leq Y^*(\mathbf{x}) \leq T_{NP} + d), \quad (34)$$

Thus, the charge at any point  $\mathbf{x}_i$  is defined as

$$q(\mathbf{x}_i) = (1 - f(p(\mathbf{x}_i), \mathbf{u}(\mathbf{x}_i)))^\gamma \quad (35)$$

where  $\mathbf{u}(\mathbf{x}_i)$  is the vector with the  $j$ -th position possessing the trust level in model  $j$  at the design point  $\mathbf{x}_i$ ,  $\gamma$  is a tuning parameter set by the investigator. The function  $f$  was defined by Vastola as [291]:

$$f(p(\mathbf{x}_i), \mathbf{u}(\mathbf{x}_i)) = \tilde{p}(\mathbf{x}_i) + \text{sgn}(m - \tilde{p}(\mathbf{x}_i)) (m - m\hat{u}(\mathbf{x}_i)) \left| \frac{\tilde{p}(\mathbf{x})}{m} - 1 \right| \quad (36)$$

The function  $f$  is defined as in Eq. 36 because it gives the overall charge function  $q$  several properties that make it well-suited to balancing the statistical and experimental design goals described above [291]. The tuning parameter  $\gamma$  was shown to balance a space-filling maximin design (for  $\gamma$  approaching zero) with an objective-oriented design that focuses design points around the process optimum (for large  $\gamma$ ). It was also shown that the magnitude of  $\gamma$  that gives the objective-oriented design depends on the particular system and process under study, so absolute values for  $\gamma$  are not meaningful comparing across systems.

After the charge function  $q$  was defined, a modified Fedorov exchange algorithm was applied to minimize Eq. 33 in the MED [89]. This algorithm iteratively tests designs in the search region; if the next design tested decreases  $E_n$ , the design is kept until updated by a future design that decreases  $E_n$  even further, until a minimum is reached.

### ***8.3 Experimental Methods***

#### **8.3.1 Materials**

Carbon dioxide gas (99.99%) and hydrogen gas (99.99%) were purchased from Airgas. The organometallic precursor iridium hexafluoroacetylacetonate cyclooctadiene (Iridium(hfac)(COD)), methanol, acetone, and isopropyl alcohol were purchased from Sigma Aldrich and used as received. Test silicon wafers ( $p$ -type, 10–20  $\Omega\cdot\text{cm}$ , (100)) were purchased from University Wafer. The substrates were cut into 2 cm x 3 cm pieces and rinsed with methanol, acetone, and isopropyl alcohol sequentially, then dried under a gentle stream of  $\text{N}_2$ . Substrates were subjected to 10 minutes of cleaning in an oxygen plasma in a Harrick PDC-32G Plasma Cleaner.

#### **8.3.2 Nanoparticle deposition**

In order to deposit IrNPs on the substrates under study,  $50 \pm 0.1$  mg of the Ir(hfac)(COD) precursor was loaded into a 30 mL hot wall stainless steel reactor along with

the substrate. The reactor was initially pressurized by  $400 \pm 10$  psi of hydrogen, then brought to  $1500 \pm 10$  psi pressure by introduction of carbon dioxide by a Teledyne ISCO 500HP pump; the reactor configuration has been previously described [161]. During pressurization, the reactor was simultaneously heated to the desired temperature using heating tape. Temperature and pressure were monitored by a thermocouple inserted into the center of the reactor and a pressure transducer, respectively. The reaction was allowed to run for two hours, followed by depressurization over a 10 minute period and removal of the products.

### 8.3.3 Characterization

Scanning electron microscope (SEM) images were recorded using a Zeiss Ultra60 SEM operated at 5 kV accelerating voltage and 4 mm working distance. Image analysis of SEM images was carried out automatically using the *regionprops* function in MATLAB 2010a. Energy dispersive X-ray (EDX) analysis was carried out on the same Zeiss Ultra60 SEM with an accelerating voltage of 20 kV and a working distance of 8 mm.

## 8.4 Results and Discussion

The survey responses regarding the size of the design window are shown in Table 16, the responses regarding the model parameters are shown in Table 17, and the experts' confidence in whether the model structure is Arrhenius are listed in Table 18. From the responses in Table 16, it is clear there was significant conflict among the experts for the location of the design region. The approach adopted in this work synthesizes the experts' responses to resolve these conflicts in choosing the region for the design window. Given the responses in Table 16, Eq. 28 was used to determine that the window for the unified design region was  $[45 \text{ }^\circ\text{C}, 190 \text{ }^\circ\text{C}]$ . Once this design window was established, the individual models were built using the hierarchical Bayesian model with Gibbs sampling described in the Methodology section using the

Table 16: Expert survey responses for conjectures of the design window and confidence in conjecture for IrNP deposition in sc-CO<sub>2</sub>. Intervals denote 95% confidence interval

Expert	Conjectured LB	Conjectured UB	Confidence in LB and UB choices
1	[40,50]	[190,210]	4
2	[60,100]	[140,170]	7
3	[60,120]	[150,250]	3
4	[0,30]	[130,150]	3

Table 17: Expert conjectures for activation energy and nanoparticle size at the midpoint of the conjectured design window. Intervals denote 95% confidence interval

Expert	Conjecture for $E_a$	Conjecture for mean NP size in center of design region	Confidence in conjectures
1	[14,18]	[50,60]	4
2	[10,25]	[6,20]	7
3	[15,30]	[20,60]	5
4	[10.5,14.5]	[28,112]	7

Table 18: Confidence in Arrhenius model structure

Expert	Confidence in Arrhenius model structure
1	2
2	7
3	5
4	7

expert conjectures from the survey instrument shown in Table 17. Based on these expert conjectures, the Bayesian hierarchical model with Gibbs sampling was used to determine the updated values of the parameters  $E_a$  and  $\beta_0$ . These final model parameters are shown in Table 19, along with the midpoints of the experts' conjectured parameters to demonstrate how the Gibbs sampling method modified the given parameters by introducing the variance terms described above. Using these confidences

Table 19: Conjectured parameters and final parameters after Gibbs sampling of Bayesian hierarchical model

Expert	Conjectured $E_a$	Final $E_a$	Conjectured $\beta_0$	Final $\beta_0$
1	16	15.96	8.99	9.01
2	17.5	15.59	7.84	7.23
3	22.5	20.82	10.19	9.72
4	12.5	12.28	8.46	8.39

in Tables 16, 17, and 18, the trust each expert has in his/her model,  $\tilde{u}_i(\mathbf{x})$ , was calculated by Eq. 30. For example, the trust that Expert 1 has in his/her model is calculated as  $\tilde{u}_i(\mathbf{x}) = 0.4 \times 0.2 \times 0.4 = 0.03$ . Each expert's trust in his/her model and the weight given to each model in the unified model,  $w_i(\mathbf{x})$ , (i.e., the normalized trusts) are shown in Table 20. Figure 57 shows each expert's individual Arrhenius model, along with the unified model. The unified model predicts that the target of 40 nm IrNP will be achieved at  $T = 165$  °C.

Table 20: Confidence in Arrhenius model structure

Expert	Expert $i$ 's confidence in model, $\tilde{u}_i(\mathbf{x})$	Weight given to expert $i$ 's model, $w_i(\mathbf{x})$
1	0.03	0.05
2	0.34	0.57
3	0.08	0.13
4	0.15	0.25

The unified model was then used to specify the experimental design via the modified Fedorov exchange algorithm discussed in the Methodology section. The potential designs are shown in Figure 58 as a function of the tuning parameter  $\gamma$ , shown on the

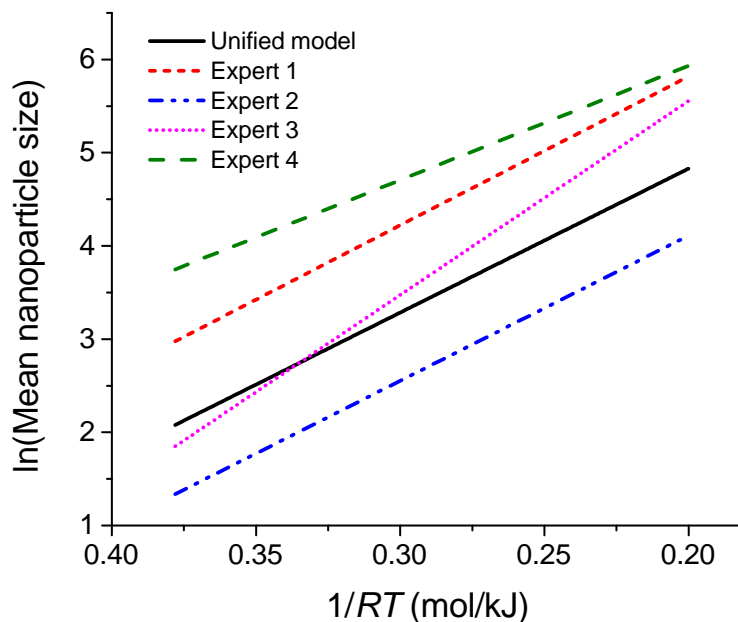


Figure 57: Individual expert models and unified model for IrNP deposition

y-axis. As  $\gamma$  increases, the designs move from a maximin, space-filling design (at  $\gamma = 0.5$ ) to an objective-oriented design (at  $\gamma = 4.5$ ). For the objective-oriented design, the design points cluster around the input of  $T = 165$  °C, the temperature at which the unified model predicts that 40 nm IrNP will be synthesized.

The parameter  $\gamma$  was set as  $\gamma = 4.5$  because this was an aggressive experimental design clustering points near the optimum predicted by the unified model at  $T = 165$  °C. The choice of  $\gamma = 4.5$  corresponds to the experimental design of [45 °C, 131 °C, 149 °C, 158 °C, 170 °C, and 184 °C]. These experiments were carried out as described in the Experimental Procedure section. A typical SEM image of the deposited IrNP products are shown in Figure 59 for IrNP synthesized at  $T = 149$  °C. Two types of structures are present: small Ir particles on the nanometer scale as well as large agglomerations of Ir. The mean IrNP sizes for the small IrNPs at each experimental design point are shown in Table 21. These data were then transformed using the Arrhenius equation and are shown in the Arrhenius plot in Figure 60. The

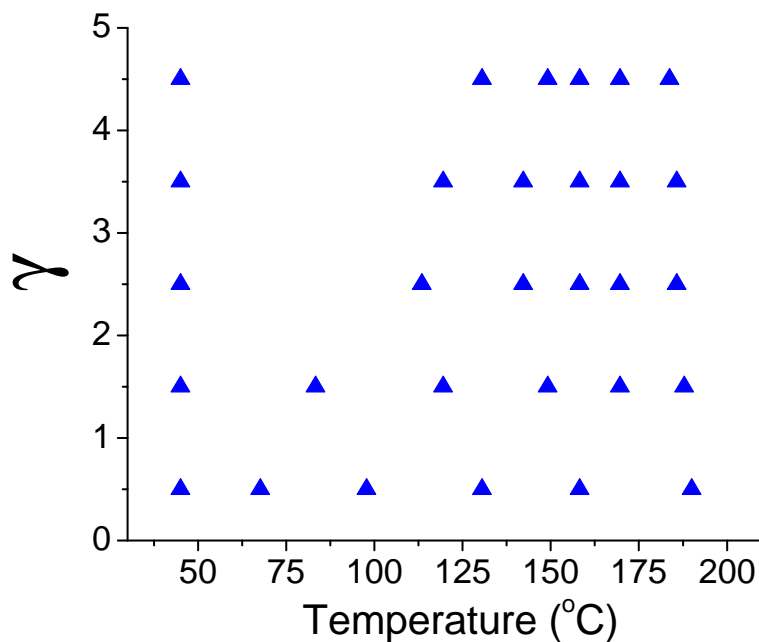


Figure 58: Potential experimental designs as a function of tuning parameter  $\gamma$

parameters from this Arrhenius plot are  $E_a = 14.3$  kJ/mol and  $\beta_0 = 7.3$  with an  $R^2 = 0.75$ . A *local* model incorporating the points in the region [131 °C, 184 °C] was also fit because these points are those clustered around the process optimum where the Arrhenius model is most useful. At the lowest temperature setting, another mechanism may be controlling nanoparticle deposition that cannot be described by the Arrhenius model, but since this data point is far away from the region of interest, it is not included. The parameters for this local model are  $\beta_0 = 13.4$  and  $E_a = 36.3$  kJ/mol, and its  $R^2$  value is 0.89. The chemical identity of the IrNPs was confirmed using EDX and these data are included in Appendix C.

#### 8.4.1 Plan for potential follow-up experiments

In order to quantify whether the model predictions were within the engineering tolerance of  $40 \pm 5$  nm, the evaluation metric developed by Casciato et al. in their Layers of Experiments (LoE) with Adaptive Combined Design (ACD) work was used. This

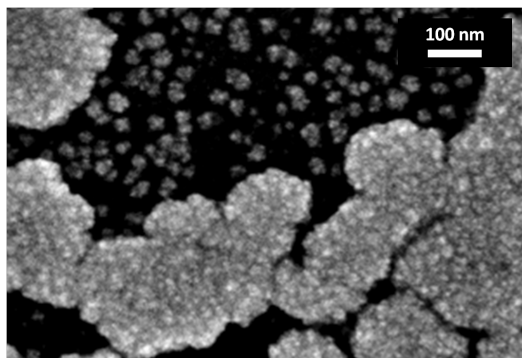


Figure 59: Typical SEM image of IrNP deposited on Si wafer surface at  $T = 149\text{ }^{\circ}\text{C}$

Table 21: Experimental data for IrNP deposited on Si wafer surface in sc-CO<sub>2</sub>

T (°C)	Mean IrNP size (nm)
45	8.1
131	12.0
149	23.4
158	32.0
170	37.8
184	40.9

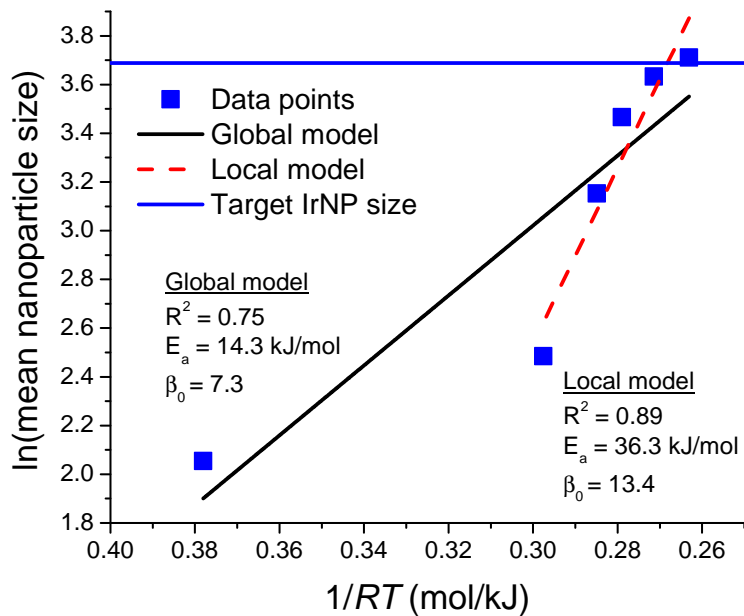


Figure 60: Arrhenius plots for global model and local model (incorporating points from  $131\text{ }^{\circ}\text{C}$  to  $184\text{ }^{\circ}\text{C}$ ) shown in Table 21

metric is defined as

$$L = \max(|T - (\hat{y}(\mathbf{x}) + \text{CI}(\mathbf{x}))|, |T - (\hat{y}(\mathbf{x}) - \text{CI}(\mathbf{x}))|) \quad (37)$$

where  $T_{NP}$  is the targeted value for the process output,  $\text{CI}(\mathbf{x})$  is the 95% confidence interval on the model prediction, and  $\hat{y}$  is the Arrhenius model. The uncertainty metric,  $L$ , is optimized over the design space:

$$\mathbf{x}^* = \min_{\mathbf{x}} L(\mathbf{x}) \quad (38)$$

The result of this optimization,  $L^*$ , is compared to the tolerance  $d$ . If  $L^* > d$ , the Layers of Experiment algorithm dictates that the experimenter continue on to the next layer of experiments for collecting additional data in a more focused region in order to further refine the model and find the process optimum. If  $L^* \leq d$ , the model is accurate to within the necessary engineering tolerances specified by the experimenter and can be used to optimize the process. Optimization routines were performed using the *fminunc* function in MATLAB 2010a.

Applying this methodology to the present work, the target nanoparticle size of 40 nm corresponds to an Arrhenius model value of  $\ln(40) = 3.69$ . The tolerance of  $\pm 5$  nm corresponds to a tolerance in the Arrhenius model of  $\ln(45) - \ln(40) = 0.118$ . The local model was used for this analysis since it is focused on describing the behavior of the system in the region of interest; understanding the global behavior of the system was not necessary. The resulting  $L$  metric along with the confidence interval, target, and Arrhenius model are shown in Figure 61. The  $L$  metric reaches a minimum at  $\frac{1}{RT} = 0.268$ , corresponding to a temperature of 175 °C. The  $L^*$  value is 0.322, greater than the  $d$  value of 0.118, indicating that the algorithm should proceed to the next layer since the model has not achieved the process optimum within the necessary tolerance set by the investigators. The LoE algorithm would constrain the design points in the region [159 °C, 189 °C], and the adaptive combined design would place design points at [159 °C, 159 °C, 172 °C, 176 °C, 189 °C, 189 °C] [43].

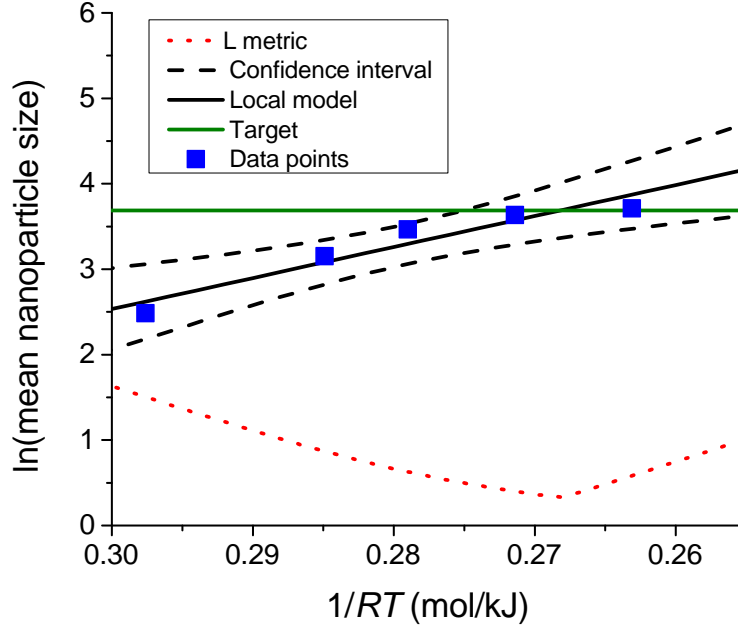


Figure 61: Plot of  $L$  metric with local Arrhenius model, confidence interval, and target IrNP size

The goal of the present work was to implement the IED methodology for efficient planning of IrNP deposition experiments from Ir(hfac)(COD) in sc-CO<sub>2</sub>. This methodology combined the use of prior data from a similar system, Ag(hfac)(COD) deposition in sc-CO<sub>2</sub>, with the opinions of experts in the area of nanomaterials synthesis. The target nanoparticle size was 40 nm  $\pm$  5 nm for this study.

The expert opinions gathered were first used to choose the size and location of the design space. For the Ag(hfac)(COD) system, the size and location of the design window was [60 °C, 150 °C]. Due to the experts' conflicting opinions elicited via survey, Eq. 28 was used to resolve these differences and widen the design window for the Ir(hfac)(COD) system to encompass [45 °C, 190 °C]. The individual models for each expert were built using the Gibbs resampling technique described in the Methodology section. Table 19 illustrates how the experts' conjectured values for the model parameters,  $\beta_0$  and  $E_a$ , were changed to the updated values based on this

Gibbs resampling. This result indicates that the 95% confidence intervals reported by each expert were successfully incorporated to account for the experts' uncertainty in each response. Next, the expert conjectures were used to develop a unified model. As illustrated by Figure 57, the unified model is weighted most heavily toward Expert 2, since s/he had the most confidence in his/her conjectures (see Table 20).

The Fedorov exchange algorithm was used with the unified model and varying values of  $\gamma$  to yield several possible experimental designs that could be chosen by the investigators (Figure 58). The unified model predicted that the process optimum for fabricating 40 nm IrNP would be found at 165 °C, and the choice of  $\gamma = 4.5$  served to cluster the design points near this optimum, with only one point far away at 45 °C. This result shows the usefulness of the IED methodology in efficiently directing the first round of experiments for a new system that is similar but not identical to an old system: the IED methodology clustered design points within the region of interest to the investigators. The local model fitted to the experimental data in Figure 60 indicates that the optimum is achieved at 175 °C, only 10 °C away from the prediction of the unified model. While 175 °C may not be the true optimum for the system, it is likely near this point.

In order to evaluate the tolerance of the local model, the LoE methodology developed by Casciato et al. was used [43]. The  $L^*$  metric was calculated to be 0.322, which is greater than the tolerance set by the investigators of 0.118 when using a local Arrhenius model in the region near the process optimum. Thus, it would be necessary to move on to a further layer of experiments to increase the reliability of the model predictions. If an additional round of experiments *were* necessary, the next layer would be in the region [159 °C, 189 °C]. Using the local model for this analysis was an important choice and contribution motivated by the desire to find the process optimum; model building was not the focus of this work, so building a useful global model was not necessary. Overall, the IED methodology succeeded in directing the

initial experimental design near the process optimum, achieving the primary goal of this work.

Though the IED methodology was useful as described above, there are drawbacks that should be addressed. While the IED approach succeeded in efficiently designing experiments to fabricate discrete IrNPs of 40 nm mean size, an unexpected result also occurred in this system. Large, agglomerated particles formed on the surface of the Si wafer, along with the smaller, discrete particles that were desired for the Ir(hfac)(COD) system. For the Ag(hfac)(COD) system, only discrete particles were observed, and this agglomeration was absent. Only a single experimental variable, the identity of the chemical precursor, was changed between the Ag(hfac)(COD) system and the Ir(hfac)(COD) system. However, this had significant effects on the process outcome: both mean IrNP size and morphology varied as a function of temperature, a result not observed for the old Ag(hfac)(COD) system. Thus, the IED methodology may be challenging to implement if unexpected results due to such a simple change of independent variables are possible. Moreover, manipulating more than one independent variable simultaneously may increase the likelihood of unintended and undesired outcomes for the new system, further limiting the applicability of the IED approach.

Furthermore, in addition to this issue, it was not possible for the experts surveyed to even predict the deposition of large, agglomerated particles. This was because questions of the survey did not address this possibility since it was not observed in the old, Ag(hfac)(COD) system. The questions of the survey assumed a particular behavior of the system — deposition of *solely* discrete Ir nanoparticles — that did not actually occur. However, the experts may have assumed that since the questions were asked in such a way, no other behavior was possible. Additionally, even if they believed another mode of growth were possible, framing the questions without this possibility may have discouraged the experts' thinking away from any alternative

system behaviors. Thus, another significant shortcoming of the IED methodology is its potential sensitivity to the questions that are asked. The questions asked may be as important as the answers received from the experts, since the survey will guide the potential range of responses the experts can give. Future studies implementing this methodology must be careful to avoid this potential pitfall. Comments received from the experts are included in Appendix D.

The reason for the differences in behavior between the Ag(hfac)(COD) system and Ir(hfac)(COD) system is not immediately obvious. Since the goal of this work was demonstration of the utility of the IED methodology for designing the initial round of experiments, an extensive study of the mechanism of deposition was not carried out. However, potential causes of the discrepancy in behavior for the old and new systems are described here. The morphology of the iridium nanoparticles potentially implies a Volmer-Weber (VW) growth mode, where particles deposited on a surface have stronger particle-particle interactions than particle-surface interactions, leading to the observed aggregation and lack of discrete particles in this work. This VW growth behavior has been observed frequently for iridium deposition in other systems, supporting the hypothesis of a Volmer-Weber growth mode in the current work [21, 105, 119]. Moreover, the Frank-van der Merwe (FM) growth mode, where particle-surface interactions are stronger than particle-particle interactions leading to discrete particles on the surface as a film is formed, has not been frequently observed for Ir deposition. On the other hand, silver can follow either a VW or FM growth mode [204, 306]. Thus, it is possible that the IrNP deposition proceeds by VW growth in sc-CO<sub>2</sub>, while AgNP deposition proceeds by FM growth.

It is also possible that there is gas-phase reaction occurring more readily in the Ir(hfac)(COD) system compared to the Ag(hfac)(COD) system, resulting in the observed agglomerated particles. The iridium precursor may dissolve in and/or transport through the sc-CO<sub>2</sub> more easily than the silver precursor. Increased solubility

and transport could be due to the fact that Ir(hfac)(COD) exists as a monomer, while Ag(hfac)(COD) exists as a dimer [15, 316]. Thus, Ir(hfac)(COD) has a higher vapor pressure than Ag(hfac)(COD), increasing its ability to dissolve in sc-CO<sub>2</sub>, and is smaller than the dimer Ag(hfac)(COD), increasing its ability to be transported through the sc-CO<sub>2</sub> [15, 316]. These effects would increase the available precursor for reaction in the fluid phase for the Ir(hfac)(COD) system, potentially explaining the different growth modes. A last potential explanation relates to the diffusivity of the Ir and Ag species on the surface. The self-diffusivity of iridium ( $4.7 \times 10^{-3} \text{ cm}^2 \cdot \text{s}^{-1}$ ) has been shown to be greater than that for silver ( $2.6 \times 10^{-3} \text{ cm}^2 \cdot \text{s}^{-1}$ ) [4] in the range [25 °C, 300 °C]. At the nanoscale, this difference may result in an increased ability of Ir to diffuse on the surface and thus promote the rate of aggregation relative to that of silver, resulting in the agglomerates observed. These conjectures should be investigated in future studies to improve understanding of the observed differences between AgNP and IrNP deposition shown here.

## **8.5 Conclusion**

The IED methodology was applied to efficiently choose experimental design points in a new system for the deposition of IrNP from Ir(hfac)(COD) in sc-CO<sub>2</sub>. The goal was a target IrNP mean size of 40 nm  $\pm$  5 nm. The IED approach used prior data relating the mean size of AgNP as a function of temperature in the sc-CO<sub>2</sub> system with Ag(hfac)(COD) as the precursor compound. Experts were supplied with data for the Ag(hfac)(COD) system and asked to give their conjectures about the design window, parameters, and Arrhenius model structure for the Ir(hfac)(COD) system based on the previous data and their expert knowledge. Conflicts in the experts' opinions were resolved by the proposed methodology, and the unified expert model predicted a process optimum at 165 °C. Experimental data for the Ir(hfac)(COD) system showed that the process optimum was at 175 °C, close to the predicted optimum of 165 °C.

The predictions made by the local model for the data, fit in the range [131 °C, 184 °C], did not fall within the desired engineering tolerance of 5 nm. Moreover, there was an additional growth mode of large, agglomerated islands of IrNP observed. The survey did not ask the experts for their thoughts on any possible behaviors of the system other than the fabrication of discrete IrNPs. Consequently, the experts did not have the opportunity to discuss any other outcomes. This sensitivity to the questions asked is a potentially significant drawback of the IED methodology.

This chapter concludes the novel experimental design methods developed and implemented in this thesis. In the following and final chapter (Chapter 9), the final conclusions of this thesis are given, and directions for future work are also discussed.

## CHAPTER IX

### CONCLUSIONS AND FUTURE WORK

The goals of this thesis were two-fold, and the thesis can be considered in two sections. In the first section, Chapters 2 through 5, process-structure-property relationships were investigated for the synthesis of various materials in *sc*-CO<sub>2</sub>. Within this section of the thesis, these PSP relationships were studied for three systems: (1) deposition of CZTS particles and films for solar energy applications, (2) deposition of ZnS nanoparticles on carbon nanotubes for optical applications, and (3) deposition of AgNPs for sensor applications. The relationships between substrate chemistry, temperature, and resulting structure and morphology were used to study the PSP relationships for the three systems in *sc*-CO<sub>2</sub>.

The main research theme that resulted from this section of the thesis was that surface chemistry has a significant effect on the nucleation and growth phenomena of nanomaterials fabricated in the *sc*-CO<sub>2</sub> system. Carboxyl and hydroxyl groups appear to promote nucleation and growth in the three systems studied. Moreover, by rationally controlling the surface chemistry (through selection of substrate or surface cleaning steps) it is possible to control the fabrication of thin films and nanoparticles with defined size.

In the second section of this thesis, Chapters 6 through 8 present novel experimental design methodologies that were developed and implemented in an interdisciplinary approach for the optimization of nanomaterials fabricated in advanced technology techniques, such as the supercritical carbon dioxide process described in Chapters 2 through 5. In this context, optimization refers to fabricating materials with the desired properties, such as mean nanoparticle size or film thickness. Specifically, these

experimental design approaches were developed to rapidly and efficiently optimize systems that are expensive to study in terms of time and money. The optimization of a AgNP deposition process was first investigated, using a novel layers of experiments with adaptive combined design methodology to fabricate AgNPs with a defined, optimal mean diameter. Next, a methodology for choosing the initial experimental design on a new system based on a related, previously studied system was investigated, taking advantage of expert opinion and prior data to plan experiments. Both the LoE/ACD and IED approaches took advantage of Arrhenius models built in the AgNP deposition studies detailed in the first section of the thesis. The main research theme from this section of the thesis is that novel experimental design methodologies can contribute to the efficient study of nanomaterials fabricated in the sc-CO<sub>2</sub> system.

### ***9.1 Process-structure-property investigations***

The deposition of CZTS particles and films in sc-CO<sub>2</sub> was achieved in Chapters 2 and 3 of this thesis. In Chapter 2, a continuous flow process was used to fabricate the CZTS particles, and large, agglomerated CZTS particles deposited onto an oxygen plasma cleaned Si surface. Detailed characterization of the products demonstrated the samples were indeed CZTS based on energy dispersive X-ray spectroscopy, X-ray diffraction, and Raman scattering analysis. The sc-CO<sub>2</sub> approach is greener than many alternative methods of CZTS fabrication that exist since the CO<sub>2</sub> solvent is more environmentally friendly than alternative solvents. Further study of the effect of substrate chemistry on CZTS deposition was carried out in Chapter 3 of this thesis. It was shown that the presence of an oxide layer on the surface of the substrate was vital for promoting particle nucleation that leads to the formation of a CZTS thin film. Moreover, the process inputs of temperature, concentration, and reaction time were used to vary deposition between favoring growth of large CZTS particles in the fluid phase and fabrication of a CZTS thin film on the surface of the substrate.

Controlling the deposition of the CZTS thin film vs. the deposition of large, agglomerated CZTS particles is a potentially valuable avenue for further research in the sc-CO<sub>2</sub> assisted fabrication of CZTS. One way this issue may be approached in future studies is to promote nucleation and growth only at the substrate surface by using a cold wall reactor and a heated substrate. Such approaches have been used previously for deposition of metals (such as copper) on Si surfaces in sc-CO<sub>2</sub> for microelectronics applications as well as in the microelectronics industry for deposition of Si surfaces incorporating dopants [25, 26]. One potential drawback of a cold wall reactor system is the introduction of temperature and/or concentration gradients that may affect the transport of precursors to the substrate surface [192, 293]. Nonetheless, a cold wall reactor approach may make it possible to further promote deposition of CZTS thin films over the growth of CZTS particles in the fluid phase. Future work should also entail the fabrication of devices based on CZTS deposited in the sc-CO<sub>2</sub> system. The work discussed in this thesis has focused mostly on the characterization of the structure and chemical properties of the CZTS material, but not how it would function in an actual device. Understanding how to manipulate the process conditions in the sc-CO<sub>2</sub> system to yield optimal device performance in terms of photoconversion efficiency would be a worthy avenue for further investigation.

ZnS nanoparticles were deposited on carbon nanotubes in the sc-CO<sub>2</sub> system in Chapter 4 of this thesis. The sc-CO<sub>2</sub> system is significantly greener than alternative approaches which use environmentally unfriendly chemicals. The ZnS-carbon nanotube nanocomposites that were fabricated possessed the characteristic chemical, physical, and optical properties that have been previously reported for ZnS-CNT compounds. Preliminary investigations showed that the deposition mechanism for decoration of the carbon nanotubes with ZnS nanoparticles proceeded in a heterogeneous manner.

One drawback of the sc-CO<sub>2</sub> approach implemented in Chapter 4 is that the

particles did not uniformly cover the surface of the CNTs. Future studies should focus on improving the process by encouraging the uniform deposition of ZnS NPs on the CNT surface. It may be possible to manipulate the chemical functionalization of the CNTs to encourage greater nucleation across the length of the nanotubes [16, 78, 153]. For example, the CNTs could be treated to increase the number of -COOH groups on the nanotubes. Alternatively, it may be possible to study the effect of alternative functional groups (such as amines or thiols) on the nucleation of ZnS particles on the CNT surface. Moreover, the size of the ZnS particles is relatively large compared to previous studies. Thus, it may be desirable to determine whether size control of the ZnS particles deposited on the CNT surface is possible in the supercritical carbon dioxide system.

Silver nanoparticles were deposited on Si and glass substrates in Chapter 5 of this thesis, and it was shown that the pretreatment of the substrate surface had a significant effect on the size and density of the deposited AgNPs. Moreover, by varying temperature, it was possible to control the size of the deposited AgNPs in the range from 10 nm to 200 nm. The data for particle size vs. temperature were used to construct Arrhenius models and estimate *effective* activation energies for the sc-CO<sub>2</sub> assisted deposition process. The models built and data collected in this chapter were then used to inform the LoE/ACD and IED work in the following chapters.

Future studies for the deposition of Ag nanoparticles in supercritical carbon dioxide should focus on shape control of the deposited nanoparticles, since certain nanostructures (such as nanoprisms) demonstrate higher SERS efficiency than the spherically shaped particles deposited here [136]. Shape control of AgNPs has been achieved in several other synthesis systems but has not been readily demonstrated for AgNP synthesis in sc-CO<sub>2</sub> [270, 281]. Controlling the shape of the AgNPs in the sc-CO<sub>2</sub> system may be achieved by the use of stabilizing agents such as polyvinylpyrrolidone

(PVP) or halide ions (such as  $\text{Br}^-$ ), which have been shown to direct the growth directions of nanoparticles and result in nanoparticles with defined shape [94, 283, 289].

## ***9.2 Novel experimental design approaches***

First, a layers of experiment with adaptive combined design methodology was developed in Chapters 6 and 7 for rapidly optimizing advanced processes, such as nanoparticle synthesis in supercritical carbon dioxide. This LoE/ACD approach was developed for systems that are expensive to study in terms of time and money. Consequently, it is difficult to optimize such systems because it is not feasible to conduct many experiments throughout the design space. The LoE/ACD approach was applied to find the optimal temperature for depositing AgNPs on Si surfaces in a supercritical carbon dioxide process. The LoE/ACD approach was successful in efficiently finding the process optimum for the selected optimal particle sizes by conducting a limited number of experiments in two subsequent layers.

While this approach was successful, there are several issues that remain unaddressed or unresolved and should be investigated in the future. The first and foremost is the issue of sample size. It is currently unclear how many experiments to conduct in each layer, and this is a vital issue to address for a methodology that purports to decrease the costs of optimizing the system. In the present work, a heuristic approach was used to decide how many experiments to conduct; however, the approach should be rigorous and systematically determine how many experiments are necessary to conduct within a layer [115, 172, 286]. Another area that was not addressed in this work was variance modeling [76, 198]. The LoE/ACD methodology was based solely on mean modeling of the nanoparticle size; however, it is possible that minimizing the variance of the nanoparticle size distribution may also be important. In addition to within-batch variability, it may be important to address the between-batch variability in this process.

The IED methodology described in Chapter 8 was used to plan the initial round of experiments for the deposition of Ir nanoparticles on a Si wafer surface in  $\text{sc-CO}_2$  from an iridium (I) hexafluoroacetylacetonate cyclooctadiene precursor. This methodology is most useful for rapidly optimizing a system that is expensive to study in terms of time and money. The major contribution of the IED approach is that it incorporates prior data on a similar, non-identical system for AgNP deposition; an Arrhenius model; and expert opinion in order to plan the initial experiments for the new system for Ir deposition. This was accomplished by surveying the experts for their opinions and, based on these opinions, constructing individual Arrhenius models corresponding to each expert. The individual models from each expert were then combined into a unified model using each expert's confidence in his or her conjectures. The resulting unified model was used in the experimental design, which combined a space-filling minimum energy design with an objective-oriented design. The resulting design focused the experiments near the process optimum but did not satisfy the engineering tolerance set on the model prediction. In addition to the small particles that were formed, large Ir particles were also deposited on the Si surface, a result that was not predicted by the experts in the survey instrument.

Future work in the area of initial experimental design should focus on improving the IED methodology and its shortcomings. First, the IED approach is highly sensitive to which specific questions are posed. For example, in the work discussed in Chapter 8, no questions were asked about alternative potential growth modes for the Ir particles, so this could not have been predicted by the experts completing the survey. It is possible that this work should be extended to include open-ended questions that allow experts to discuss any issues they feel may arise in the new system. However, such responses would be more difficult to quantify than the survey approach adopted here using confidences rated on a scale of 1 – 10. Potential collaboration

with experts in survey instrument writing may improve the usefulness of the IED approach. For example, collaboration with investigators who commonly design surveys in the biobehavioral sciences (such as psychology or anthropology) may fulfill this role [22, 66, 77, 239]. Second, similar to the issues raised above for the LoE/ACD approach, it is unclear what the optimal sample size should be for experiments conducted in the IED methodology. One potential approach to this issue could be surveying experts for their conjecture on how many experiments are necessary within the design space. Alternatively, it may be possible to produce pseudo-data from the experts' individual models (i.e., taking a bootstrapping approach), and identify the model coefficients using the pseudo-data. This approach could then be implemented for different numbers of samples and different experimental designs, e.g. a D-optimal design or space filling design, to determine how many experiments to conduct. Last, it was noted above that the IED methodology resulted in a model that did not meet the engineering tolerance on the model predictions set by the investigators. In such a situation, it would be necessary to use a sequential experimental design approach in combination with the IED method, such as the LoE method detailed here or other sequential design methodologies [6, 311].

# APPENDIX A

## XRD AND RAMAN DATA FOR CZTS DEPOSITED ON VARIOUS SUBSTRATES

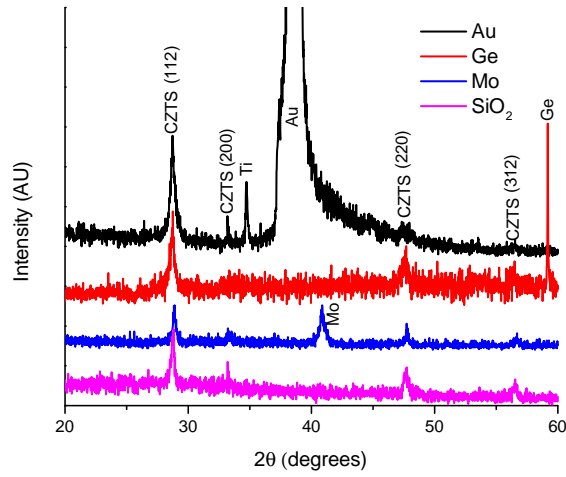


Figure 62: XRD spectra for samples fabricated in the base case conditions

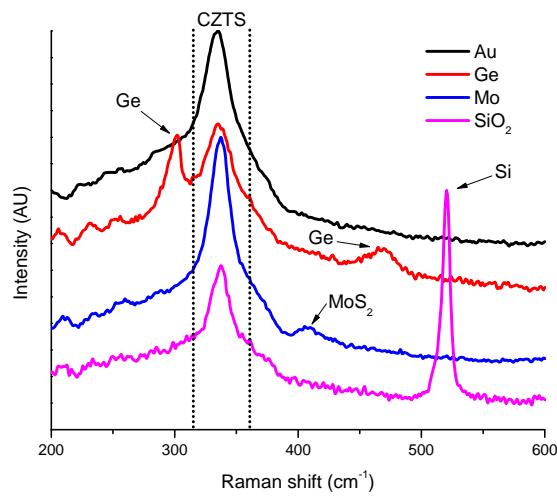


Figure 63: Raman spectra for samples fabricated in the base case conditions

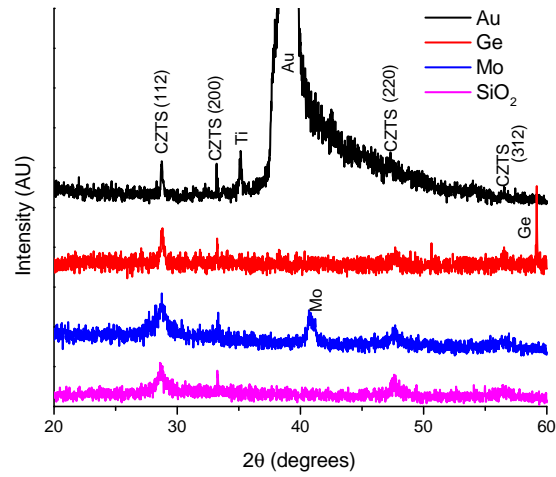


Figure 64: XRD spectra for samples fabricated at 1 minute reaction time

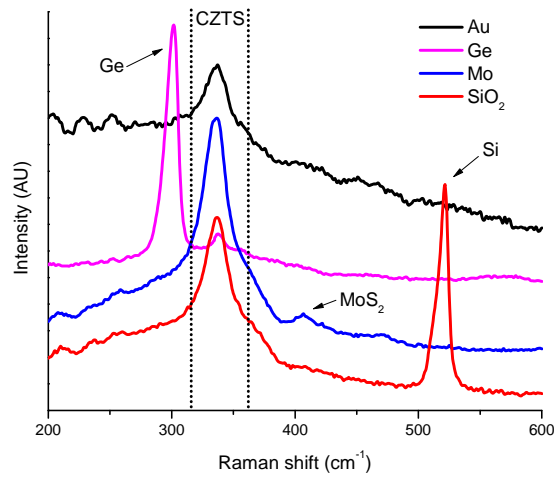


Figure 65: Raman spectra for samples fabricated at 1 minute reaction time

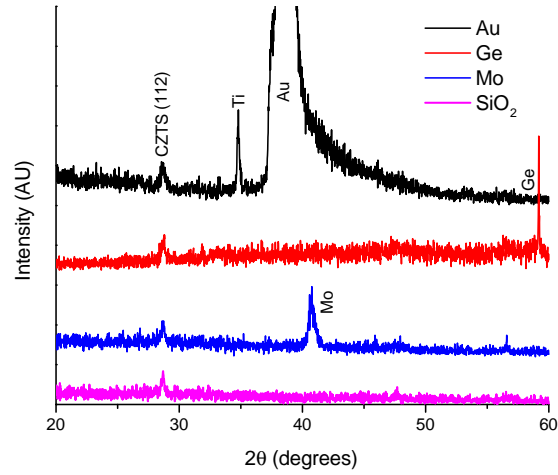


Figure 66: XRD spectra for samples fabricated at low concentration

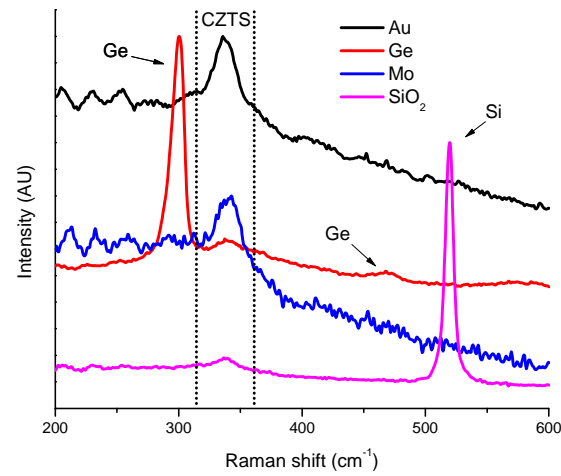


Figure 67: Raman spectra for samples fabricated at low concentration

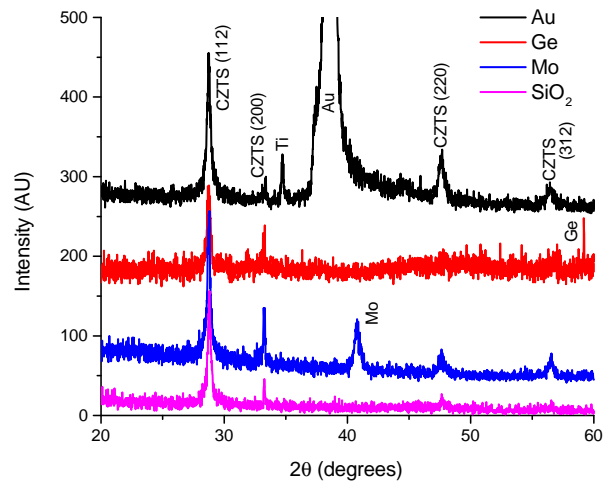


Figure 68: XRD spectra for samples fabricated at 400 °C

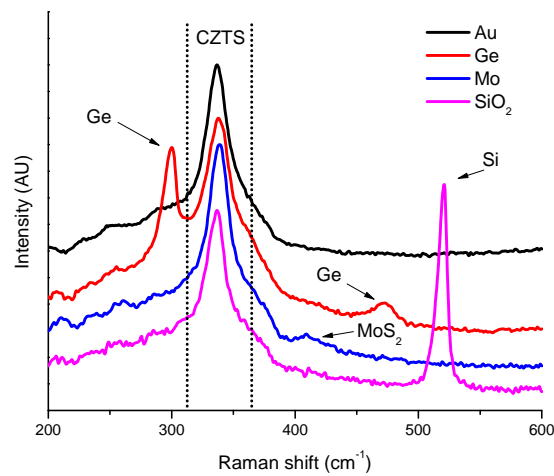


Figure 69: Raman spectra for samples fabricated at 400 °C

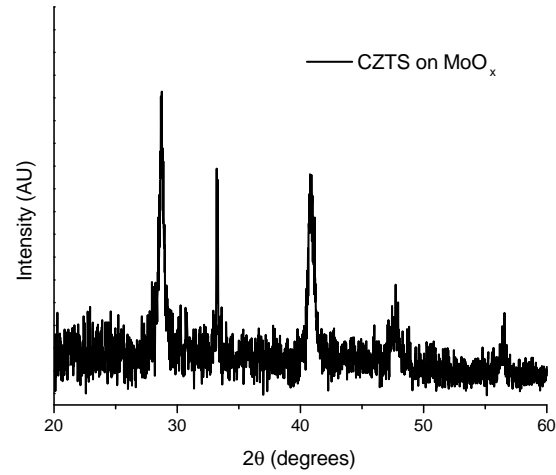


Figure 70: XRD spectrum for CZTS deposited on  $\text{MoO}_x$  surface

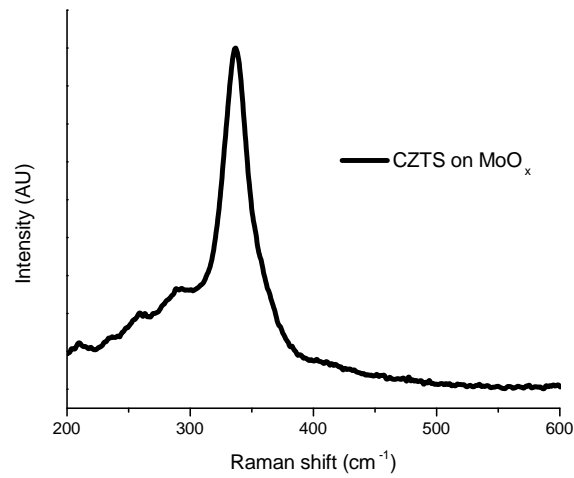


Figure 71: Raman spectrum for CZTS deposited on  $\text{MoO}_x$  surface

## APPENDIX B

### SURVEY FOR INITIAL DESIGN OF EXPERIMENTS

A supercritical carbon dioxide (sc-CO<sub>2</sub>) deposition method was used to decorate a silicon wafer with silver nanoparticles on the surface for application in surface-enhanced Raman spectroscopy. A 2 cm × 3 cm size silicon wafer purchased from University Wafer (10–20 Ω·cm, 100, *p*-type) was cleaned in an oxygen plasma for 10 min to populate the surface with reactive silanol groups. The substrate was placed in a 30 mL stainless steel reactor along with 50 mg of silver precursor silver(I) hexafluoroacetylacetonate cyclooctadiene (Ag(hfac)(COD)). The reactor was then charged with 400 psi of hydrogen gas as a reducing agent and the final pressure was increased to 1500 psi by introduction of carbon dioxide from a Teledyne ISCO 500HP high pressure pump. Surfaces were characterized using a Zeiss Ultra60 scanning electron microscope operated at 3 mm working distance and 5 kV accelerating voltage. Images were analyzed using the Image Analysis Toolbox in MATLAB R2010a, and mean nanoparticle diameter was calculated based on this automated analysis. Table 22 and Figure 72 summarize the data from this process. The Arrhenius plot for these data are shown in Figure 73. From the above data and using the Arrhenius equation, namely:

$$\text{mean AgNP diameter} = Ae^{(E_A/RT)} \quad (39)$$

the activation energy of the system is estimated as (with a 95% confidence interval in parenthesis):

$$\hat{E}_a = 15.25 \text{ kJ/mol}; (12.82991, 17.61729) \quad (40)$$

New System for Future Experimentation

Table 22: Table of experimental results

Temperature (°C)	Mean AgNP Diameter (nm)
60	18.3
60	17.8
90	24.3
98	29.2
98	32.3
108	34.9
120	44.0
120	47.5
121	41.8
128	42.0
128	49.0
150	51.8

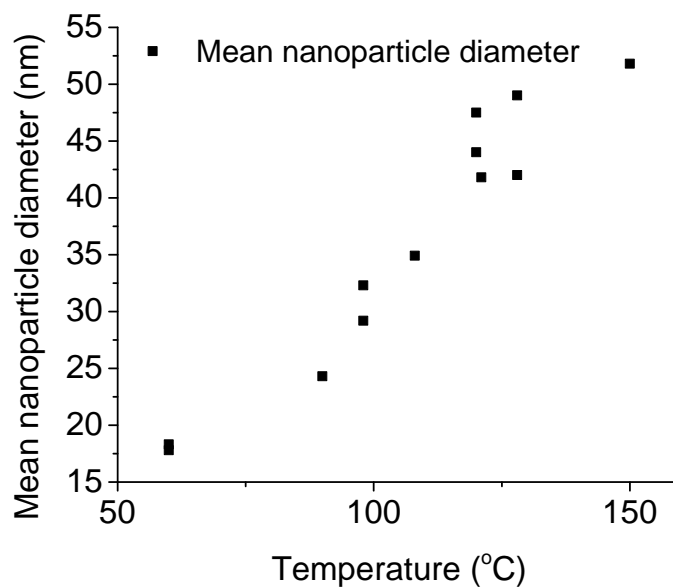


Figure 72: Plot of experimental data for mean nanoparticle size vs. temperature

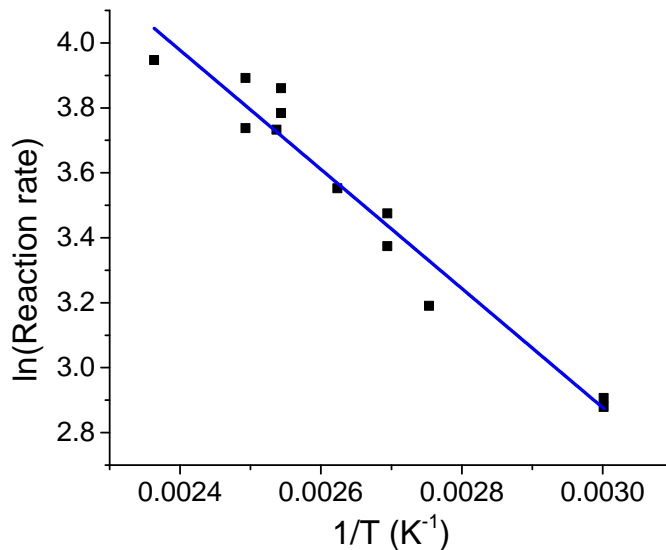


Figure 73: Arrhenius plot of experimental data

New experiments are going to be conducted using the same setup as the previous experiment but with one difference: the 50 mg of silver precursor is going to be replaced with 50 mg of iridium(I) hexafluoroacetylacetonate cyclooctadiene (Ir(hfac)(COD)) precursor. The goal of the new experiment is to find the system operating condition, in this case the temperature setting, to create iridium nanoparticles with a mean diameter of 40 nm. We will refer to the experimental setup when using the silver precursor as the old system and the experimental setup with the iridium precursor as the new system. Please answer the following questions based on your expectations for the new system.

Q1. The temperature range for the old system is 60°C to 150°C.

(a) For the new system, what do you expect is the minimum temperature needed in order to create nanoparticles? Please state your answer as a 95% confidence interval which you think will contain the true value.

(b) For the new system, what do you expect is the maximum temperature at which nanoparticles can still be created? Please state your answer as a 95% confidence

interval which you think will contain the true value.

(c) How confident are you in your answers to Q1, (a) and (b)? Please choose one integer value between 0 (complete guess) – 10 (complete confidence) (5 excluded).

Q2. Denote the midpoint of your interval in Q1(a) by  $a$  and the midpoint of your interval in Q1(b) by  $b$ . How confident are you that the new system behavior can be described by the Arrhenius model in the interval  $[a, b]$ ? Please choose one integer value between 0 (complete guess) – 10 (complete confidence) (5 excluded).

Q3. For question Q3, assume the behavior of the new system in the interval  $[a, b]$  can be described by the Arrhenius model. Additionally, let  $m$  denote the midpoint of the interval  $[a, b]$ .

(a) In the temperature range  $[a, b]$ , what do you expect the activation energy ( $E_a$ ) for the new system to be? Please express your answer as a 95% confidence interval which you think contain the true value.

(b) At the temperature  $m$ , what do you expect the mean nanoparticle size to be? Please express your answer as a 95% confidence interval which you think will contain the true value.

(c) Please choose one integer value between 0 (complete guess) – 10 (complete confidence) (5 excluded) to express your overall confidence in your answers to Q3 only.

## APPENDIX C

### EDX SPECTRUM FOR IRIDIUM NANOPARTICLES ON SILICON

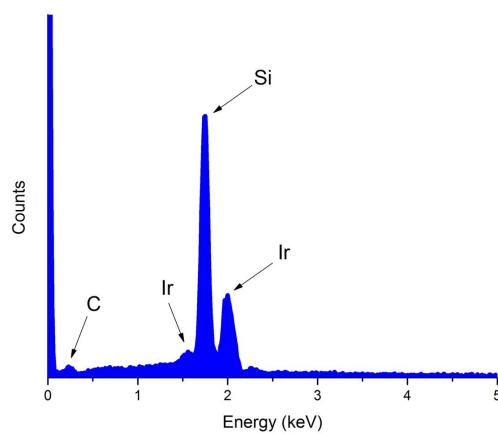


Figure 74: EDX spectra of Ir nanoparticles deposited on Si surface

## APPENDIX D

### EXPERTS' COMMENTS FOR SURVEY

- Expert 1 comments:
  - Q1. Note that this is range of experiment and not nanoparticle formation. Also, the 60 and 150 °C results seem not to follow an Arrhenius relationship (are the 60 C particles really pure Ag?). Most metal(hfac)COD organometallics will undergo facile removal of the COD ligand followed by adsorption of the metal(hfac) and bimolecular reaction to form metal in zero oxidation state and metal (hfac)<sub>2</sub>, which then desorbs. A key question is what does this relatively low activation energy represent? Surface diffusion?
- Expert 2 comments:
  - Q1.

For the new system, what do you expect is the minimum temperature needed in order to create nanoparticles? Please state you answer as a 95% confidence interval which you think will contain the true value.

This is very difficult to say because the chemistry of Ir is very different than Ag, specifically the redox potential for the metal ion and the hydrogen reduction reaction. It is quite possible that the hydrogen may not be a strong enough reducing agent to reduce the Ir<sup>+</sup> to ground state for nanoparticle formation. The first experiment would be to determine if the reduction is even possible and with that I would start with a value intermediate of the temperatures used in the old system. My estimation,

if the reaction is possible, is that the minimum temperature for the new system would be greater than the old system. Interval of 60 °C to 100 °C. For the new system, what do you expect is the maximum temperature at which nanoparticles can still be created? Please state your answer as a 95% confidence interval which you think will contain the true value.

The maximum temperature is likely due to the stability and solubility of the precursor and/or product, and thus would probably be similar to the old system, given that the 150 °C is an actual maximum temperature for the synthesis and not a limit of the experimental apparatus. Interval would be 140 °C to 170 °C.

My confidence would be a 7 but would like to do more background investigation of the literature before going further.

– Q2.

I would say 7, granted if the synthesis is even possible. On a side note, it is difficult to say why the Arrhenius model fits the data. It could be that the temperature is influencing the reduction reaction rate, leading to more nucleation sites at higher temperature, but this would lead to smaller particles, which is not observed. There could be a solubility effect, but it is not clear what the system pressure is at the different reaction temperatures. Was the reaction run isobaric or isometric? Lastly, the temperature effect could be influencing the ripening effect of the particles on the silicon surface. In this case the differences in the metal mobility of the new versus old system could be very different and may not follow the Arrhenius model at all.

– Q3. No justification, just numerical answers.

- Expert 3 comments:

No justification was given for any response, just numerical answers.

- Expert 4 comments:

I based my answers solely on the 1st ionization potentials of Ir vs. Ag, to estimate an  $E_a$  value for  $\text{Ir}^+$ .

## REFERENCES

- [1] ADSCHIRI, T., HAKUTA, Y., SUE, K., and ARAI, K., “Hydrothermal synthesis of metal oxide nanoparticles at supercritical conditions,” *Journal of Nanoparticle Research*, vol. 3, no. 2, pp. 227–235, 2001.
- [2] AGARWAL, A. K. and BRISK, M. L., “Sequential experimental design for precise parameter estimation. 1. Use of reparameterization,” *Industrial & Engineering Chemistry Process Design and Development*, vol. 24, no. 1, pp. 203–207, 1985.
- [3] AGHALAYAM, P., PARK, Y., FERNANDES, N., PAPAVALASSIOU, V., MHADESHWAR, A., and VLACHOS, D., “A C1 mechanism for methane oxidation on platinum,” *Journal of Catalysis*, vol. 213, no. 1, pp. 23 – 38, 2003.
- [4] AGRAWAL, P. M., RICE, B. M., and THOMPSON, D. L., “Predicting trends in rate parameters for self-diffusion on fcc metal surfaces,” *Surface Science*, vol. 515, no. 1, pp. 21–35, 2002.
- [5] AHMED, S., REUTER, K. B., GUNAWAN, O., GUO, L., ROMANKIW, L. T., and DELIGIANNI, H., “A high efficiency electrodeposited  $\text{Cu}_2\text{ZnSnS}_4$  solar cell,” *Advanced Energy Materials*, vol. 2, no. 2, pp. 253–259, 2012.
- [6] ALAEDDINI, A., YANG, K., and MURAT, A., “ASRSM: A sequential experimental design for response surface optimization,” *Quality and Reliability Engineering International*, 2012.

- [7] ALS-NIELSEN, B., CHEN, W., GLUUD, C., and KJAERGARD, L., “Association of funding and conclusions in randomized drug trials,” *The Journal of the American Medical Association*, vol. 290, no. 7, pp. 921–928, 2003.
- [8] ANASTAS, P. and WARNER, J., *Green Chemistry: Theory and Practice*. Oxford University Press, USA, 2000.
- [9] ANDERSON, M. and WHITCOMB, P., *Design of Experiments*. Wiley Online Library, 1974.
- [10] ANG, S.-Y. and WALSH, D. A., “Highly stable platinum electrocatalysts for oxygen reduction formed using supercritical fluid impregnation,” *Journal of Power Sources*, vol. 195, no. 9, pp. 2557–2563, 2010.
- [11] ANWAR, M., HOGARTH, C., and BULPETT, R., “Effect of substrate temperature and film thickness on the surface structure of some thin amorphous films of MoO<sub>3</sub> studied by X-ray photoelectron spectroscopy (ESCA),” *Journal of Materials Science*, vol. 24, no. 9, pp. 3087–3090, 1989.
- [12] ATKINS, P. and DE PAULA, J., *Physical Chemistry*. Oxford University Press, 7 ed., 2002.
- [13] BAHLAWANE, N., PREMKUMAR, P. A., BRECHLING, A., REISS, G., and KOHSE-HINGHAUS, K., “Alcohol-assisted CVD of silver using commercially available precursors,” *Chemical Vapor Deposition*, vol. 13, no. 8, pp. 401–407, 2007.
- [14] BAI, L., MA, X., LIU, J., SUN, X., ZHAO, D., and EVANS, D., “Rapid separation and purification of nanoparticles in organic density gradients,” *Journal of the American Chemical Society*, vol. 132, no. 7, pp. 2333–2337, 2010.

- [15] BAILEY, A., CORBITT, T. S., HAMPDEN-SMITH, M. J., DUESLER, E., and KODAS, T. T., "Synthesis and characterization of 1, 1, 1, 5, 5, 5-hexafluoroacetylacetonato-(1, 5-cyclooctadiene) silver (I) dimer. An unusual  $\beta$ -diketonate coordination mode," *Polyhedron*, vol. 12, no. 14, pp. 1785–1792, 1993.
- [16] BANERJEE, S., KAHN, M. G., and WONG, S. S., "Rational chemical strategies for carbon nanotube functionalization," *Chemistry-A European Journal*, vol. 9, no. 9, pp. 1898–1908, 2003.
- [17] BARKHOUSE, D., GUNAWAN, O., GOKMEN, T., TODOROV, T., and MITZI, D., "Device characteristics of a 10.1% hydrazine-processed  $\text{Cu}_2\text{ZnSn}(\text{Se,S})_4$  solar cell," *Progress in Photovoltaics: Research and Applications*, vol. 20, no. 1, pp. 6–11, 2011.
- [18] BAYRAKÇEKEN, A., SMIRNOVA, A., KITKAMTHORN, U., AINDOW, M., TURKER, L., EROUGLU, I., and ERKEY, C., "Pt-based electrocatalysts for polymer electrolyte membrane fuel cells prepared by supercritical deposition technique," *Journal of Power Sources*, vol. 179, no. 2, pp. 532–540, 2008.
- [19] BECHET, D., COULEAUD, P., FROCHOT, C., VIRIOT, M., GUILLEMIN, F., and BARBERI-HEYOB, M., "Nanoparticles as vehicles for delivery of photodynamic therapy agents," *Trends in Biotechnology*, vol. 26, no. 11, pp. 612–621, 2008.
- [20] BELL, A., "The impact of nanoscience on heterogeneous catalysis," *Science*, vol. 299, no. 5613, pp. 1688–1691, 2003.
- [21] BERKO, A. and SOLYMOSI, F., "Effects of different gases on the morphology of Ir nanoparticles supported on the  $\text{TiO}_2$  (110)-(1 $\times$ 2) surface," *The Journal of Physical Chemistry B*, vol. 104, no. 44, pp. 10215–10221, 2000.

- [22] BERNARD, H. R., *Research Methods in Anthropology: Qualitative and Quantitative Approaches*. Altamira press, 2011.
- [23] BHARGAVA, R., GALLAGHER, D., HONG, X., and NURMIKKO, A., “Optical properties of manganese-doped nanocrystals of ZnS,” *Physical Review Letters*, vol. 72, no. 3, pp. 416–419, 1994.
- [24] BINNIG, G., QUATE, C., and GERBER, C., “Atomic force microscope,” *Physical Review Letters*, vol. 56, no. 9, pp. 930–933, 1986.
- [25] BLACKBURN, J., LONG, D., CABAÑAS, A., and WATKINS, J., “Deposition of conformal copper and nickel films from supercritical carbon dioxide,” *Science*, vol. 294, no. 5540, pp. 141–145, 2001.
- [26] BLOEM, J., OEI, Y., DE MOOR, H., HANSEN, J., and GILING, L., “Near equilibrium growth of silicon by CVD I. The Si-Cl-H system,” *Journal of Crystal Growth*, vol. 65, no. 1, pp. 399–405, 1983.
- [27] BOX, G., *Box on Quality and Discovery*. John Wiley & Sons, Inc., 2000.
- [28] BOX, G. and HILL, W., “Discrimination among mechanistic models,” *Technometrics*, vol. 9, pp. 57–71, 1967.
- [29] BOX, G. and HUNTER, J., “The  $2^{k-p}$  fractional factorial designs,” *Technometrics*, vol. 3, no. 3, pp. 311–351, 1961.
- [30] BOX, G., HUNTER, J., and HUNTER, W., *Statistics for Experimenters: Design, Innovation, and Discovery*, vol. 13. Wiley Online Library, 2005.
- [31] BOX, G. and HUNTER, W., “The experimental study of physical mechanisms,” *Technometrics*, vol. 7, pp. 23–42, 1965.
- [32] BOX, G. and LUCAS, H., “Design of experiments in non-linear situations,” *Biometrika*, vol. 46, no. 1, pp. 77–90, 1959.

- [33] BOX, G. and WILSON, K., “On the experimental attainment of optimum conditions,” *Journal of the Royal Statistical Society. Series B (Methodological)*, vol. 13, no. 1, pp. 1–45, 1951.
- [34] BROWNING, N., CHISHOLM, M., and PENNYCOOK, S., “Atomic-resolution chemical analysis using a scanning transmission electron microscope,” *Nature*, vol. 366, no. 6451, pp. 143–146, 1993.
- [35] BROX, B. and OLEFJORD, I., “ESCA studies of MoO<sub>2</sub> and MoO<sub>3</sub>,” *Surface and Interface Analysis*, vol. 13, no. 1, pp. 3–6, 1988.
- [36] BRUMFIEL, G., “Nanotechnology: A little knowledge...,” *Nature*, vol. 424, no. 6946, pp. 246–248, 2003.
- [37] BURGESS, D., “Nanotechnology: Tissue penetration of photodynamic therapy,” *Nature Reviews Cancer*, vol. 12, no. 11, pp. 737–737, 2012.
- [38] BURNHAM, K.P.; ANDERSON, D., *Model Selection and Inference: A Practical Information-Theoretic Approach*. Springer-Verlag, 1998.
- [39] CABAÑAS, A., BLACKBURN, J. M., and WATKINS, J. J., “Deposition of Cu films from supercritical fluids using Cu(I)  $\beta$ -diketonate precursors,” *Microelectronic Engineering*, vol. 64, pp. 53–61, 2002.
- [40] CAI, J., RUFFIEUX, P., JAAFAR, R., BIERI, M., BRAUN, T., BLANKENBURG, S., MUOTH, M., SEITSONEN, A., SALEH, M., FENG, X., and OTHERS, “Atomically precise bottom-up fabrication of graphene nanoribbons,” *Nature*, vol. 466, no. 7305, pp. 470–473, 2010.
- [41] CANCELL, F. and AYMONIER, C., “Design of functional nanostructured materials using supercritical fluids,” *The Journal of Supercritical Fluids*, vol. 47, no. 3, pp. 508–516, 2009.

- [42] CASCIATO, M. J., KIM, S., LU, J., HESS, D. W., and GROVER, M. A., “Optimization of carbon dioxide-assisted nanoparticle deposition process with uncertain design space,” in *Proceedings of the 11th International Symposium on Process Systems Engineering*, 2012.
- [43] CASCIATO, M., KIM, S., LU, J., HESS, D., and GROVER, M., “Optimization of a carbon dioxide-assisted nanoparticle deposition process using sequential experimental design with adaptive design space,” *Industrial & Engineering Chemistry Research*, vol. 51, no. 11, pp. 4363–4370, 2012.
- [44] CASCIATO, M., LEVITIN, G., HESS, D., and GROVER, M., “Controlling the properties of silver nanoparticles deposited on surfaces using supercritical carbon dioxide for surface-enhanced Raman spectroscopy,” *Journal of Nanoparticle Research*, vol. 14, no. 5, pp. 1–15, 2012.
- [45] CASCIATO, M., LEVITIN, G., HESS, D., and GROVER, M., “Synthesis of  $\text{Cu}_2\text{ZnSnS}_4$  micro-and nanoparticles via a continuous-flow supercritical carbon dioxide process,” *ChemSusChem*, vol. 5, no. 7, pp. 1186–1189, 2012.
- [46] CASCIATO, M., LEVITIN, G., HESS, D., and GROVER, M., “Synthesis of optically active ZnS-carbon nanotube nanocomposites in supercritical carbon dioxide via a single source diethyldithiocarbamate precursor,” *Industrial & Engineering Chemistry Research*, 2012.
- [47] CHAN, H. and KWOK, P., “Production methods for nanodrug particles using the bottom-up approach,” *Advanced Drug Delivery Reviews*, vol. 63, no. 6, pp. 406–416, 2011.
- [48] CHANEY, S., SHANMUKH, S., DLUHY, R., and ZHAO, Y., “Aligned silver nanorod arrays produce high sensitivity surface-enhanced Raman spectroscopy substrates,” *Applied Physics Letters*, vol. 87, no. 3, pp. 0319081–0319083, 2005.

- [49] CHEN, M., FALKNER, J., GUO, W., ZHANG, J., SAYES, C., and COLVIN, V., “Synthesis and self-organization of soluble monodisperse palladium nanoclusters,” *Journal of Colloid and Interface Science*, vol. 287, no. 1, pp. 146–151, 2005.
- [50] CHEN, Y., ZHANG, Y., LIANG, W., and LI, X., “Gold nanocages as contrast agents for two-photon luminescence endomicroscopy imaging,” *Nanomedicine: Nanotechnology, Biology and Medicine*, vol. 8, no. 8, pp. 1267 – 1270, 2012.
- [51] CHENG, A., MANNO, M., KHARE, A., LEIGHTON, C., CAMPBELL, S., and AYDIL, E., “Imaging and phase identification of  $\text{Cu}_2\text{ZnSnS}_4$  thin films using confocal Raman spectroscopy,” *Journal of Vacuum Science & Technology A: Vacuum, Surfaces, and Films*, vol. 29, no. 5, pp. 051203–11, 2011.
- [52] CHERNOFF, H., “Locally optimal designs for estimating parameters,” *The Annals of Mathematical Statistics*, vol. 24, no. 4, pp. 586–602, 1953.
- [53] CHIH, Y. and CHENG, W., “Supercritical carbon dioxide-assisted synthesis of silver nano-particles in polyol process,” *Materials Science and Engineering: B*, vol. 145, no. 1, pp. 67–75, 2007.
- [54] CHO, M.-H., ROH, Y., WHANG, C., JEONG, K., NAHM, S., KO, D.-H., LEE, J., LEE, N., and FUJIHARA, K., “Thermal stability and structural characteristics of  $\text{HfO}$  films on Si (100) grown by atomic layer deposition,” *Applied Physics Letters*, vol. 81, pp. 472–475, 2002.
- [55] CHOI, K. and HAN, C., “Low temperature copper etching using an inductively coupled plasma with ultraviolet light irradiation,” *Journal of The Electrochemical Society*, vol. 145, no. 3, pp. 37–39, 1998.
- [56] CIOPPA, T. M. and LUCAS, T. W., “Efficient nearly orthogonal and space-filling Latin hypercubes,” *Technometrics*, vol. 49, no. 1, pp. 45–55, 2007.

- [57] COCHRAN, W. and COX, G., *Experimental Designs*. John Wiley & Sons, 1957.
- [58] COLLINS, G., KOLESNIK, M., KRSTIC, V., and HOLMES, J., “Germanium nanowire synthesis from fluorothiolate-capped gold nanoparticles in supercritical carbon dioxide,” *Chemistry of Materials*, vol. 22, no. 18, pp. 5235–5243, 2010.
- [59] CORBIERRE, M. and LENNOX, R., “Preparation of thiol-capped gold nanoparticles by chemical reduction of soluble Au (I)-thiolates,” *Chemistry of Materials*, vol. 17, no. 23, pp. 5691–5696, 2005.
- [60] CREMER, P. S., SU, X., SHEN, Y. R., and SOMORJAI, G. A., “Hydrogenation and dehydrogenation of propylene on Pt(111) studied by sum frequency generation from UHV to atmospheric pressure,” *The Journal of Physical Chemistry*, vol. 100, no. 40, pp. 16302–16309, 1996.
- [61] CUI, W., LI, X., ZHOU, S., and WENG, J., “Investigation on process parameters of electrospinning system through orthogonal experimental design,” *Journal of Applied Polymer Science*, vol. 103, no. 5, pp. 3105–3112, 2006.
- [62] CULLEN, A. C. and FREY, H. C., *Probabilistic Techniques in Exposure Assessment: A Handbook for Dealing with Variability and Uncertainty in Models and Inputs*. Plenum Publishing Corporation, 1999.
- [63] DAMLEN, P., WAKEFIELD, J., and WALKER, S., “Gibbs sampling for Bayesian non-conjugate and hierarchical models by using auxiliary variables,” *Journal of the Royal Statistical Society: Series B (Statistical Methodology)*, vol. 61, no. 2, pp. 331–344, 1999.
- [64] DASGUPTA, T., *Robust Parameter Design for Automatically Controlled Systems and Nanostructure Synthesis*. PhD thesis, H. Milton Stewart School of Industrial & Systems Engineering, Georgia Institute of Technology, 2007.

- [65] DAVIS, S. G., MHADESHWAR, A. B., VLACHOS, D. G., and WANG, H., “A new approach to response surface development for detailed gas-phase and surface reaction kinetic model optimization,” *International Journal of Chemical Kinetics*, vol. 36, no. 2, pp. 94–106, 2004.
- [66] DE VAUS, D., *Surveys in Social Research*. Routledge, 2013.
- [67] DEITZEL, J., KLEINMEYER, J., HARRIS, D., and BECK TAN, N., “The effect of processing variables on the morphology of electrospun nanofibers and textiles,” *Polymer*, vol. 42, no. 1, pp. 261–272, 2001.
- [68] DEL CASTILLO, E., “Stopping rules for steepest ascent in experimental optimization,” *Communications in Statistics - Simulation and Computation*, vol. 26, no. 4, pp. 1599–1615, 1997.
- [69] DERSCH, R., STEINHART, M., BOUDRIOT, U., GREINER, A., and WENDORFF, J., “Nanoprocessing of polymers: applications in medicine, sensors, catalysis, photonics,” *Polymers for Advanced Technologies*, vol. 16, no. 2-3, pp. 276–282, 2005.
- [70] DHAS, N., ZABAN, A., and GEDANKEN, A., “Surface synthesis of zinc sulfide nanoparticles on silica microspheres: Sonochemical preparation, characterization, and optical properties,” *Chemistry of Materials*, vol. 11, no. 3, pp. 806–813, 1999.
- [71] DIXIT, P., VÄHÄNEN, S., SALONEN, J., and MONNOYER, P., “Effect of process gases on fabricating tapered through-silicon vias by continuous SF<sub>6</sub>/O<sub>2</sub>/Ar plasma etching,” *ECS Journal of Solid State Science and Technology*, vol. 1, no. 3, pp. 107–116, 2012.

- [72] DOOLEY, K., GHONASGI, D., KNOPF, F., and GAMBRELL, R., “Supercritical CO<sub>2</sub>-cosolvent extraction of contaminated soils and sediments,” *Environmental Progress*, vol. 9, no. 4, pp. 197–203, 1990.
- [73] DOSHI, J. and RENEKER, D., “Electrospinning process and applications of electrospun fibers,” *Journal of Electrostatics*, vol. 35, no. 2, pp. 151–160, 1995.
- [74] DOWLING, A., “Development of nanotechnologies,” *Materials Today*, vol. 7, no. 12, pp. 30–35, 2004.
- [75] DU, J., FU, L., LIU, Z., HAN, B., LI, Z., LIU, Y., SUN, Z., and ZHU, D., “Facile route to synthesize multiwalled carbon nanotube/zinc sulfide heterostructures: optical and electrical properties,” *The Journal of Physical Chemistry B*, vol. 109, no. 26, pp. 12772–12776, 2005.
- [76] DU, X. and CHEN, W., “Towards a better understanding of modeling feasibility robustness in engineering design,” *Journal of Mechanical Design*, vol. 122, p. 385, 2000.
- [77] DUNN, D., *Research Methods for Social Psychology*. Wiley-Blackwell, 2009.
- [78] DYKE, C. A. and TOUR, J. M., “Covalent functionalization of single-walled carbon nanotubes for materials applications,” *The Journal of Physical Chemistry A*, vol. 108, no. 51, pp. 11151–11159, 2004.
- [79] EDINGTON, E. and ONGHENA, P., *Randomization Tests*, vol. 191. Chapman & Hall/CRC, 2007.
- [80] EDINGTON, J., *Practical Electron Microscopy in Materials Science*. Van Nostrand Reinhold Company, 1976.

- [81] EDWARDS, P. and THOMAS, J., “Gold in a metallic divided state - from Faraday to present-day nanoscience,” *Angewandte Chemie International Edition*, vol. 46, no. 29, pp. 5480–5486, 2007.
- [82] ELLIS, S., “Surface studies on single-crystal germanium,” *Journal of Applied Physics*, vol. 28, no. 11, pp. 1262–1269, 1957.
- [83] EUSTIS, S. and EL-SAYED, M., “Why gold nanoparticles are more precious than pretty gold: Noble metal surface plasmon resonance and its enhancement of the radiative and nonradiative properties of nanocrystals of different shapes,” *Chemical Society Reviews*, vol. 35, no. 3, pp. 209–217, 2006.
- [84] EVANOFF JR, D. and CHUMANOV, G., “Synthesis and optical properties of silver nanoparticles and arrays,” *ChemPhysChem*, vol. 6, no. 7, pp. 1221–1231, 2005.
- [85] EYETT, M. and BÄUERLE, D., “Influence of the beam spot size on ablation rates in pulsed-laser processing,” *Applied Physics Letters*, vol. 51, p. 2054, 1987.
- [86] FAN, S.-K. S. and HUANG, K.-N., “A new search procedure of steepest ascent in response surface exploration,” *Journal of Statistical Computation and Simulation*, vol. 81, no. 6, pp. 661–678, 2011.
- [87] FANG, K.-T., LIN, D. K., WINKER, P., and ZHANG, Y., “Uniform design: theory and application,” *Technometrics*, vol. 42, no. 3, pp. 237–248, 2000.
- [88] FARADAY, M., “The Bakerian Lecture: Experimental relations of gold (and other metals) to light,” *Philosophical Transactions of the Royal Society of London*, vol. 147, pp. 145–181, 1857.
- [89] FEDOROV, V. and HACKL, P., *Model-oriented Design of Experiments*, vol. 125. Springer Verlag, 1997.

- [90] FENG, S., ZHAO, J., and ZHU, Z., “The manufacture of carbon nanotubes decorated with ZnS to enhance the ZnS photocatalytic activity,” *New Carbon Materials*, vol. 23, no. 3, pp. 228–234, 2008.
- [91] FERNANDES, P., SALOMÉ, P., and DA CUNHA, A., “Growth and Raman scattering characterization of  $\text{Cu}_2\text{ZnSnS}_4$  thin films,” *Thin Solid Films*, vol. 517, no. 7, pp. 2519–2523, 2009.
- [92] FERNANDEZ, C. and WAI, C., “Continuous tuning of cadmium sulfide and zinc sulfide nanoparticle size in a water-in-supercritical carbon dioxide microemulsion,” *Chemistry – A European Journal*, vol. 13, no. 20, pp. 5838–5844, 2007.
- [93] FEYNMAN, R., “There’s plenty of room at the bottom,” *Engineering and Science*, vol. 23, no. 5, pp. 22–36, 1960.
- [94] FILANKEMBO, A., GIORGIO, S., LISIECKI, I., and PILENI, M., “Is the anion the major parameter in the shape control of nanocrystals?,” *The Journal of Physical Chemistry B*, vol. 107, no. 30, pp. 7492–7500, 2003.
- [95] FISHER, R., *The Design of Experiments*. Oliver & Boyd, 1935.
- [96] FOGLER, H. S., *Elements of Chemical Reaction Engineering*. Prentice Hall, fourth ed., 2006.
- [97] FONASH, S. J., ASHOK, S., and SINGH, R., “Effect of ion-beam sputter damage on Schottky barrier formation in silicon,” *Applied Physics Letters*, vol. 39, no. 5, pp. 423–425, 1981.
- [98] FONSECA, G. S., MACHADO, G., TEIXEIRA, S. R., FECHER, G. H., MORAIS, J., ALVES, M., and DUPONT, J., “Synthesis and characterization of catalytic iridium nanoparticles in imidazolium ionic liquids,” *Journal of Colloid and Interface Science*, vol. 301, no. 1, pp. 193–204, 2006.

- [99] FRANCESCHINI, G. and MACCHIETTO, S., “Model-based design of experiments for parameter precision: State of the art,” *Chemical Engineering Science*, vol. 63, no. 19, pp. 4846 – 4872, 2008.
- [100] GAGO, R., VÁZQUEZ, L., PLANTEVIN, O., SÁNCHEZ-GARCÍA, J., VARELA, M., BALLESTEROS, M., ALBELLA, J., and METZGER, T., “Temperature influence on the production of nanodot patterns by ion beam sputtering of Si (001),” *Physical Review B*, vol. 73, no. 15, p. 155414, 2006.
- [101] GAGO, R., VÁZQUEZ, L., CUERNO, R., VARELA, M., BALLESTEROS, C., and ALBELLA, J. M., “Nanopatterning of silicon surfaces by low-energy ion-beam sputtering: dependence on the angle of ion incidence,” *Nanotechnology*, vol. 13, no. 3, p. 304, 2002.
- [102] GALOPIN, E., BARBILLAT, J., COFFINIER, Y., SZUNERITS, S., PATRIARCHE, G., and BOUKHERROUB, R., “Silicon nanowires coated with silver nanostructures as ultrasensitive interfaces for surface-enhanced Raman spectroscopy,” *ACS Applied Materials & Interfaces*, vol. 1, no. 7, pp. 1396–1403, 2009.
- [103] GARNETT, E. and YANG, P., “Silicon nanowire radial p-n junction solar cells,” *Journal of the American Chemical Society*, vol. 130, no. 29, pp. 9224–9225, 2008.
- [104] GELFAND, A. E., HILLS, S. E., RACINE-POON, A., and SMITH, A. F., “Illustration of Bayesian inference in normal data models using gibbs sampling,” *Journal of the American Statistical Association*, vol. 85, no. 412, pp. 972–985, 1990.
- [105] GERFIN, T., HÄLG, W. J., ATAMNY, F., and DAHMEN, K.-H., “Growth of iridium films by metal organic chemical vapour deposition,” *Thin Solid Films*, vol. 241, no. 1, pp. 352–355, 1994.

- [106] GOEL, T., HAFTKA, R. T., SHYY, W., and WATSON, L. T., “Pitfalls of using a single criterion for selecting experimental designs,” *International Journal for Numerical Methods in Engineering*, vol. 75, no. 2, pp. 127–155, 2008.
- [107] GOLOVERDA, G., JACKSON, B., KIDD, C., and KOLESNICHENKO, V., “Synthesis of ultrasmall magnetic iron oxide nanoparticles and study of their colloid and surface chemistry,” *Journal of Magnetism and Magnetic Materials*, vol. 321, no. 10, pp. 1372–1376, 2009.
- [108] GROSSMANN, I. and KRAVANJA, Z., “Mixed-integer nonlinear programming techniques for process systems engineering,” *Computers & Chemical Engineering*, vol. 19, pp. 189–204, 1995.
- [109] GROSSMANN, I. and WESTERBERG, A., “Research challenges in process systems engineering,” *AIChE Journal*, vol. 46, no. 9, pp. 1700–1703, 2004.
- [110] GRZELCZAK, M., PÉREZ-JUSTE, J., MULVANEY, P., and LIZ-MARZÁN, L., “Shape control in gold nanoparticle synthesis,” *Chemical Society Reviews*, vol. 37, no. 9, pp. 1783–1791, 2008.
- [111] GU, F., LI, C., and WANG, S., “Solution-chemical synthesis of carbon nanotube/ZnS nanoparticle core/shell heterostructures,” *Inorganic Chemistry*, vol. 46, no. 13, pp. 5343–5348, 2007.
- [112] GUERRERO-MARTÍNEZ, A., BARBOSA, S., PASTORIZA-SANTOS, I., and LIZ-MARZÁN, L., “Nanostars shine bright for you: Colloidal synthesis, properties and applications of branched metallic nanoparticles,” *Current Opinion in Colloid & Interface Science*, vol. 16, no. 2, pp. 118–127, 2011.
- [113] GUNAWAN, O. and GUHA, S., “Characteristics of vapor–liquid–solid grown silicon nanowire solar cells,” *Solar Energy Materials and Solar Cells*, vol. 93, no. 8, pp. 1388–1393, 2009.

- [114] HAAS, W., RATH, T., PEIN, A., RATTENBERGER, J., TRIMMEL, G., and HOFER, F., “The stoichiometry of single nanoparticles of copper zinc tin selenide,” *Chemical Communications*, vol. 47, no. 7, pp. 2050–2052, 2011.
- [115] HAMILTON, M. A. and COLLINGS, B. J., “Determining the appropriate sample size for nonparametric tests for location shift,” *Technometrics*, vol. 33, no. 3, pp. 327–337, 1991.
- [116] HANNON, J., KODAMBAKA, S., ROSS, F., and TROMP, R., “The influence of the surface migration of gold on the growth of silicon nanowires,” *Nature*, vol. 440, no. 7080, pp. 69–71, 2006.
- [117] HANRATH, T. and KORGEL, B., “Nucleation and growth of germanium nanowires seeded by organic monolayer-coated gold nanocrystals,” *Journal of the American Chemical Society*, vol. 124, no. 7, pp. 1424–1429, 2002.
- [118] HASELL, T., LAGONIGRO, L., PEACOCK, A., YODA, S., BROWN, P., SAZIO, P., and HOWDLE, S., “Silver nanoparticle impregnated polycarbonate substrates for surface enhanced Raman spectroscopy,” *Advanced Functional Materials*, vol. 18, no. 8, pp. 1265–1271, 2008.
- [119] HAYEK, K., GOLLER, H., PENNER, S., RUPPRECHTER, G., and ZIMMERMANN, C., “Regular alumina-supported nanoparticles of iridium, rhodium and platinum under hydrogen reduction: structure, morphology and activity in the neopentane conversion,” *Catalysis Letters*, vol. 92, no. 1, pp. 1–9, 2004.
- [120] HAYNES, C. L. and VAN DUYN, R. P., “Nanosphere lithography: A versatile nanofabrication tool for studies of size-dependent nanoparticle optics,” *The Journal of Physical Chemistry B*, vol. 105, no. 24, pp. 5599–5611, 2001.
- [121] HEDGES, L. and OLKIN, I., “Meta analysis: A review and a new view,” *Educational Researcher*, pp. 14–16, 1986.

- [122] HELANDER, I. and MAKELA, A., "Contact urticaria to zinc diethyldithiocarbamate (zdc)," *Contact Dermatitis*, vol. 9, no. 4, pp. 327–328, 1983.
- [123] HESS, D., JENSEN, K., and ANDERSON, T., "Chemical vapor deposition: A chemical engineering perspective," *Reviews in Chemical Engineering*, vol. 3, no. 2, pp. 97–186, 2011.
- [124] HILDEBRANDT, P. and STOCKBURGER, M., "Surface-enhanced resonance Raman spectroscopy of Rhodamine 6G adsorbed on colloidal silver," *The Journal of Physical Chemistry*, vol. 88, no. 24, pp. 5935–5944, 1984.
- [125] HILL, W. J. and HUNTER, W. G., "A review of response surface methodology: a literature survey," *Technometrics*, vol. 8, no. 4, pp. 571–590, 1966.
- [126] HOLMES, J., JOHNSTON, K., DOTY, R., and KORGEL, B., "Control of thickness and orientation of solution-grown silicon nanowires," *Science*, vol. 287, no. 5457, pp. 1471–1473, 2000.
- [127] HU, J., REN, L., GUO, Y., LIANG, H., CAO, A., WAN, L., and BAI, C., "Mass production and high photocatalytic activity of ZnS nanoporous nanoparticles," *Angewandte Chemie*, vol. 117, no. 8, pp. 1295–1299, 2005.
- [128] HUANG, J., JIANG, T., HAN, B., GAO, H., CHANG, Y., ZHAO, G., and WU, W., "Hydrogenation of olefins using ligand-stabilized palladium nanoparticles in an ionic liquid," *Chemical Communications*, no. 14, pp. 1654–1655, 2003.
- [129] HULL, R., LI, L., XING, Y., and CHUSUEI, C., "Pt nanoparticle binding on functionalized multiwalled carbon nanotubes," *Chemistry of Materials*, vol. 18, no. 7, pp. 1780–1788, 2006.

- [130] HUTCHISON, J., “Greener nanoscience: a proactive approach to advancing applications and reducing implications of nanotechnology,” *ACS Nano*, vol. 2, no. 3, pp. 395–402, 2008.
- [131] HUXTER, V., MIRKOVIC, T., NAIR, P., and SCHOLTS, G., “Demonstration of bulk semiconductor optical properties in processable Ag<sub>2</sub>S and EuS nanocrystalline systems,” *Advanced Materials*, vol. 20, no. 12, pp. 2439–2443, 2008.
- [132] HYEON, T., “Chemical synthesis of magnetic nanoparticles,” *Chemical Communications*, no. 8, pp. 927–934, 2002.
- [133] JEN-LA PLANTE, I., ZEID, T., YANG, P., and MOKARI, T., “Synthesis of metal sulfide nanomaterials via thermal decomposition of single-source precursors,” *Journal of Materials Chemistry*, vol. 20, no. 32, pp. 6612–6617, 2010.
- [134] JENSEN, T., MALINSKY, M., HAYNES, C., and VAN DUYN, R., “Nanosphere lithography: Tunable localized surface plasmon resonance spectra of silver nanoparticles,” *The Journal of Physical Chemistry B*, vol. 104, no. 45, pp. 10549–10556, 2000.
- [135] JI, M., CHEN, X., WAI, C. M., and FULTON, J. L., “Synthesizing and dispersing silver nanoparticles in a water-in-supercritical carbon dioxide microemulsion,” *Journal of the American Chemical Society*, vol. 121, no. 11, pp. 2631–2632, 1999.
- [136] JIN, R., CAO, Y., MIRKIN, C. A., KELLY, K., SCHATZ, G. C., and ZHENG, J., “Photoinduced conversion of silver nanospheres to nanoprisms,” *Science*, vol. 294, no. 5548, pp. 1901–1903, 2001.
- [137] JOHNSON, M., MOORE, L., and YLVISAKER, D., “Minimax and maximin distance designs,” *Journal of Statistical Planning and Inference*, vol. 26, no. 2, pp. 131 – 148, 1990.

- [138] JOSEPH, V. R. and MELKOTE, S. N., “Statistical adjustments to engineering models,” *Journal of Quality Technology*, vol. 41, no. 4, pp. 362–375, 2009.
- [139] JOSEPH, V. and HUNG, Y., “Orthogonal maximin Latin hypercube design,” *Statistica Sinica*, vol. 18, pp. 171–186, 2008.
- [140] JUHA, L., BITTNER, M., CHVOSTOVA, D., KRASA, J., OTCENASEK, Z., PRAG, A., ULLSCHMIED, J., PIENKA, Z., KRZYWINSKI, J., PELKA, J., and OTHERS, “Ablation of organic polymers by 46.9 nm laser radiation,” *Applied Physics Letters*, vol. 86, no. 3, pp. 034109–034109, 2005.
- [141] JUNK, A. and RIESS, F., “From an idea to a vision: There’s plenty of room at the bottom,” *American Journal of Physics*, vol. 74, p. 825, 2006.
- [142] KAHL, M., VOGES, E., KOSTREWA, S., VIETS, C., and HILL, W., “Periodically structured metallic substrates for SERS,” *Sensors and Actuators B: Chemical*, vol. 51, no. 1, pp. 285–291, 1998.
- [143] KALANTAR-ZADEH, K. and FRY, B., *Nanotechnology Enabled Sensors*. Springer, US, 2007.
- [144] KENNEDY, M. C. and O’HAGAN, A., “Bayesian calibration of computer models,” *Journal of the Royal Statistical Society: Series B (Statistical Methodology)*, vol. 63, no. 3, pp. 425–464, 2001.
- [145] KESSLER, F. and RUDMANN, D., “Technological aspects of flexible CIGS solar cells and modules,” *Solar Energy*, vol. 77, no. 6, pp. 685–695, 2004.
- [146] KHARE, A., WILLS, A., AMMERMAN, L., AYDIL, E., and OTHERS, “Size control and quantum confinement in  $\text{Cu}_2\text{ZnSnS}_4$  nanocrystals,” *Chemical Communications*, vol. 47, no. 42, pp. 11721–11723, 2011.

- [147] KIM, H. and SIGMUND, W., “Zinc sulfide nanocrystals on carbon nanotubes,” *Journal of Crystal Growth*, vol. 255, no. 1, pp. 114–118, 2003.
- [148] KIM, S., *Experimental Design Methods for Nanofabrication Processes*. PhD thesis, H. Milton Stewart School of Industrial & Systems Engineering, Georgia Institute of Technology, August 2011.
- [149] KITAJIMA, M., KUROKI, H., SHINNO, H., and NAKAMURA, K. G., “Growth of silicon oxide on silicon in the thin film region in an oxygen plasma,” *Solid State Communications*, vol. 83, no. 5, pp. 385–388, 1992.
- [150] KITIYANAN, B., ALVAREZ, W., HARWELL, J., and RESASCO, D., “Controlled production of single-wall carbon nanotubes by catalytic decomposition of CO on bimetallic Co–Mo catalysts,” *Chemical Physics Letters*, vol. 317, no. 3, pp. 497–503, 2000.
- [151] KLAR, T., PERNER, M., GROSSE, S., VON PLESSEN, G., SPIRKL, W., and FELDMANN, J., “Surface-plasmon resonances in single metallic nanoparticles,” *Physical Review Letters*, vol. 80, no. 19, pp. 4249–4252, 1998.
- [152] KNEIPP, K., KNEIPP, H., MANOHARAN, R., HANLON, E. B., ITZKAN, I., DASARI, R. R., and FELD, M. S., “Extremely large enhancement factors in surface-enhanced Raman scattering for molecules on colloidal gold clusters,” *Applied Spectroscopy*, vol. 52, no. 12, pp. 1493–1497, 1998.
- [153] KOVALCHUK, A. A., SHEVCHENKO, V. G., SHCHEGOLIKHIN, A. N., NEDOREZOVA, P. M., KLYAMKINA, A. N., and ALADYSHEV, A. M., “Effect of carbon nanotube functionalization on the structural and mechanical properties of polypropylene/MWCNT composites,” *Macromolecules*, vol. 41, no. 20, pp. 7536–7542, 2008.

- [154] KUNG, H. and KUNG, M., “Nanotechnology: applications and potentials for heterogeneous catalysis,” *Catalysis Today*, vol. 97, no. 4, pp. 219–224, 2004.
- [155] KUO, Y. and LEE, S., “Room-temperature copper etching based on a plasma–copper reaction,” *Applied Physics Letters*, vol. 78, no. 7, pp. 1002–1004, 2001.
- [156] LARSON, D., ZIPFEL, W., WILLIAMS, R., CLARK, S., BRUCHEZ, M., WISE, F., and WEBB, W., “Water-soluble quantum dots for multiphoton fluorescence imaging *in vivo*,” *Science*, vol. 300, no. 5624, pp. 1434–1436, 2003.
- [157] LEE, R. E., “Microfabrication by ion-beam etching,” *Journal of Vacuum Science and Technology*, vol. 16, no. 2, pp. 164–170, 1979.
- [158] LEE, S., PARK, K., CHOI, J., KWON, B., and SUNG, Y., “Nanoparticle synthesis and electrocatalytic activity of Pt alloys for direct methanol fuel cells,” *Journal of the Electrochemical Society*, vol. 149, no. 10, pp. 1299–1304, 2002.
- [159] LESKELÄ, M. and RITALA, M., “Atomic layer deposition (ALD): from precursors to thin film structures,” *Thin Solid Films*, vol. 409, no. 1, pp. 138–146, 2002.
- [160] LEUTWYLER, W., BÜRGI, S., and BURGL, H., “Semiconductor clusters, nanocrystals, and quantum dots,” *Science*, vol. 271, p. 933, 1996.
- [161] LEVITIN, G., BUSH, D., ECKERT, C. A., and HESS, D. W., “Phase behavior and modeling of CO<sub>2</sub>/methanol/tetramethylammonium bicarbonate and CO<sub>2</sub>/methanol/tetramethylammonium bicarbonate/water mixtures at high pressures,” *Journal of Chemical & Engineering Data*, vol. 49, no. 3, pp. 599–606, 2004.
- [162] LEWIS, N., “Toward cost-effective solar energy use,” *Science*, vol. 315, no. 5813, pp. 798–801, 2007.

- [163] LI, J., STEIN, D., MCMULLAN, C., BRANTON, D., AZIZ, M. J., and GOLOVCHENKO, J. A., “Ion-beam sculpting at nanometre length scales,” *Nature*, vol. 412, no. 6843, pp. 166–169, 2001.
- [164] LI, Q. and WANG, C., “Fabrication of wurtzite ZnS nanobelts via simple thermal evaporation,” *Applied Physics Letters*, vol. 83, no. 2, pp. 359–361, 2003.
- [165] LI, Y., DING, Y., ZHANG, Y., and QIAN, Y., “Photophysical properties of ZnS quantum dots,” *Journal of Physics and Chemistry of Solids*, vol. 60, no. 1, pp. 13–15, 1999.
- [166] LIN, C. and KUO, Y., “Plasma etching of copper thin film over a dielectric step and electromigration failure mechanism,” in *MRS Proceedings*, vol. 1428, Cambridge Univ Press, 2012.
- [167] LIN, Y., CUI, X., YEN, C., and WAI, C., “Platinum/carbon nanotube nanocomposite synthesized in supercritical fluid as electrocatalysts for low-temperature fuel cells,” *The Journal of Physical Chemistry B*, vol. 109, no. 30, pp. 14410–14415, 2005.
- [168] LIN, Y., CUI, X., YEN, C., and WAI, C., “PtRu/carbon nanotube nanocomposite synthesized in supercritical fluid: a novel electrocatalyst for direct methanol fuel cells,” *Langmuir*, vol. 21, no. 24, pp. 11474–11479, 2005.
- [169] LIU, D.-J., WEEKS, J. D., JOHNSON, M. D., and WILLIAMS, E. D., “Two-dimensional facet nucleation and growth on Si(111),” *Physical Review B*, vol. 55, pp. 7653–7659, Mar 1997.
- [170] LIU, Y., CHU, H., and ZHAO, Y., “Silver nanorod array substrates fabricated by oblique angle deposition: morphological, optical, and SERS characterizations,” *The Journal of Physical Chemistry C*, vol. 114, no. 18, pp. 8176–8183, 2010.

- [171] LIU, Z., LIN, X., LEE, J. Y., ZHANG, W., HAN, M., and GAN, L. M., “Preparation and characterization of platinum-based electrocatalysts on multi-walled carbon nanotubes for proton exchange membrane fuel cells,” *Langmuir*, vol. 18, no. 10, pp. 4054–4060, 2002.
- [172] LOEPPKY, J. L., SACKS, J., and WELCH, W. J., “Choosing the sample size of a computer experiment: A practical guide,” *Technometrics*, vol. 51, no. 4, 2009.
- [173] LOMBARDO, S. J. and BELL, A. T., “A review of theoretical models of adsorption, diffusion, desorption, and reaction of gases on metal surfaces,” *Surface Science Reports*, vol. 13, no. 1-2, pp. 3 – 72, 1991.
- [174] LU, W. and LIEBER, C., “Nanoelectronics from the bottom up,” *Nature Materials*, vol. 6, no. 11, pp. 841–850, 2007.
- [175] LU, Y. and CHEN, S., “Nanopatterning of a silicon surface by near-field enhanced laser irradiation,” *Nanotechnology*, vol. 14, no. 5, p. 505, 2003.
- [176] LU, Z. and YIN, Y., “Colloidal nanoparticle clusters: functional materials by design,” *Chemical Society Reviews*, 2012.
- [177] MANZOOR, K., VADERA, S., KUMAR, N., and KUTTY, T., “Synthesis and photoluminescent properties of ZnS nanocrystals doped with copper and halogen,” *Materials Chemistry and Physics*, vol. 82, no. 3, pp. 718–725, 2003.
- [178] MARLIN, T. and MARLIN, T., *Process Control: Designing Processes and Control Systems for Dynamic Performance*. McGraw-Hill New York, 1995.
- [179] MAYER, T. M., DE BOER, M. P., SHINN, N. D., CLEWS, P. J., and MICHALSKE, T. A., “Chemical vapor deposition of fluoroalkylsilane monolayer films for adhesion control in microelectromechanical systems,” *Journal of*

- Vacuum Science & Technology B: Microelectronics and Nanometer Structures*, vol. 18, no. 5, pp. 2433–2440, 2000.
- [180] MCLEOD, M., ANAND, M., KITCHENS, C., and ROBERTS, C., “Precise and rapid size selection and targeted deposition of nanoparticle populations using CO<sub>2</sub> gas expanded liquids,” *Nano Letters*, vol. 5, no. 3, pp. 461–465, 2005.
- [181] MEHR, C., BISWAL, R., COLLINS, J., and COCHRAN, H., “Supercritical carbon dioxide extraction of caffeine from guaraná,” *The Journal of Supercritical Fluids*, vol. 9, no. 3, pp. 185–191, 1996.
- [182] MEHTA, S., KUMAR, S., CHAUDHARY, S., BHASIN, K., and GRADZIELSKI, M., “Evolution of ZnS nanoparticles via facile CTAB aqueous micellar solution route: A study on controlling parameters,” *Nanoscale Research Letters*, vol. 4, no. 1, pp. 17–28, 2009.
- [183] MENDES, R., NOBRE, B., CARDOSO, M., PEREIRA, A., and PALAVRA, A., “Supercritical carbon dioxide extraction of compounds with pharmaceutical importance from microalgae,” *Inorganica Chimica Acta*, vol. 356, pp. 328–334, 2003.
- [184] MEWS, A., KADAVANICH, A., BANIN, U., and ALIVISATOS, A., “Structural and spectroscopic investigations of CdS/HgS/CdS quantum-dot quantum wells,” *Physical Review B*, vol. 53, no. 20, pp. 13242–13245, 1996.
- [185] MEYER, E., “Atomic force microscopy,” *Progress in Surface Science*, vol. 41, no. 1, pp. 3–49, 1992.
- [186] MHADESHWAR, A. B. and VLACHOS, D. G., “Hierarchical multiscale mechanism development for methane partial oxidation and reforming and for thermal decomposition of oxygenates on Rh,” *The Journal of Physical Chemistry B*, vol. 109, no. 35, pp. 16819–16835, 2005.

- [187] MHADESHWAR, A. and VLACHOS, D., “Is the water gas shift reaction on Pt simple?: Computer-aided microkinetic model reduction, lumped rate expression, and rate-determining step,” *Catalysis Today*, vol. 105, no. 1, pp. 162 – 172, 2005.
- [188] MICHAEL, Y., XU, H., PENN, S., and CROMER, R., “SERS nanoparticles: a new optical detection modality for cancer diagnosis,” *Nanomedicine*, vol. 2, no. 5, pp. 725–734, 2007.
- [189] MIJATOVIC, D., EIJKEL, J., and VAN DEN BERG, A., “Technologies for nanofluidic systems: Top-down vs. bottom-up - A review,” *Lab on a Chip*, vol. 5, no. 5, pp. 492–500, 2005.
- [190] MILLER, J. and MILLER, J., *Statistics for Analytical Chemistry*. John Wiley & Sons, New York, NY, 1988.
- [191] MITCHELL, T., “An algorithm for the construction of D-optimal experimental designs,” *Technometrics*, vol. 16, no. 2, pp. 203–210, 1974.
- [192] MOFFAT, H. and JENSEN, K. F., “Complex flow phenomena in MOCVD reactors: I. Horizontal reactors,” *Journal of Crystal Growth*, vol. 77, no. 1, pp. 108–119, 1986.
- [193] MONTGOMERY, D., *Design and Analysis of Experiments*, vol. 6. John Wiley & Sons, Inc., 2005.
- [194] MOULIJN, J., STANKIEWICZ, A., GRIEVINK, J., and GÓRAK, A., “Process intensification and process systems engineering: A friendly symbiosis,” *Computers & Chemical Engineering*, vol. 32, no. 1, pp. 3–11, 2008.

- [195] MURPHY, C., “Sustainability as an emerging design criterion in nanoparticle synthesis and applications,” *Journal of Materials Chemistry*, vol. 18, no. 19, pp. 2173–2176, 2008.
- [196] MURPHY, C. and JANA, N., “Controlling the aspect ratio of inorganic nanorods and nanowires,” *Advanced Materials*, vol. 14, no. 1, p. 80, 2002.
- [197] MYERS, R. H., KHURI, A. I., and CARTER, W. H., “Response surface methodology: 1966–1988,” *Technometrics*, vol. 31, no. 2, pp. 137–157, 1989.
- [198] MYERS, R. H., KHURI, A. I., and VINING, G., “Response surface alternatives to the Taguchi robust parameter design approach,” *The American Statistician*, vol. 46, no. 2, pp. 131–139, 1992.
- [199] MYERS, R. and KHURI, A., “A new procedure for steepest ascent,” *Communications in Statistics-Theory and Methods*, vol. 8, no. 14, pp. 1359–1376, 1979.
- [200] NAKAMURA, S., HARADA, Y., and SENO, M., “Novel metalorganic chemical vapor deposition system for GaN growth,” *Applied Physics Letters*, vol. 58, no. 18, pp. 2021–2023, 1991.
- [201] NANDA, J., SAPRA, S., SARMA, D., CHANDRASEKHARAN, N., and HODES, G., “Size-selected zinc sulfide nanocrystallites: synthesis, structure, and optical studies,” *Chemistry of Materials*, vol. 12, no. 4, pp. 1018–1024, 2000.
- [202] NIE, S., XING, Y., KIM, G., and SIMONS, J., “Nanotechnology applications in cancer,” *Annual Reviews of Biomedical Engineering*, vol. 9, pp. 257–288, 2007.
- [203] NÖLL, T. and NÖLL, G., “Strategies for wiring redox-active proteins to electrodes and applications in biosensors, biofuel cells, and nanotechnology,” *Chemical Society Reviews*, vol. 40, no. 7, pp. 3564–3576, 2011.

- [204] OATES, T. and MÜCKLICH, A., “Evolution of plasmon resonances during plasma deposition of silver nanoparticles,” *Nanotechnology*, vol. 16, no. 11, p. 2606, 2005.
- [205] OH, S. H., FISHER, G. B., CARPENTER, J. E., and GOODMAN, D., “Comparative kinetic studies of CO-O<sub>2</sub> and CO-NO reactions over single crystal and supported rhodium catalysts,” *Journal of Catalysis*, vol. 100, no. 2, pp. 360 – 376, 1986.
- [206] OHDE, H., HUNT, F., and WAI, C., “Synthesis of silver and copper nanoparticles in a water-in-supercritical-carbon dioxide microemulsion,” *Chemistry of Materials*, vol. 13, no. 11, pp. 4130–4135, 2001.
- [207] OHDE, H., OHDE, M., BAILEY, F., KIM, H., and WAI, C., “Water-in-CO<sub>2</sub> microemulsions as nanoreactors for synthesizing CdS and ZnS nanoparticles in supercritical CO<sub>2</sub>,” *Nano Letters*, vol. 2, no. 7, pp. 721–724, 2002.
- [208] OHDE, H., KRAMER, S., MOORE, S., and WAI, C. M., “Low-temperature deposition of conformal copper films in supercritical CO<sub>2</sub> by catalytic hydrogen reduction of copper hexafluoroacetylacetonate,” *Chemistry of Materials*, vol. 16, no. 21, pp. 4028–4031, 2004.
- [209] OKAMOTO, T. and YAMAGUCHI, I., “Optical absorption study of the surface plasmon resonance in gold nanoparticles immobilized onto a gold substrate by self-assembly technique,” *The Journal of Physical Chemistry B*, vol. 107, no. 38, pp. 10321–10324, 2003.
- [210] OTTO, A., BRUCKBAUER, A., and CHEN, Y. X., “On the chloride activation in SERS and single molecule SERS,” *Journal of Molecular Structure*, vol. 661-662, pp. 501–514, 2003.

- [211] OUTOKESH, M., HOSSEINPOUR, M., AHMADI, S. J., MOUSAVAND, T., SADJADI, S., and SOLTANIAN, W., “Hydrothermal synthesis of CuO nanoparticles: Study on effects of operational conditions on yield, purity, and size of the nanoparticles,” *Industrial & Engineering Chemistry Research*, vol. 50, no. 6, pp. 3540–3554, 2011.
- [212] OZIN, G., ARSENAULT, A., and CADEMARTIRI, L., *Nanochemistry: A Chemical Approach to Nanomaterials*. Royal Society of Chemistry, 2008.
- [213] PACIOTTI, G., MYER, L., WEINREICH, D., GOIA, D., PAVEL, N., MCLAUGHLIN, R., and TAMARKIN, L., “Colloidal gold: a novel nanoparticle vector for tumor directed drug delivery,” *Drug Delivery*, vol. 11, no. 3, pp. 169–183, 2004.
- [214] PAN, T., LEI, T., CHAO, T., LIAW, M., KO, F., and LU, C., “One-step cleaning solution to replace the conventional RCA two-step cleaning recipe for pregate oxide cleaning,” *Journal of The Electrochemical Society*, vol. 148, no. 6, pp. 315–320, 2001.
- [215] PAPALAMBROS, P. Y. and WILDE, D. J., *Principles of Optimal Design: Modeling and Computation*. Cambridge University Press, 2000.
- [216] PARK, H., YOON, J., and KIM, K., “Novel fabrication of Ag thin film on glass for efficient surface-enhanced Raman scattering,” *Langmuir*, vol. 22, no. 4, pp. 1626–1629, 2006.
- [217] PARK, I., LI, Z., PISANO, A., and WILLIAMS, R., “Top-down fabricated silicon nanowire sensors for real-time chemical detection,” *Nanotechnology*, vol. 21, no. 1, p. 015501, 2009.

- [218] PARK, W., YI, G., KIM, M., and PENNYCOOK, S., “Quantum confinement observed in ZnO/ZnMgO nanorod heterostructures,” *Advanced Materials*, vol. 15, no. 6, pp. 526–529, 2003.
- [219] PARK, Y. K., AGHALAYAM, P., and VLACHOS, D. G., “A generalized approach for predicting coverage-dependent reaction parameters of complex surface reactions: Application to H<sub>2</sub> oxidation over platinum,” *The Journal of Physical Chemistry A*, vol. 103, no. 40, pp. 8101–8107, 1999.
- [220] PARRY, M. and WALLACH, R., “Ethylene glycol poisoning,” *The American Journal of Medicine*, vol. 57, no. 1, pp. 143–150, 1974.
- [221] PEKER, H., SRINIVASAN, M., SMITH, J., and MCCOY, B., “Caffeine extraction rates from coffee beans with supercritical carbon dioxide,” *AIChE Journal*, vol. 38, no. 5, pp. 761–770, 1992.
- [222] PEMASIRI, K., MONTAZERI, M., GASS, R., SMITH, L., JACKSON, H., YARRISON-RICE, J., PAIMAN, S., GAO, Q., TAN, H., JAGADISH, C., and OTHERS, “Carrier dynamics and quantum confinement in type II ZB-WZ InP nanowire homostructures,” *Nano Letters*, vol. 9, no. 2, pp. 648–654, 2009.
- [223] PERSSON, A., LARSSON, M., STENSTRÖM, S., OHLSSON, B., SAMUELSON, L., and WALLENBERG, L., “Solid-phase diffusion mechanism for GaAs nanowire growth,” *Nature Materials*, vol. 3, no. 10, pp. 677–681, 2004.
- [224] POORTMANS, J. and ARKHIPOV, V., *Thin Film Solar Cells: Fabrication, Characterization and Applications*. Wiley, 2006.
- [225] PRISTINSKI, D., TAN, S., EROL, M., DU, H., and SUKHISHVILI, S., “*In situ* SERS study of Rhodamine 6G adsorbed on individually immobilized Ag nanoparticles,” *Journal of Raman Spectroscopy*, vol. 37, no. 7, pp. 762–770, 2006.

- [226] PUKELSHEIM, F., *Optimal Design of Experiments*. Society for Industrial Mathematics, 2006.
- [227] RAIMONDEAU, S. and VLACHOS, D., “Recent developments on multiscale, hierarchical modeling of chemical reactors,” *Chemical Engineering Journal*, vol. 90, no. 1, pp. 3–23, 2002.
- [228] RAMANATHAN, K., CONTRERAS, M., PERKINS, C., ASHER, S., HASOON, F., KEANE, J., YOUNG, D., ROMERO, M., METZGER, W., NOUFI, R., and OTHERS, “Properties of 19.2% efficiency ZnO/CdS/CuInGaSe<sub>2</sub> thin-film solar cells,” *Progress in Photovoltaics: Research and Applications*, vol. 11, no. 4, pp. 225–230, 2003.
- [229] RAMASAMY, K., MALIK, M., and O’BRIEN, P., “The chemical vapor deposition of Cu<sub>2</sub>ZnSnS<sub>4</sub> thin films,” *Chemical Science*, vol. 2, no. 6, pp. 1170–1172, 2011.
- [230] RAMGIR, N., SUBANNAJUI, K., YANG, Y., GRIMM, R., MICHIELS, R., and ZACHARIAS, M., “Reactive VLS and the reversible switching between VS and VLS growth modes for ZnO nanowire growth,” *The Journal of Physical Chemistry C*, vol. 114, no. 23, pp. 10323–10329, 2010.
- [231] RATH, N., RASAPUTRA, K., LIYANAGE, R., HUFF, G., and HUFF, W., *Dithiocarbamate Toxicity-An Appraisal*. InTechOpen, 2011.
- [232] RATHORE, H., VARSHNEY, G., MOJUMDAR, S., and SALEH, M., “Synthesis, characterization and fungicidal activity of zinc diethyldithiocarbamate and phosphate,” *Journal of Thermal Analysis and Calorimetry*, vol. 90, no. 3, pp. 681–686, 2007.

- [233] RAVEENDRAN, P., FU, J., and WALLEN, S., “Completely green synthesis and stabilization of metal nanoparticles,” *Journal of the American Chemical Society*, vol. 125, no. 46, pp. 13940–13941, 2003.
- [234] REESE, C. S., WILSON, A. G., HAMADA, M., MARTZ, H. F., and RYAN, K. J., “Integrated analysis of computer and physical experiments,” *Technometrics*, vol. 46, no. 2, pp. 153–164, 2004.
- [235] REIFFENSTEIN, R., HULBERT, W., and ROTH, S., “Toxicology of hydrogen sulfide,” *Annual Review of Pharmacology and Toxicology*, vol. 32, no. 1, pp. 109–134, 1992.
- [236] REINHARDT, K. and KERN, W., *Handbook of Silicon Wafer Cleaning Technology*. William Andrew Inc., 2 ed., 2008.
- [237] RITALA, M. and LESKELA, M., *Atomic Layer Deposition*. Academic Press: San Diego, CA, 2001.
- [238] RIVILLON, S., CHABAL, Y. J., AMY, F., and KAHN, A., “Hydrogen passivation of germanium (100) surface using wet chemical preparation,” *Applied Physics Letters*, vol. 87, no. 25, pp. 253101–253101–3, 2005.
- [239] ROBSON, C., *Real World Research: A Resource for Users of Social Research Methods in Applied Settings*. Wiley, 2011.
- [240] ROCO, M., “The long view of nanotechnology development: The National Nanotechnology Initiative at 10 years,” *Nanotechnology Research Directions for Societal Needs in 2020*, pp. 1–28, 2011.
- [241] ROOPAN, S. and NAWAZ KHAN, F., “ZnO nanoparticles in the synthesis of AB ring core of camptothecin,” *Chemical Papers*, vol. 64, no. 6, pp. 812–817, 2010.

- [242] RYBALTOVSKII, A., ZAVOROTNYI, Y., MINAEV, N., SAMOILOVICH, M., TIMASHEV, P., TSVETKOV, M., and BAGRATASHVILI, V., “Synthesis of silver nanocomposites by SCF impregnation of matrices of synthetic opal and vycor glass by the Ag(hfac)COD precursor,” *Russian Journal of Physical Chemistry B*, vol. 3, no. 7, pp. 1106–1112, 2009.
- [243] SACKS, J., WELCH, W. J., MITCHELL, T. J., and WYNN, H. P., “Design and analysis of computer experiments,” *Statistical Science*, vol. 4, no. 4, pp. 409–423, 1989.
- [244] SAPRA, S., PRAKASH, A., GHANGREKAR, A., PERIASAMY, N., and SARMA, D., “Emission properties of manganese-doped ZnS nanocrystals,” *The Journal of Physical Chemistry B*, vol. 109, no. 5, pp. 1663–1668, 2005.
- [245] SARSWAT, P. and FREE, M., “Demonstration of a sol–gel synthesized bifacial CZTS photoelectrochemical cell,” *physica status solidi (a)*, vol. 208, no. 12, pp. 2861–2864, 2011.
- [246] SAU, T. and ROGACH, A., *Colloids, Nanocrystals, and Surface Nanostructures of Uniform Size and Shape: Modeling of Nucleation and Growth in Solution Synthesis*. Wiley Online Library, 2012.
- [247] SCHMIDT, O. and EBERL, K., “Nanotechnology: Thin solid films roll up into nanotubes,” *Nature*, vol. 410, no. 6825, pp. 168–168, 2001.
- [248] SCHUBERT, B.-A., MARSEN, B., CINQUE, S., UNOLD, T., KLENK, R., SCHORR, S., and SCHOCK, H.-W., “Cu<sub>2</sub>ZnSnS<sub>4</sub> thin film solar cells by fast coevaporation,” *Progress in Photovoltaics: Research and Applications*, vol. 19, no. 1, pp. 93–96, 2011.

- [249] SCHWAAB, M., MONTEIRO, J. L., and PINTO, J. C., “Sequential experimental design for model discrimination: Taking into account the posterior covariance matrix of differences between model predictions,” *Chemical Engineering Science*, vol. 63, no. 9, pp. 2408 – 2419, 2008.
- [250] SCRAGG, J., DALE, P., PETER, L., ZOPPI, G., and FORBES, I., “New routes to sustainable photovoltaics: Evaluation of  $\text{Cu}_2\text{ZnSnS}_4$  as an alternative absorber material,” *physica status solidi (b)*, vol. 245, no. 9, pp. 1772–1778, 2008.
- [251] SELL, S., MCCLURE, M., GARG, K., WOLFE, P., and BOWLIN, G., “Electrospinning of collagen/biopolymers for regenerative medicine and cardiovascular tissue engineering,” *Advanced Drug Delivery Reviews*, vol. 61, no. 12, pp. 1007–1019, 2009.
- [252] SEOL, J., LEE, S., LEE, J., NAM, H., and KIM, K., “Electrical and optical properties of  $\text{Cu}_2\text{ZnSnS}_4$  thin films prepared by rf magnetron sputtering process,” *Solar Energy Materials & Solar Cells*, vol. 75, no. 1, pp. 155–162, 2003.
- [253] SHAFIEI, S., NOURBAKHS, A., GANJIPOUR, B., ZAHEDIFAR, M., and VAKILI-NEZHAAD, G., “Diameter optimization of VLS-synthesized ZnO nanowires, using statistical design of experiment,” *Nanotechnology*, vol. 18, no. 35, p. 355708, 2007.
- [254] SHAH, A., TORRES, P., TSCHARNER, R., WYRSCH, N., and KEPPNER, H., “Photovoltaic technology: The case for thin-film solar cells,” *Science*, vol. 285, no. 5428, pp. 692–698, 1999.
- [255] SHAVEL, A., ARBIOL, J., and CABOT, A., “Synthesis of quaternary chalcogenide nanocrystals: Stannite  $\text{Cu}_2\text{Zn}_x\text{Sn}_y\text{Se}_{1+x+2y}$ ,” *Journal of the American Chemical Society*, vol. 132, no. 13, pp. 4514–4515, 2010.

- [256] SHELDON, R., “Green solvents for sustainable organic synthesis: state of the art,” *Green Chemistry*, vol. 7, no. 5, pp. 267–278, 2005.
- [257] SHEN, X., JIANG, Z., GAO, C., XU, Z., XIE, Z., and ZHENG, L., “One-step construction of ZnS/C and CdS/C one-dimensional core-shell nanostructures,” *Journal of Materials Chemistry*, vol. 17, no. 13, pp. 1326–1330, 2007.
- [258] SILVA, G., “Introduction to nanotechnology and its applications to medicine,” *Surgical Neurology*, vol. 61, no. 3, pp. 216–220, 2004.
- [259] SLOUFOVA, I., SISKOVA, K., VLCKOVA, B., and STEPANEK, J., “SERS-activating effect of chlorides on borate-stabilized silver nanoparticles: formation of new reduced adsorption sites and induced nanoparticle fusion,” *Physical Chemistry Chemical Physics*, vol. 10, no. 16, pp. 2233–2242, 2008.
- [260] SMART, N., CARLESON, T., ELSHANI, S., WANG, S., and WAI, C., “Extraction of toxic heavy metals using supercritical fluid carbon dioxide containing organophosphorus reagents,” *Industrial & Engineering Chemistry Research*, vol. 36, no. 5, pp. 1819–1826, 1997.
- [261] SMITH, J., VAN NESS, H., and ABBOTT, M., *Chemical Engineering Thermodynamics*. McGraw Hill, 2001.
- [262] SOTELO-GONZALEZ, E., FERNANDEZ-ARGÜELLES, M., COSTA-FERNANDEZ, J., and SANZ-MEDEL, A., “Mn-doped ZnS quantum dots for the determination of acetone by phosphorescence attenuation,” *Analytica Chimica Acta*, 2011.
- [263] SRINIVASAN, R., “Kinetics of the ablative photodecomposition of organic polymers in the far ultraviolet (193 nm),” *Journal of Vacuum Science & Technology B: Microelectronics and Nanometer Structures*, vol. 1, no. 4, pp. 923–926, 1983.

- [264] STAMPLECOSKIE, K., SCAIANO, J., TIWARI, V., and ANIS, H., “Optimal size of silver nanoparticles for surface-enhanced Raman spectroscopy,” *The Journal of Physical Chemistry C*, vol. 115, no. 5, pp. 1403–1409, 2011.
- [265] STEIN, M., “Large sample properties of simulations using Latin hypercube sampling,” *Technometrics*, vol. 29, no. 2, pp. 143–151, 1987.
- [266] STEWART, W. E., SHON, Y., and BOX, G. E. P., “Discrimination and goodness of fit of multiresponse mechanistic models,” *AIChE Journal*, vol. 44, no. 6, pp. 1404–1412, 1998.
- [267] STEWART, W. E., HENSON, T. L., and BOX, G. E. P., “Model discrimination and criticism with single-response data,” *AIChE Journal*, vol. 42, no. 11, pp. 3055–3062, 1996.
- [268] STIGER, R. M., GORER, S., CRAFT, B., and PENNER, R. M., “Investigations of electrochemical silver nanocrystal growth on hydrogen-terminated silicon(100),” *Langmuir*, vol. 15, no. 3, pp. 790–798, 1998.
- [269] SUBRAMANIAM, B., RAJEWSKI, R., and SNAVELY, K., “Pharmaceutical processing with supercritical carbon dioxide,” *Journal of Pharmaceutical Sciences*, vol. 86, no. 8, pp. 885–890, 1997.
- [270] SUN, Y. and XIA, Y., “Shape-controlled synthesis of gold and silver nanoparticles,” *Science*, vol. 298, no. 5601, pp. 2176–2179, 2002.
- [271] SUTCLIFFE, E. and SRINIVASAN, R., “Dynamics of UV laser ablation of organic polymer surfaces,” *Journal of Applied Physics*, vol. 60, no. 9, pp. 3315–3322, 1986.
- [272] TAGUCHI, G., *Introduction to Quality Engineering: Designing Quality into Products and Processes*. Quality Resources, 1986.

- [273] TAGUCHI, G., “Quality engineering (Taguchi methods) for the development of electronic circuit technology,” *IEEE Transactions on Reliability*, vol. 44, no. 2, pp. 225–229, 1995.
- [274] TAGUCHI, G. and CARIAPA, V., “Taguchi on robust technology development,” *Journal of Pressure Vessel Technology*, vol. 115, p. 336, 1993.
- [275] TAGUCHI, G. and CLAUSING, D., “Robust quality,” *Harvard Business Review*, vol. 68, no. 1, pp. 65–75, 1990.
- [276] TAGUCHI, G., TUNG, L., and CLAUSING, D., *System of Experimental Design: Engineering Methods to Optimize Quality and Minimize Costs*. UNIPUB/Kraus International Publications, 1987.
- [277] TAGUCHI, G. and YOKOYAMA, Y., *Taguchi Methods*, vol. 1. ASI Press, 1994.
- [278] TAN, R., AGARWAL, A., BALASUBRAMANIAN, N., KWONG, D., JIANG, Y., WIDJAJA, E., and GARLAND, M., “3D arrays of SERS substrate for ultrasensitive molecular detection,” *Sensors and Actuators A: Physical*, vol. 139, no. 1, pp. 36–41, 2007.
- [279] TANAKA, T., NAGATOMO, T., KAWASAKI, D., NISHIO, M., GUO, Q., WAKAHARA, A., YOSHIDA, A., and OGAWA, H., “Preparation of  $\text{Cu}_2\text{ZnSnS}_4$  thin films by hybrid sputtering,” *Journal of Physics and Chemistry of Solids*, vol. 66, no. 11, pp. 1978–1981, 2005.
- [280] TANIGUCHI, N. and OTHERS, “On the basic concept of nanotechnology,” in *Proc. Intl. Conf. Prod. Eng. Tokyo, Part II, Japan Society of Precision Engineering*, pp. 18–23, 1974.
- [281] TAO, A. R., HABAS, S., and YANG, P., “Shape control of colloidal metal nanocrystals,” *Small*, vol. 4, no. 3, pp. 310–325, 2008.

- [282] TEMPLE, P. A. and HATHAWAY, C. E., “Multiphonon Raman spectrum of silicon,” *Physical Review B*, vol. 7, no. 8, p. 3685, 1973.
- [283] TERANISHI, T., KURITA, R., and MIYAKE, M., “Shape control of Pt nanoparticles,” *Journal of Inorganic and Organometallic Polymers*, vol. 10, no. 3, pp. 145–156, 2000.
- [284] TERSOFF, J. and HAMANN, D., “Theory and application for the scanning tunneling microscope,” *Physical Review Letters*, vol. 50, no. 25, pp. 1998–2001, 1983.
- [285] TERSOFF, J. and HAMANN, D., “Theory of the scanning tunneling microscope,” *Physical Review B*, vol. 31, no. 2, p. 805, 1985.
- [286] TOMICK, J. J., ARNOLD, S. F., and BARTON, R. R., “Sample size selection for improved Nelder-Mead performance,” in *Simulation Conference Proceedings*, pp. 341–345, IEEE, 1995.
- [287] TSAKALAKOS, L., BALCH, J., FRONHEISER, J., KOREVAAR, B., SULIMA, O., and RAND, J., “Silicon nanowire solar cells,” *Applied Physics Letters*, vol. 91, no. 23, pp. 233117–233120, 2007.
- [288] TSU, D., LUCOVSKY, G., and MANTINI, M., “Local atomic structure in thin films of silicon nitride and silicon diimide produced by remote plasma-enhanced chemical vapor deposition,” *Physical Review B*, vol. 33, no. 10, p. 7069, 1986.
- [289] TSUNG, C.-K., KUHN, J. N., HUANG, W., ALIAGA, C., HUNG, L.-I., SOMORJAI, G. A., and YANG, P., “Sub-10 nm platinum nanocrystals with size and shape control: catalytic study for ethylene and pyrrole hydrogenation,” *Journal of the American Chemical Society*, vol. 131, no. 16, pp. 5816–5822, 2009.

- [290] TSYGANENKO, A. and FILIMONOV, V., “Infrared spectra of surface hydroxyl groups and crystalline structure of oxides,” *Journal of Molecular Structure*, vol. 19, pp. 579–589, 1973.
- [291] VASTOLA, J. T., *Sequential Experimental Design Under Competing Prior Knowledge*. PhD thesis, H. Milton Stewart School of Industrial & Systems Engineering, Georgia Institute of Technology, 2012.
- [292] VAZQUEZ, A., LOPEZ, I., and GOMEZ, I., “Growth of one-dimensional zinc sulfide nanostructures through electrophoretic deposition,” *Materials Letters*, vol. 65, no. 15, pp. 2422–2425, 2011.
- [293] VOROB’EV, A., KARPOV, S. Y., BOGDANOV, M., KOMISSAROV, A., BORD, O., ZHMAKIN, A., and MAKAROV, Y. N., “Numerical study of SiC CVD in a vertical cold-wall reactor,” *Computational Materials Science*, vol. 24, no. 4, pp. 520–534, 2002.
- [294] WAI, C., WANG, S., and YU, J., “Solubility parameters and solubilities of metal dithiocarbamates in supercritical carbon dioxide,” *Analytical Chemistry*, vol. 68, no. 19, pp. 3516–3519, 1996.
- [295] WALPOLE, R., MYERS, R., MYERS, S., and YE, K., *Probability and Statistics for Engineers and Scientists*, vol. 5. Macmillan New York, 1972.
- [296] WANG, J. and MARSHALL, W., “Recovery of metals from aqueous media by extraction with supercritical carbon dioxide,” *Analytical Chemistry*, vol. 66, no. 10, pp. 1658–1663, 1994.
- [297] WANG, K., GUNAWAN, O., TODOROV, T., SHIN, B., CHEY, S., BOJARCZUK, N., MITZI, D., and GUHA, S., “Thermally evaporated  $\text{Cu}_2\text{ZnSnS}_4$  solar cells,” *Applied Physics Letters*, vol. 97, no. 14, pp. 143508–143508, 2010.

- [298] WANG, K., WEI, M., MORRIS, M., ZHOU, H., and HOLMES, J., “Mesoporous titania nanotubes: their preparation and application as electrode materials for rechargeable lithium batteries,” *Advanced Materials*, vol. 19, no. 19, pp. 3016–3020, 2007.
- [299] WANG, M., RAGHUNATHAN, N., and ZIAIE, B., “A nonlithographic top-down electrochemical approach for creating hierarchical (micro-nano) superhydrophobic silicon surfaces,” *Langmuir*, vol. 23, no. 5, pp. 2300–2303, 2007.
- [300] WANG, X., YANG, L., CHEN, Z., and SHIN, D., “Application of nanotechnology in cancer therapy and imaging,” *CA: A Cancer Journal for Clinicians*, vol. 58, no. 2, pp. 97–110, 2008.
- [301] WANG, Y., SCHMIDT, V., SENZ, S., and GÖSELE, U., “Epitaxial growth of silicon nanowires using an aluminium catalyst,” *Nature Nanotechnology*, vol. 1, no. 3, pp. 186–189, 2006.
- [302] WASZCZUK, P., LU, G.-Q., WIECKOWSKI, A., LU, C., RICE, C., and MASEL, R., “UHV and electrochemical studies of CO and methanol adsorbed at platinum/ruthenium surfaces, and reference to fuel cell catalysis,” *Electrochimica Acta*, vol. 47, no. 22-23, pp. 3637 – 3652, 2002.
- [303] WATKINS, J., BLACKBURN, J., and MCCARTHY, T., “Chemical fluid deposition: reactive deposition of platinum metal from carbon dioxide solution,” *Chemistry of Materials*, vol. 11, no. 2, pp. 213–215, 1999.
- [304] WEI, D., LIU, Y., CAO, L., ZHANG, H., HUANG, L., and YU, G., “Synthesis and photoelectric properties of coaxial Schottky junctions of ZnS and carbon nanotubes,” *Chemistry of Materials*, vol. 22, no. 2, pp. 288–293, 2009.

- [305] WENDLER, F., MENNERICH, C., and NESTLER, B., “A phase-field model for polycrystalline thin film growth,” *Journal of Crystal Growth*, vol. 327, no. 1, pp. 189 – 201, 2011.
- [306] WENZEL, T., BOSBACH, J., STIETZ, F., and TRÄGER, F., “*In situ* determination of the shape of supported silver clusters during growth,” *Surface Science*, vol. 432, no. 3, pp. 257–264, 1999.
- [307] WHITESIDES, G., “Nanoscience, nanotechnology, and chemistry,” *Small*, vol. 1, no. 2, pp. 172–179, 2004.
- [308] WILLETS, K. and VAN DUYN, R., “Localized surface plasmon resonance spectroscopy and sensing,” *Annual Review of Physical Chemistry*, vol. 58, pp. 267–297, 2007.
- [309] WILSON, R., “The use of gold nanoparticles in diagnostics and detection,” *Chemical Society Reviews*, vol. 37, no. 9, pp. 2028–2045, 2008.
- [310] WISSMANN, P. J. and GROVER, M. A., “A new approach to batch process optimization using experimental design,” *AIChE Journal*, vol. 55, no. 2, pp. 342–353, 2009.
- [311] WISSMANN, P. J. and GROVER, M. A., “Optimization of a chemical vapor deposition process using sequential experimental design,” *Industrial & Engineering Chemistry Research*, vol. 49, no. 12, pp. 5694–5701, 2010.
- [312] WOEHLE, T., EVANS, J., ARSLAN, I., RISTENPART, W., and BROWNING, N., “Direct *in situ* determination of the mechanisms controlling nanoparticle nucleation and growth,” *ACS Nano*, vol. 6, no. 10, pp. 8599–8610, 2012.
- [313] WU, C. J. and HAMADA, M. S., *Experiments: Planning, Analysis, and Optimization*. Wiley, 2011.

- [314] WU, F., LEVITIN, G., and HESS, D., “Mechanistic considerations of low temperature hydrogen-based plasma etching of Cu,” *Journal of Vacuum Science & Technology B: Microelectronics and Nanometer Structures*, vol. 29, no. 1, pp. 011013–011013–7, 2011.
- [315] XIE, Y., ZHANG, C., MIAO, S., LIU, Z., DING, K., MIAO, Z., AN, G., and YANG, Z., “One-pot synthesis of ZnS/polymer composites in supercritical CO<sub>2</sub>-ethanol solution and their applications in degradation of dyes,” *Journal of Colloid and Interface Science*, vol. 318, no. 1, pp. 110–115, 2008.
- [316] XU, C., BAUM, T. H., and RHEINGOLD, A. L., “New precursors for chemical vapor deposition of iridium,” *Chemistry of Materials*, vol. 10, no. 9, pp. 2329–2331, 1998.
- [317] XU, C., DIMEO, F., BAUM, T. H., and RUSSELL, M., “Chemical vapor deposition (CVD) of iridium and platinum films and gas-phase chemical etching of iridium thin films,” in *Materials Research Society Symposium Proceedings*, vol. 541, pp. 129–140, Cambridge Univ Press, 1999.
- [318] XU, H., JIA, H., YAO, Z., and LI, X., “Photoluminescence and IV characteristics of ZnS grown on silicon nanoporous pillar array,” *Journal of Materials Research*, vol. 23, no. 1, pp. 121–126, 2008.
- [319] XU, S., ADIGA, N., BA, S., DASGUPTA, T., WU, C. F. J., and WANG, Z. L., “Optimizing and improving the growth quality of ZnO nanowire arrays guided by statistical design of experiments,” *ACS Nano*, vol. 3, no. 7, pp. 1803–1812, 2009.
- [320] YANG, C. and LI, S., “Size, dimensionality, and constituent stoichiometry dependence of bandgap energies in semiconductor quantum dots and wires,” *The Journal of Physical Chemistry C*, vol. 112, no. 8, pp. 2851–2856, 2008.

- [321] YANG, J., HYDE, J., WILSON, J., MALLIK, K., SAZIO, P., O'BRIEN, P., MALIK, M., AFZAAL, M., NGUYEN, C., GEORGE, M., and OTHERS, "Continuous flow supercritical chemical fluid deposition of optoelectronic quality CdS," *Advanced Materials*, vol. 21, no. 41, pp. 4115–4119, 2009.
- [322] YE, X. R., WAI, C. M., ZHANG, D., KRANOV, Y., MCILROY, D. N., LIN, Y., and ENGELHARD, M., "Immersion deposition of metal films on silicon and germanium substrates in supercritical carbon dioxide," *Chemistry of Materials*, vol. 15, no. 1, pp. 83–91, 2002.
- [323] YE, X., LIN, Y., WANG, C., ENGELHARD, M., WANG, Y., and WAI, C., "Supercritical fluid synthesis and characterization of catalytic metal nanoparticles on carbon nanotubes," *Journal of Materials Chemistry*, vol. 14, no. 5, pp. 908–913, 2004.
- [324] YE, X., LIN, Y., WANG, C., and WAI, C., "Supercritical fluid fabrication of metal nanowires and nanorods templated by multiwalled carbon nanotubes," *Advanced Materials*, vol. 15, no. 4, pp. 316–319, 2003.
- [325] YEH, C., MAITRA, A., LEE, K., JAN, Y., and CHEN, M., "Thioacetamide-induced intestinal-type cholangiocarcinoma in rat: an animal model recapitulating the multi-stage progression of human cholangiocarcinoma," *Carcinogenesis*, vol. 25, no. 4, pp. 631–636, 2004.
- [326] YOU, T., NIWA, O., KURITA, R., IWASAKI, Y., HAYASHI, K., SUZUKI, K., and HIRONO, S., "Reductive H<sub>2</sub>O<sub>2</sub> detection at nanoparticle iridium/carbon film electrode and its application as L-glutamate enzyme sensor," *Electroanalysis*, vol. 16, no. 1-2, pp. 54–59, 2004.

- [327] YU, Q. and GOLDEN, G., “Probing the protein orientation on charged self-assembled monolayers on gold nanohole arrays by SERS,” *Langmuir*, vol. 23, no. 17, pp. 8659–8662, 2007.
- [328] ZHANG, Y., KANG, D., SAQUING, C., AINDOW, M., and ERKEY, C., “Supported platinum nanoparticles by supercritical deposition,” *Industrial & Engineering Chemistry Research*, vol. 44, no. 11, pp. 4161–4164, 2005.
- [329] ZHAO, L. and GAO, L., “Coating multi-walled carbon nanotubes with zinc sulfide,” *Journal of Materials Chemistry*, vol. 14, no. 6, pp. 1001–1004, 2004.
- [330] ZHAO, Q., XIE, Y., ZHANG, Z., and BAI, X., “Size-selective synthesis of zinc sulfide hierarchical structures and their photocatalytic activity,” *Crystal Growth & Design*, vol. 7, no. 1, pp. 153–158, 2007.
- [331] ZHAO, Y., ZHANG, Y., ZHU, H., HADJIPANAYIS, G., and XIAO, J., “Low-temperature synthesis of hexagonal (wurtzite) ZnS nanocrystals,” *Journal of the American Chemical Society*, vol. 126, no. 22, pp. 6874–6875, 2004.
- [332] ZHOU, Q., LI, Z., YANG, Y., and ZHANG, Z., “Arrays of aligned, single crystalline silver nanorods for trace amount detection,” *Journal of Physics D: Applied Physics*, vol. 41, no. 15, p. 152007, 2008.
- [333] ZHU, J., ZHOU, M., XU, J., and LIAO, X., “Preparation of CdS and ZnS nanoparticles using microwave irradiation,” *Materials Letters*, vol. 47, no. 1, pp. 25–29, 2001.
- [334] ZHU, Y., BANDO, Y., and XUE, D., “Spontaneous growth and luminescence of zinc sulfide nanobelts,” *Applied Physics Letters*, vol. 82, no. 11, pp. 1769–1771, 2003.

- [335] ZONG, Y. and WATKINS, J., “Deposition of copper by the H<sub>2</sub>-assisted reduction of Cu(tm<sub>2</sub>d)<sub>2</sub> in supercritical carbon dioxide: Kinetics and reaction mechanism,” *Chemistry of Materials*, vol. 17, no. 3, pp. 560–565, 2005.

## VITA

Michael was born in 1986 in Fort Lauderdale, Florida. He attended Cardinal Gibbons High School where he earned the distinction of Valedictorian. He then attended the University of Miami in Coral Gables, Florida, graduating *summa cum laude* with a Bachelor of Science degree in Neuroscience and minors in Mathematics, Chemistry, and Physics. He was admitted to Phi Beta Kappa in the spring of 2007. At the Georgia Institute of Technology, he earned several fellowships, including a National Science Foundation Graduate Research Fellowship in 2010.

When not in the lab, Michael enjoys cheering for the Miami Hurricanes in football and baseball, teaching and dancing *salsa*, and playing softball.